X-RAY SCATTERING STUDIES OF CHARGE DENSITY WAVES IN CUPRATE AND PNICTIDE SUPERCONDUCTORS

BY

SANGJUN LEE

DISSERTATION

Submitted in partial fulfillment of the requirements
for the degree of Doctor of Philosophy in Physics
in the Graduate College of the
University of Illinois at Urbana-Champaign, 2021

Urbana, Illinois

Doctoral Committee:

Professor Vidya Madhavan, Chair
Professor Peter Abbamonte, Director of Research
Professor Eduardo Fradkin
Assistant Professor Jeffrey Filippini

Abstract

The phase diagrams of unconventional superconductors exhibit many different broken-symmetry phases near superconductivity, such as antiferromagnetism, charge density wave, spin density wave, and nematic order. The proximity and similar temperature scales of these orders suggest superconductivity and other order parameters are intertwined, and how they intertwine is a longstanding problem in condensed matter physics. Among the phases found in the vicinity of superconductivity, charge density wave (CDW) has been found in nearly all cuprate superconductors and observed to have an intimate relationship with superconductivity. Thus, characterizing the nature of CDWs is crucial for understanding the mechanism of unconventional superconductivity. Here, we studied CDWs in cuprate and pnictide superconductors using various x-ray scattering techniques. We discovered new CDW phases in $\mathrm{BaNi_2As_2}$ and Co-, Sr-doped systems, confirming a generic presence of CDW in the phase diagram of unconventional superconductors, and the nature of the superconductivity in these systems are closely related to the presence of CDW. We also precisely measured the temperature and doping evolution of the CDW wave vector in $\mathrm{La_{1.8-\mathit{x}}Eu_{0.2}Sr_{\mathit{x}}CuO_4}$, revealing the effect of the finite charge compressibility and the coupling of charge and spin order on the wave vector change. Furthermore, energy- and time-resolved resonant soft x-ray scattering experiments on the CDW in $\mathrm{La_{2-\mathit{x}}Ba_{\mathit{x}}CuO_4}$ were performed to reveal a previously unidentified fluctuating nature of the CDW.

It is the glory of God to conceal a matter;
to search out a matter is the glory of kings.
- Proverbs 25:2

Acknowledgments

First and foremost, I would like to thank my advisor Professor Peter Abbamonte for his support, guidance, patience, wisdom, and humor. I'm particularly grateful to Peter for showing trust in my abilities, which has been a great motivation for me. During my days in Urbana, Peter was always a good teacher for me, not only just in physics but also in life. I have grown a lot in many ways in my life through the lessons that I have learned from Peter.

I would also like to thank Professor Eduardo Fradkin for providing insightful theoretical explanations of my data and, also to Professor Vidya Madhavan and Professor Jeffrey Filippini, for being on my thesis committee and evaluating my thesis.

I would also like to thank my lab-mates: Gilberto de la Peña, I learned how to do an x-ray experiment from you. Thank you for teaching me how to use all the instruments in the x-ray lab. I won't be able to forget the times we spent at the beamlines. Matteo Mitrano, thank you for being a great senior, and also a great friend. Your passion in research has always inspired me. Thank you for giving me a lot of valuable advice on my papers, and also making great espresso and ragù for me. Ali Husain, thank you for being a great friend and also for the many good laughs we had, especially during the LCLS beamtimes. Also thanks for the MPMS measurements. Stella Sun, thank you for helping me with numerous experiments and always keeping the x-ray lab in good shape. Anshul Kogar, I learned how to approach and develop experiments from you in my early days of graduate school. Thank you for being an example of a good experimentalist. Yizhi Fang, Xuefei Guo, Yingying Peng, thank you for helping me with experiments at the lab and the beamlines. Mindy Rak, Sam Rubeck, Jin Chen, Cat Kengle, thank you for your help, chats, and fun memories in and out of the office.

I would also like to thank Young Il Joe, Randy Doriese, and Dan Swetz at NIST for their assists during the TES experiments and for warmly treating me during my visit at NIST for two months. Thank you to Jun-Sik Lee, Sang-Jun Lee, Hai Huang, and Hoyoung Jang (now at PAL) at SSRL for their help during the experiments at 13-3. I gained a lot of experimental skills during my visit at SSRL for nine months. Thank you to Fanny Rodolakis and Jessica McChesney at APS for their help during the experiments at sector 29.

I would also like to thank Edwin Huang for his help on the LESCO project with theoretical analyses and pointing out interesting aspects in my data. Thank you to Thomas Johnson, Alex Zakrzewski, and Chris Eckberg for providing crystals with an incredible quality.

I would also like to thank Hyuneil Kim, Gil Young Cho, and Moon Jip Park for their friendship and so many fun memories we had together. They were always warming and comforting, and they always encouraged me. Without them, I would not have endured the murkiness in my early years in Urbana.

I thank my father Siyoung Lee, my mother Soonok Kim and my brother Sanghoon Lee for their relentless support and prayers for me. I have been away from home for more than ten years, but thank you for always being there whenever I needed them.

Mi Young Jang, my wonderful wife, I can't thank you enough for your love and mental support, especially during my tough times. This thesis would not have been possible without you. I'm excited for the journey that is ahead of us.

Lastly, I thank God for everything that He planned for me and for guiding me. All honor and glory to God.

This work was supported by U.S. Department of Energy, Office of Basic Energy Sciences Grant No. DE-FG02-06ER46285. This research used resources of the Advanced Photon Source, a U.S. Department of Energy (DOE) Office of Science User Facility operated for the DOE Office of Science by Argonne National Laboratory under Contract No. DE-AC02-06CH11357. Use of the Stanford Synchrotron Radiation Lightsource, SLAC National Accelerator Laboratory, is supported by the U.S. Department of Energy, Office of Science, Office of Basic Energy Sciences under Contract No. DE-AC02-76SF00515. Use of the Linac Coherent Light Source (LCLS), SLAC National Accelerator Laboratory, is supported by the U.S. Department of Energy, Office of Science, Office of Basic Energy Sciences under Contract No. DE-AC02-76SF00515.

Table of Contents

Chapter 1

Introduction

1.1 Unconventional superconductivity

In the last few decades, several new classes of superconductors have been discovered that do not conform the conventional Bardeen–Cooper–Schrieffer (BCS) theory. The mechanism of the superconductivity of these materials is likely different from the phonon-mediated formation of Cooper pairs [1], and the pairing state was found to have a *d*-wave symmetry [2] rather than an *s*-wave symmetry as the BCS theory described. These 'non-BCS' materials are commonly referred to as unconventional superconductors, and the examples include copper oxides (cuprates) [3–5], iron pnictides and chalcogenides [6, 7], heavy fermion materials such as $CeCu_2Si_2$ [8], UBe_{13}, and UPt3 [9], and organic materials such as the quasi-1D TMTSF salts [10] and the quasi-2D BEDT-TTF salts [11]. There has been no consensus made on theoretical description of unconventional superconductivity, and its mechanism is one of the biggest unsolved problems in condensed matter physics.

Despite the diversity in their composition, crystal structure, and T_c, unconventional superconductors exhibit an important similarity in their phase diagrams, that superconductivity is always found near the boundary of some other ordered phases. Many different broken-symmetry phases appear with similar temperature and energy scales as those of superconductivity. For example, Fig. 1.1 shows typical phase diagrams of cuprate and iron-pnictide superconductors, which are some of the most studied examples, showing the proximity of the antiferromagnetic (AFM) phase to the superconductivity in both systems [5, 7]. Various other orders are also commonly found in unconventional superconductors, such as charge density wave (CDW), spin density wave (SDW), and nematic orders, near superconductivity with comparable onset temperatures. This complexity in their phase diagrams indicates that the relation between these phases are intimate and intertwined [12]. Moreover, the interaction of such orders can lead to interesting phenomena, such as the enhancement of superconductivity driven by the presence of nematic fluctuations [13], and the putative pair density wave (PDW), in which the Cooper pair density is spatially modulated, that results from the intertwining of CDW, SDW, and superconductivity orders [12].

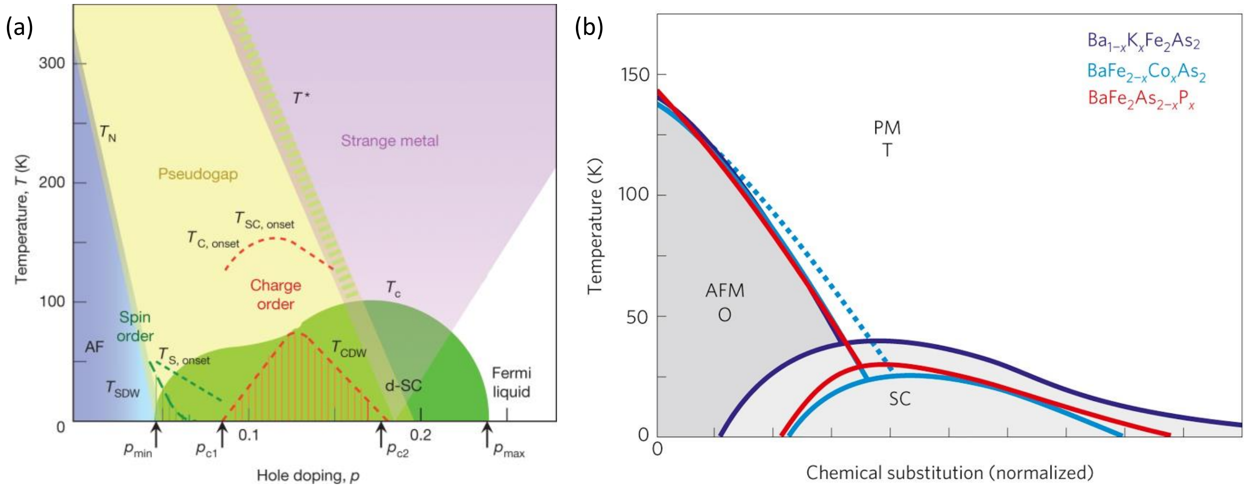

Figure 1.1: Phase diagram of (a) cuprates [5], and (b) iron-based superconductor $BaFe_2As_2$ systems [7].

Among the phases found in the vicinity of superconductivity, the phase of charge density wave (CDW) order is the main focus of this thesis. CDW is a broken-symmetry state through a self-organization of valence electrons into a periodic structure. This electronic state is ubiquitously found in the phase diagrams of cuprate superconductors, suggesting its intimate relationship to the formation of superconductivity. However, the nature of the relationship is still unclear. Some experimental observations suggest competition between CDW and superconductivity; T_c gets suppressed when a long-ranged strong CDW order develops [14], and the CDW order weakens when a system transitions into the superconducting state [15,16]. On the other hand, there are theoretical works that describe the relationship being more complex than a simple competition, and CDW may be an important ingredient in the formation of superconductivity [12]. Thus, it is crucial to experimentally determine the properties of CDW in the vicinity of superconductivity and characterize how it intertwines with other orders.

In this thesis, I present x-ray scattering results on the properties of CDWs in pnictide superconductors $Ba(Ni_{1-x}Co_x)_2As_2$ and $Ba_{1-x}Sr_xNi_2As_2$, and cuprate superconductors $La_{1.8-x}Eu_{0.2}Sr_xCuO_4$ and $La_{2-x}Ba_xCuO_4$. Evolutions of the lineshape and the ordering wave vector of CDW upon temperature and doping are measured, and their implications on the superconductivity are discussed. In the next sections, brief overviews of the materials and summaries of the main results are provided.

1.2 Nickel pnictides

$BaNi_2As_2$ is a structural homologue of the prototypical iron-based superconductor $BaFe_2As_2$. Structurally, the two compounds show some similarities; both materials have the tetragonal structure at room temperature

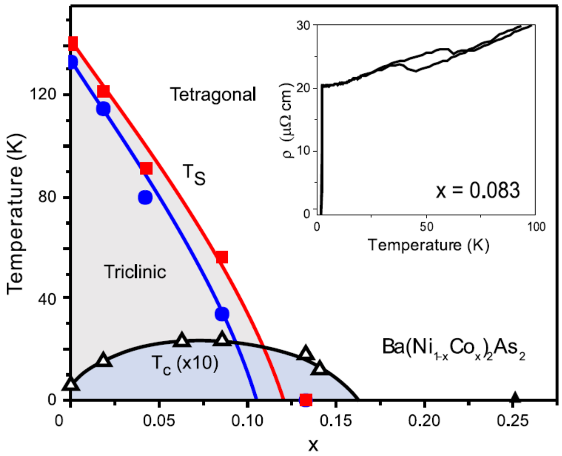

Figure 1.2: Phase diagram of Ba(Ni$_{1-x}$Co$_x$)$_2$As$_2$ showing the doping evolution of the tetragonal-to-triclinic structural phase transition temperatures and T_c [17].

and exhibit a structural phase transition at $T \sim 130$ K, to orthorhombic structure for BaFe$_2$As$_2$ [7] and to triclinic structure for BaNi$_2$As$_2$ [18]. However, in terms of electronic and magnetic properties, the two materials are quite different. For example, upon doping with Co, Ba(Fe$_{1-x}$Co$_x$)$_2$As$_2$ exhibits a maximum T_c of 24 K [19], while T_c of Ba(Ni$_{1-x}$Co$_x$)$_2$As$_2$ only reaches 2.3 K (Fig. 1.2) [17]. Moreover, BaFe$_2$As$_2$ exhibits AFM order in the orthorhombic structure [7], while neutron scattering measurements have not detected such magnetic order in BaNi$_2$As$_2$ [20]. In light of the universal phase diagram of unconventional superconductors, it is important to verify the existence of a symmetry-breaking phase in BaNi$_2$As$_2$ that parallels the role of AFM order in BaFe$_2$As$_2$, and its possible connection to the suppression of T_c in BaNi$_2$As$_2$.

In Chapter 3, we present the discovery of CDW order in BaNi$_2$As$_2$ as well as Co- and Sr-doped compounds, using hard x-ray scattering. We found that the compounds exhibit multiple CDW transitions. Especially, Ba$_{1-x}$Sr$_x$Ni$_2$As$_2$ with $x \sim 0.4$ exhibits three different CDW orders sequentially upon cooling. We also found that the doping evolution of CDW shows the same trend as that of AFM order in iron-based compounds, indicating they play similar role in each system. Moreover, recent transport and elastoresistivity measurements showed that Ba$_{1-x}$Sr$_x$Ni$_2$As$_2$ exhibit strong nematic fluctuations [Fig. 1.3(a)], and filamentary superconductivity that is characterized by broad transitions in magnetic [Fig. 1.3(c)] and transport measurements [Fig. 1.3(d)], but without a bulk signature in heat capacity measurements [Fig. 1.3(e)]. We show that the newly discovered incommensurate CDW is closely related with the nematic fluctuation, and the heterogeneous structure induced by the period-2 commensurate CDW may be the origin of the observed filamentary superconductivity.

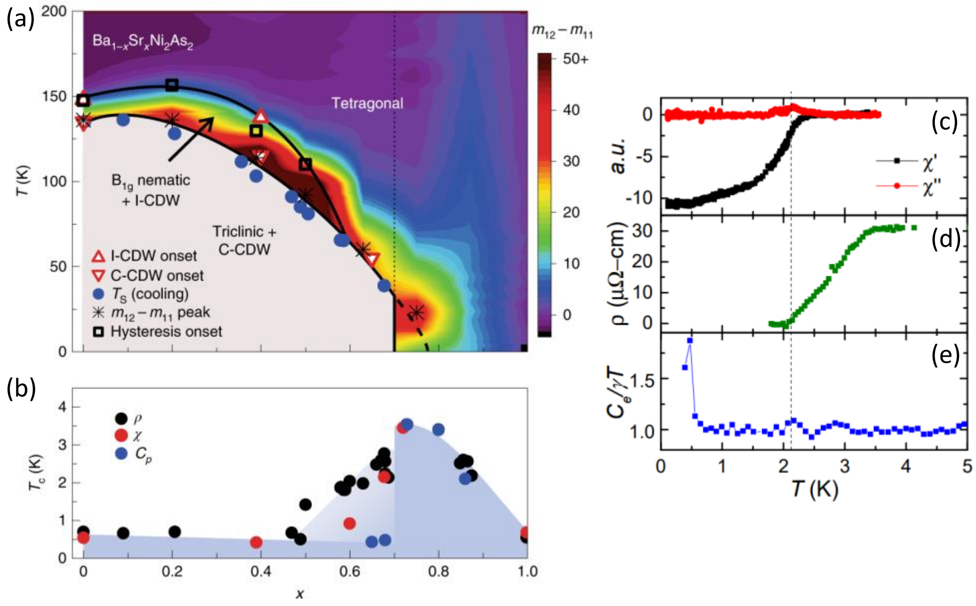

Figure 1.3: (a) Phase diagram of $Ba_{1-x}Sr_xNi_2As_2$. The overlaid color scale represents the nematic susceptibility. (b) Superconducting transition temperatures T_c determined by transport (black circles), magnetization (red circles) and heat capacity (blue circles) measurements. (c-e) Magnetization (c), transport (d), and heat capacity (e) measurements showing filamentary superconductivity in $Ba_{1-x}Sr_xNi_2As_2$ $x = 0.068$. All panels are from Ref. [13].

1.3 La-based cuprates

All cuprate superconductors share the same basic building block of CuO_2 layers [Fig. 1.4(b)] separated by spacer (or, charge reservoir) layers. Superconducting charge carriers reside in CuO_2 plane, whose electronic states near the Fermi energy are formed by the hybridization of Cu $3d$ and O $2p$ orbitals. The parent compound of La-based cuprates is La_2CuO_4 [Fig. 1.4(a)], and the CuO_2 plane can be hole-doped by substituting La with Sr or Ba and optionally co-doped with Nd or Eu.

CDW in cuprates was first discovered in the form of stripe order, as depicted in Fig. 1.4(d). In this representation, the doped holes with the doping level of 1/8 act as boundaries separating undoped domains characterized by AFM order. This geometrical configuration leads to spin density wave (SDW) with a period of 8 unit cells and CDW with a period of 4 unit cells, as first observed in $La_{1.6-x}Nd_{0.4}Sr_xCuO_4$ with $x = 0.12$ using neutron scattering in 1995 [23]. Soon after the discovery, CDW was found in nearly all cuprates using (mostly) x-ray scattering [14, 16, 24–28], neutron scattering [23, 29], and scanning tunneling microscopy (STM) [28,30], and this phase has been recognized as a generic part of the cuprate phase diagram.

Although it is a general phenomenon found in cuprates, CDW in La-based cuprates shows a distinct property compared to CDW in other families, such as $YBa_2Cu_3O_{6+\delta}$, $Bi_2Sr_{2-x}La_xCuO_{6+\delta}$, and $Bi_2Sr_2CaCu_2O_{8+\delta}$. As shown in Fig. 1.5, the doping evolution of CDW wave vector exhibits the oppo-

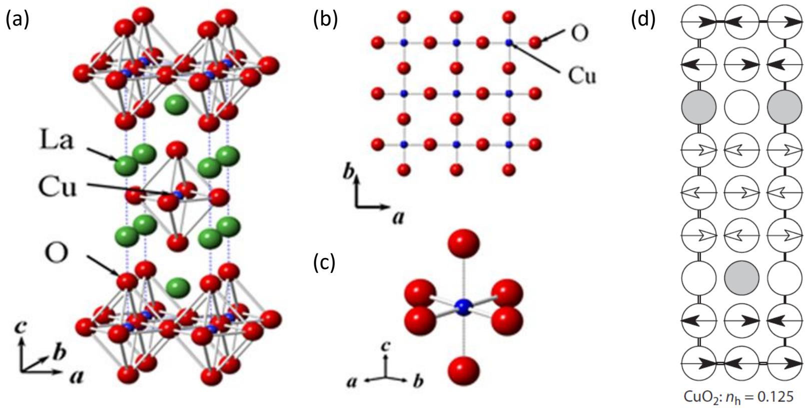

Figure 1.4: (a) Crystal structure of La_2CuO_4. La can be substituted with Sr or Ba and optionally co-doped with Nd or Eu. (b) CuO_2 layer, the common structural unit of cuprate superconductors. (c) CuO_6 octahedron. (d) Schematic drawing of the stripe pattern in cuprates: Circles represent the Cu sites in the CuO2 plane, with arrows denoting the Cu spins and gray circles indicating the location of the doped holes. (a), (b), (c) are from Ref. [21] and (d) is from Ref. [22].

site sign for La-based cuprates with respect to other families. The reason for this apparent difference is not known, and it has prevented finding a unified mechanism of CDW in cuprates. In chapter 4, we present resonant soft x-ray scattering measurements on CDW in $La_{1.8-x}Eu_{0.2}Sr_xCuO_4$. The CDW wave vector exhibit a temperature dependence due to a competition of microscopic effects, and the doping evolution of the wave vector at a high temperature follows the same trend of non-La-based cuprates. This result indicates that La-cuprates and other families may share the same origin of CDW formation.

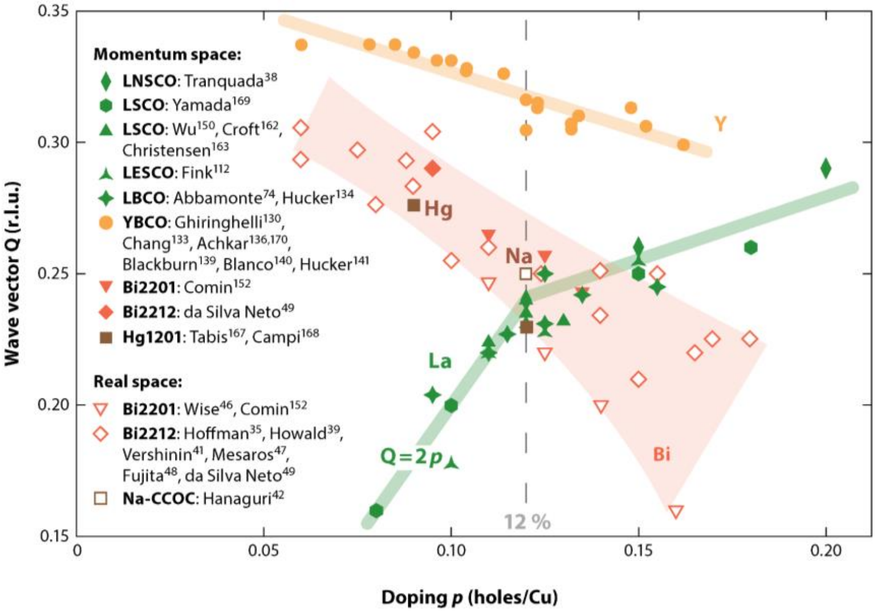

Figure 1.5: Doping dependence of the CDW wave vector of various cuprates [22].

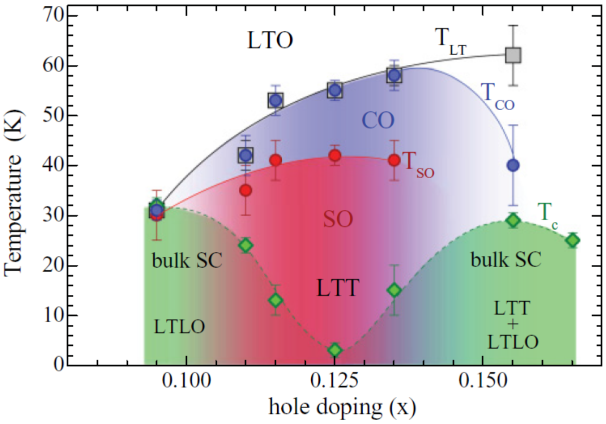

Figure 1.6: Phase diagram of $La_{2-x}Ba_xCuO_4$ showing onset temperatures of superconductivity (SC), charge stripe order (CO), spin stripe order (SO), and the low-temperature tetragonal structural phase (LTT) [14].

$La_{2-x}Ba_xCuO_4$ (LBCO) is considered as the most charge-ordered cuprate. Especially, at $x = 1/8$ CDW is the strongest with its correlation length reaching hundreds of lattice parameters, and superconductivity is highly suppressed with $T_c \sim 4$ K, commonly referred to as the $\frac{1}{8}$-anomaly (Fig. 1.6). While its detailed properties near $x \sim 1/8$ are relatively well-characterized by previous resonant x-ray scattering experiments [25, 31–33], the behavior of CDW under the presence of coexisting superconductivity has not been studied in-depth due to low T_c. At optimal dopings $x = 0.095$ and 0.155, T_c is enhanced up to 30 K; however, CDW is expected to be fluctuating, or "glassy", that is short-ranged with small structure factor spread over a wide range of momenta. To study CDW at the optimal doping, it requires a technique that provides a better detection sensitivity than conventional x-ray scattering techniques. We developed an experimental scheme of detecting CDW using resonant soft x-ray scattering by utilizing a transition-edge sensor detector, presented in Chapter 5. We showed that employing the energy-resolving detector improves the statistical quality of the data compared to a conventional energy-integrated measurement. The application of the scheme was performed on detecting fluctuating orders in LBCO $x = 0.155$ and the preliminary results are presented together. In addition, we performed a time-resolved resonant soft x-ray scattering experiment on CDW in LBCO $x = 0.125$ to study its dynamics, and the result is presented in Chapter 6. We showed that, even though it is believed to be static at $x = 0.125$ when it is most stable, the dynamics of the charge order are relaxational, exhibiting gapless collective excitations.

Chapter 2

Experimental methods

2.1 Basic theory of x-ray scattering

2.1.1 Structure factor $S(q)$

X-ray scattering is the most commonly used technique to characterize the structure of solids. The distribution of x-rays scattered by a material contains information of the periodicity and symmetry of the arrangement of atoms. For crystalline materials, sharp peaks of scattering are observed, which can be explained as the result of constructive interference of reflected rays from successive crystal planes. This formulation is described by the well-known Bragg condition, $n\lambda = 2d\sin\theta$, where n is the order of the interference, λ is the wavelength of the incident x-ray, d is the interplanar distance, and θ is the angle of incidence.

Another way to view the scattering is provided by the Laue formulation, in which the atoms in a solid are considered as point scatterers and reradiate the incident radiation in all directions [34]. Consider a scattering process where incident rays with the wavevector $\boldsymbol{k}$ is scattered to $\boldsymbol{k}'$ by point scatterers at positions $\boldsymbol{r}_1, ..., \boldsymbol{r}_n$. The amplitudes of the rays scattered at each scatterer are in the ratios $e^{i\boldsymbol{q}\cdot\boldsymbol{r}_1}, ..., e^{i\boldsymbol{q}\cdot\boldsymbol{r}_n}$, where $\boldsymbol{q} = \boldsymbol{k}' - \boldsymbol{k}$ is the change in wavevector. Following this formulation, the scattering amplitude from a solid will be proportional to the structure factor $S(\boldsymbol{q})$ that is written as

$$S(\boldsymbol{q}) = \sum_{j}^{\text{all atoms}} f_j(\boldsymbol{q}) e^{i\boldsymbol{q}\cdot\boldsymbol{r}_j}, \tag{2.1}$$

where f_j is the atomic form factor of the atom at $\boldsymbol{r}_j$. The intensity of the scattered rays will be proportional to the square of the amplitude, which will contain a factor $|S(\boldsymbol{q})|^2$.

Among many forms of materials, crystals are of particular interest in this study. Crystals are periodic structures composed of the lattice of unit cells and the arrangement of atoms (basis) within the unit cell.

Following Eq. (2.1), the scattering amplitude from a crystal can be described as

$$S^{\text{crystal}}(\boldsymbol{q}) = \sum_{\boldsymbol{R}_n+\boldsymbol{r}_j}^{\text{all atoms}} f_j(\boldsymbol{q}) e^{i\boldsymbol{q}\cdot(\boldsymbol{R}_n+\boldsymbol{r}_j)} = \sum_{n}^{\text{all unit cells}} e^{i\boldsymbol{q}\cdot\boldsymbol{R}_n} \sum_{j}^{\substack{\text{atoms within}\\ \text{a unit cell}}} f_j(\boldsymbol{q}) e^{i\boldsymbol{q}\cdot\boldsymbol{r}_j}, \tag{2.2}$$

where $\boldsymbol{R}_n$ is a lattice vector, and $\boldsymbol{r}_j$ is the position of an atom within the unit cell. The first term is a sum over the lattice and, in the limit that the number of unit cells goes to infinity, this term gains non-vanishing magnitude only if $\boldsymbol{q}$ coincides with a reciprocal lattice vector $\boldsymbol{G}$. This is the Laue condition, $\boldsymbol{q} = \boldsymbol{G}$, which can be shown to be equivalent to the Bragg condition. The second term is known as the unit cell structure factor. While this term alone cannot predict the absolute intensity of scattering, the unit cell structure factor provides important information of forbidden reflections, which is a characteristic of particular symmetry of the basis [34, 35].

In certain cases, some crystalline materials display a modulation that is incompatible with the lattice structure. That is, the position of the atoms is modulated with a wavelength that is a multiple of a lattice parameter, or equivalently a wavevector that is a fraction of a reciprocal lattice parameter. When the fraction can be expressed as a rational number, the material is said to possess a commensurate modulation. If the fraction is an irrational number, then the modulation is incommensurate and the material is not periodic. Still, it is possible to define an average, periodic lattice for incommensurate materials, and the scattering will consists of Bragg reflections from the average lattice and additional satellite reflections from the modulation [35]. This can be illustrated with a simple monatomic 1D chain model in which the positions of atoms are given by $x_n = an + u\cos(q_m an)$ where a is the lattice parameter, n is a integer index of atoms, u is the amplitude of the modulation, and $q_m = \frac{2\pi}{\lambda_m}$ is the wavevector associated with the modulation with the wavelength λ_m. The structure factor for the modulated 1D chain model can be written as

$$S_{\text{1D model}}(q) = \sum_n e^{iqx_n} = \sum_n e^{iq[an+u\cos(q_m an)]} = \sum_n e^{iqan} e^{iqu\cos(q_m an)}. \tag{2.3}$$

For simplicity, the atomic form factor has been set to unity. By making an approximation that the modulation amplitude u is small, we can expand the second phase factor and keep up to the second order term:

$$\begin{aligned} S_{\text{1D model}}(q) &\simeq \sum_n e^{iqan}[1 + iqu\cos(q_m an) + \cdots] \\ &= \sum_n e^{iqan} + i\frac{qu}{2} \sum_n \left[e^{i(q+q_m)an} + e^{i(q-q_m)an}\right]. \end{aligned} \tag{2.4}$$

In the limit that the number of atoms is large,

$$S_{\mathrm{1D\ model}}(q) = \frac{2\pi}{a}\sum_G \delta(q-G) + i\left(\frac{qu}{2}\right)\left(\frac{2\pi}{a}\right)\sum_G \left[\delta(q+q_m-G)+\delta(q-q_m-G)\right], \tag{2.5}$$

where the sum is over all reciprocal lattice vector G. The intensity distribution, which is proportional to $|S(q)|^2$, will exhibit the main peaks at $q = G$ due to the first term and the satellite peaks at $q = G \pm q_m$ due to the second term.

2.1.2 Atomic form factor $f(q,\omega)$

In the classical description of the elastic scattering of x-ray photons whose energy is greater than the binding energy of atomic electrons, so that the electrons can be treated as free electrons, the atomic form factor is simply the Fourier transform of the electronic charge distribution:

$$f_j^0(\boldsymbol{q}) = \int \rho_j(\boldsymbol{r}) e^{i\boldsymbol{q}\cdot\boldsymbol{r}} d\boldsymbol{r}, \tag{2.6}$$

where ρ_j is the electron number density of the atom at $\boldsymbol{r}_j$. Note that, in the limit of a small wavevector change, $f_j^0(\boldsymbol{q} \to 0) = Z$, where Z is the number of electrons in the atom. This particular case of elastic scattering described by f^0 term is commonly referred to as Thomson scattering.

When the energy of x-ray is smaller than or close to the binding energy of atomic electrons, corrections have to be made to the atomic form factor as the free electron approximation no longer holds. The atomic form factor can be generalized to be complex, allowing absorption processes included, that is written in the form

$$f(\boldsymbol{q},\omega) = f^0(\boldsymbol{q}) + f'(\omega) + if''(\omega), \tag{2.7}$$

where f' and f'' are the real and imaginary parts of the dispersion corrections, and also known as the resonant scattering terms. In a classical picture, the electrons are allowed to respond to the driving field of the x-ray as damped harmonic oscillators with an associated resonant frequency ω_s and a damping constant Γ. When a single oscillator is considered, it can be shown that the scattering amplitude is written as

$$\begin{aligned} f_s = \frac{\omega^2}{\omega^2-\omega_s^2+i\omega\Gamma} = \frac{\omega^2-\omega_s^2+i\omega\Gamma+\omega_s^2-i\omega\Gamma}{\omega^2-\omega_s^2+i\omega\Gamma} &= 1 + \frac{\omega_s^2-i\omega\Gamma}{\omega^2-\omega_s^2+i\omega\Gamma} \\ &\simeq 1 + \frac{\omega_s^2}{\omega^2-\omega_s^2+i\omega\Gamma}, \end{aligned} \tag{2.8}$$

where the fact that Γ is usually much less than ω_s is used in the last step. When the energy of x-ray is much bigger than the resonant energy, $\omega \gg \omega_s$, the electron can be considered to be free, and the Thomson scattering expression is recovered, that is $f_s = 1$. The second term of Eq. (2.8) is the dispersion correction, whose real and imaginary parts are given by

$$f_s' = \frac{\omega_s^2(\omega^2 - \omega_s^2)}{(\omega^2 - \omega_s^2)^2 + (\omega\Gamma)^2},\ f_s'' = -\frac{\omega_s^2\omega\Gamma}{(\omega^2 - \omega_s^2)^2 + (\omega\Gamma)^2}, \tag{2.9}$$

where the subscript s is to denote that this result is for the single oscillator model [35]. Note that Thomson scattering is always present regardless of the energy of x-ray, and the Thomson and resonant scatterings can interfere with one another.

While this model has a single resonance frequency $\omega = \omega_s$, in a real situation electrons can be excited to a continuum of free states above the absorption edge and each of these states can be associated with a different characteristic frequency ω_s. For this reason, in order to adequately describe the atomic x-ray absorption process a superposition of oscillators with relative weights $g(\omega_s)$ should be considered, which leads to

$$f'(\omega) = \sum_s g(\omega_s) f_s'(\omega_s, \omega),\ f''(\omega) = \sum_s g(\omega_s) f_s''(\omega_s, \omega). \tag{2.10}$$

The resonant part of the atomic form factor $f' + if''$ can be determined from experimental data of frequency dependence of x-ray absorption. The absorption coefficient μ is the quantity that is typically measured from experiments, which is related to the absorption cross section σ_a by

$$\mu = \sum_j \rho_{\text{at},j}\sigma_{a,j} \tag{2.11}$$

where $\rho_{\text{at},j}$ and $\sigma_{a,j}$ is the atomic number density and the absorption cross section, respectively, of the atom of type j. From experimentally determined $\sigma_a(\omega)$, the imaginary part of the form factor $f''(\omega)$ can be determined through

$$f''(\omega) = -\left(\frac{\omega}{4\pi c}\right)\sigma_a(\omega). \tag{2.12}$$

Once f'' is determined, the real part f' can be obtained using the relationships that exist between f' and f'':

$$f'(\omega) = \frac{2}{\pi}\mathcal{P}\int_0^\infty \frac{\omega' f''(\omega')}{\omega'^2 - \omega^2}d\omega',\ f''(\omega) = -\frac{2\omega}{\pi}\mathcal{P}\int_0^\infty \frac{f'(\omega')}{\omega'^2 - \omega^2}d\omega'. \tag{2.13}$$

These are known as Kramers-Kronig relations which can be used to compute the real part from the imaginary part (or vice versa) of response functions in physical systems [35].

2.1.3 Quantum mechanical description of scattering

Consider a scattering process, taking place in a box of side L and volume $V = L^3$, from a photon state $(\boldsymbol{k}, \alpha)$ to a state $(\boldsymbol{k}', \alpha')$ and let the initial sample state be written as A and the final state by B. The differential cross section for this process into a solid angle element $d\Omega$ is defined by

$$\frac{d\sigma}{d\Omega} = \frac{1}{\Phi}\frac{1}{d\Omega} w_{d\Omega} \tag{2.14}$$

where $w_{d\Omega}$ is the transition probability per unit time into $d\Omega$, and Φ is the incident photon flux which is just c/V since there is one photon in the normalization box of volume V. For a photon emitted into $d\Omega$, the number of allowed states in an energy interval $[E, E + dE]$, where $E = \hbar\omega = \hbar c|\boldsymbol{k}|$, can be written as $\rho_{E,d\Omega} dE$. Assuming the periodic boundary condition and that the normalization volume becomes infinite, the allowed photon states form a continuous energy spectrum, and $\rho_{E,d\Omega}$ is given by [36]

$$\rho_{E,d\Omega} = \frac{V\omega^2}{(2\pi)^3}\frac{d\Omega}{\hbar c^3}. \tag{2.15}$$

For a given interaction Hamiltonian H_{int}, $w_{d\Omega}$ can be obtained from the time-dependent perturbation theory,

$$w_{d\Omega} = \int \left(|c^{(1)} + c^{(2)} + \cdots|^2/t \right) \rho_{E,d\Omega} dE \tag{2.16}$$

where $c^{(1)}$ and $c^{(2)}$ are the first and second order terms of the transition amplitude from state $|A; \boldsymbol{k}, \alpha\rangle$ at $t = 0$ to state $|B; \boldsymbol{k}', \alpha'\rangle$ at a later time t, that are given by

$$c^{(1)}(t) = \frac{1}{i\hbar}\int_0^t dt_1 \langle B; \boldsymbol{k}', \alpha'| H_{\text{int}}(t_1) |A; \boldsymbol{k}, \alpha\rangle \, e^{i(E_B - E_A)t_1/\hbar} \tag{2.17}$$

$$\begin{aligned} c^{(2)}(t) &= \frac{1}{i\hbar}\sum_I \int_0^t dt_2 \langle B; \boldsymbol{k}', \alpha'| H_{\text{int}}(t_2) |I\rangle \, e^{i(E_B - E_I)t_2/\hbar} c_I^{(1)}(t_2) \\ &= \frac{1}{(i\hbar)^2}\sum_I \int_0^t dt_2 \int_0^{t_2} dt_1 \langle B; \boldsymbol{k}', \alpha'| H_{\text{int}}(t_2) |I\rangle \, e^{i(E_B - E_I)t_2/\hbar} \langle I| H_{\text{int}}(t_1) |A; \boldsymbol{k}, \alpha\rangle \, e^{i(E_I - E_A)t_1/\hbar} \end{aligned} \tag{2.18}$$

where I is an intermediate state [37].

The Hamiltonian for a system of non-relativistic electrons interacting with an electromagnetic field is given by

$$H = \frac{1}{2m}\sum_i \left[\boldsymbol{p}_i - \frac{e}{c}\boldsymbol{A}(\boldsymbol{r}_i, t)\right] \cdot \left[\boldsymbol{p}_i - \frac{e}{c}\boldsymbol{A}(\boldsymbol{r}_i, t)\right] + \sum_i V(\boldsymbol{r}_i), \tag{2.19}$$

where the sum is over all electrons. The vector potential $\boldsymbol{A}$ can be written as

$$\boldsymbol{A}(\boldsymbol{r},t)=\frac{1}{\sqrt{V}}\sum_{k,\alpha}c\sqrt{\frac{\hbar}{2\omega}}[a_{\boldsymbol{k},\alpha}\boldsymbol{\epsilon}_\alpha e^{i\boldsymbol{k}\cdot\boldsymbol{r}-i\omega t}+a^\dagger_{\boldsymbol{k},\alpha}\boldsymbol{\epsilon}^*_\alpha e^{-i\boldsymbol{k}\cdot\boldsymbol{r}+i\omega t}] \tag{2.20}$$

where $a^\dagger_{\boldsymbol{k},\alpha}$ and $a_{\boldsymbol{k},\alpha}$ are, respectively, photon creation and annihilation operators for the photon with wavevector $\boldsymbol{k}$ and polarization α, and $\boldsymbol{\epsilon}_\alpha$ is a polarization vector. By expanding Eq. (2.19), we obtain $H=H_{\text{el}}+H^{(1)}_{\text{int}}+H^{(2)}_{\text{int}}$ where

$$H_{\text{el}}=\sum_i\left[\frac{\boldsymbol{p}_i}{2m}+V(\boldsymbol{r}_i)\right] \tag{2.21}$$

$$H^{(1)}_{\text{int}}=-\frac{e}{2mc}\sum_i[\boldsymbol{p}_i\cdot\boldsymbol{A}(\boldsymbol{r}_i,t)+\boldsymbol{A}(\boldsymbol{r}_i,t)\cdot\boldsymbol{p}_i] \tag{2.22}$$

$$H^{(2)}_{\text{int}}=\frac{e^2}{2mc^2}\sum_i\boldsymbol{A}(\boldsymbol{r}_i,t)\cdot\boldsymbol{A}(\boldsymbol{r}_i,t). \tag{2.23}$$

The term $H^{(1)}_{\text{int}}$ is linear in $a^\dagger_{\boldsymbol{k},\alpha}$ and $a_{\boldsymbol{k},\alpha}$, which means that in the first order perturbation theory $H^{(1)}_{\text{int}}$ contributes to one-photon absorption or emission, and only in the second order to scattering. The term $H^{(2)}_{\text{int}}$ is quadratic in $a^\dagger_{\boldsymbol{k},\alpha}$ and $a_{\boldsymbol{k},\alpha}$, and will contribute to scattering in the first order via $a^\dagger a$ and $aa^\dagger$ terms [36,37].

For simplicity, consider the scattering by a one-electron atom. Following Eq. (2.17) and (2.23), the first order transition amplitude is given by

$$\begin{aligned}
c^{(1)}(t)=&\frac{1}{i\hbar}\int_0^t dt_1\,\langle B;\boldsymbol{k'},\alpha'|\,H^{(2)}_{\text{int}}(t_1)\,|A;\boldsymbol{k},\alpha\rangle\,e^{i(E_B-E_A)t_1/\hbar}\\
=&\frac{1}{i\hbar}\frac{e^2}{2mc^2}\frac{c^2\hbar}{2V\sqrt{\omega\omega'}}\int_0^t dt_1\,\langle B;\boldsymbol{k'},\alpha'|\,(a_{\boldsymbol{k},\alpha}a^\dagger_{\boldsymbol{k'},\alpha'}+a^\dagger_{\boldsymbol{k'},\alpha'}a_{\boldsymbol{k},\alpha})\boldsymbol{\epsilon}^*_{\alpha'}\cdot\boldsymbol{\epsilon}_\alpha\\
&\qquad\qquad\times e^{\left[i(\boldsymbol{k}-\boldsymbol{k'})\cdot\boldsymbol{r}-i(\omega-\omega')t_1\right]}\,|A;\boldsymbol{k},\alpha\rangle\,e^{i(E_B-E_A)t_1/\hbar}\\
=&\frac{1}{i\hbar}\frac{e^2}{2mc^2}\frac{c^2\hbar}{2V\sqrt{\omega\omega'}}2\delta_{AB}\boldsymbol{\epsilon}^*_{\alpha'}\cdot\boldsymbol{\epsilon}_\alpha\int_0^t dt_1\exp[i(\hbar\omega'+E_B-\hbar\omega-E_A)t_1/\hbar]
\end{aligned} \tag{2.24}$$

with $\omega=|\boldsymbol{k}|c$ and $\omega'=|\boldsymbol{k'}|c$, where $e^{i\boldsymbol{k}\cdot r}$ and $e^{-i\boldsymbol{k'}\cdot r}$ are replaced by 1, since in the long-wavelength approximation the atomic electron may be assumed to be situated at the origin (which is equivalent to the dipole approximation).

For the second order contribution of $\boldsymbol{A}\cdot\boldsymbol{p}$ terms in Eq. (2.22), there are two types of transition processes that are possible. In the first type, the atomic state A first absorb the incident photon $(\boldsymbol{k},\alpha)$ at an earlier time t_1 and becomes state I, and subsequently at a later time t_2 the atomic state I emits the outgoing photon $(\boldsymbol{k'},\alpha')$ and changes into state B. In the second type, state A first emits the outgoing photon at t_1 and changes into state I, and subsequently at t_2 state I absorbs the incident photon and becomes state

B [37]. These processes are reflected in the second order transition amplitude, following Eq. (2.18) and (2.22),

$$
\begin{aligned}
c^{(2)}(t) =& \frac{1}{(i\hbar)^2}\frac{c^2\hbar}{2V\sqrt{\omega\omega'}}\left(-\frac{e}{mc}\right)^2\int_0^t dt_2\int_0^{t_2} dt_1 \\
&\times \Bigg[\sum_I \langle B;\boldsymbol{k}',\alpha'|\, a^\dagger_{\boldsymbol{k}',\alpha'}\boldsymbol{p}\cdot\boldsymbol{\epsilon}^*_{\alpha'}e^{-i\boldsymbol{k}'\cdot\boldsymbol{r}+\omega' t_2}\,|I\rangle\, e^{i(E_B-E_I)t_2/\hbar} \\
&\times \langle I|\, a_{\boldsymbol{k},\alpha}\boldsymbol{p}\cdot\boldsymbol{\epsilon}_\alpha e^{i\boldsymbol{k}\cdot\boldsymbol{r}-\omega t_1}\,|A;\boldsymbol{k},\alpha\rangle\, e^{i(E_I-E_A)t_1/\hbar} \\
&+\sum_I \langle B;\boldsymbol{k}',\alpha'|\, a_{\boldsymbol{k},\alpha}\boldsymbol{p}\cdot\boldsymbol{\epsilon}_\alpha e^{i\boldsymbol{k}\cdot\boldsymbol{r}-\omega t_2}\,|I;\boldsymbol{k}',\alpha';\boldsymbol{k},\alpha\rangle\, e^{i(E_B-E_I)t_2/\hbar} \\
&\times \langle I;\boldsymbol{k}',\alpha';\boldsymbol{k},\alpha|\, a^\dagger_{\boldsymbol{k}',\alpha'}\boldsymbol{p}\cdot\boldsymbol{\epsilon}^*_{\alpha'}e^{-i\boldsymbol{k}'\cdot\boldsymbol{r}+\omega' t_1}\,|A;\boldsymbol{k},\alpha\rangle\, e^{i(E_I-E_A)t_1/\hbar}\Bigg] \\
=&-\frac{c^2\hbar}{i\hbar 2V\sqrt{\omega\omega'}}\left(\frac{e}{mc}\right)^2\sum_I\left(\frac{\langle B|\,\boldsymbol{p}\cdot\boldsymbol{\epsilon}^*_{\alpha'}\,|I\rangle\,\langle I|\,\boldsymbol{p}\cdot\boldsymbol{\epsilon}_\alpha\,|A\rangle}{E_I-E_A-\hbar\omega}+\frac{\langle B|\,\boldsymbol{p}\cdot\boldsymbol{\epsilon}_\alpha\,|I\rangle\,\langle I|\,\boldsymbol{p}\cdot\boldsymbol{\epsilon}^*_{\alpha'}\,|A\rangle}{E_I-E_A+\hbar\omega'}\right) \\
&\times\int_0^{t_2} dt_2 \exp[i(E_B-E_A+\hbar\omega'-\hbar\omega)t_2/\hbar],
\end{aligned}
\tag{2.25}
$$

where the dipole approximation is made. Combining $c^{(1)}(t)$ and $c^{(2)}(t)$, we have the transition probability $w_{d\Omega}=\int\left(|c^{(1)}+c^{(2)}|^2/t\right)\rho_{E,d\Omega}dE$, and it can be shown that we have for the differential cross section

$$
\frac{d\sigma}{d\Omega}=r_0^2\left(\frac{\omega'}{\omega}\right)\left|\delta_{AB}\boldsymbol{\epsilon}^*_{\alpha'}\cdot\boldsymbol{\epsilon}_\alpha-\frac{1}{m}\sum_I\left(\frac{\langle B|\,\boldsymbol{p}\cdot\boldsymbol{\epsilon}^*_{\alpha'}\,|I\rangle\,\langle I|\,\boldsymbol{p}\cdot\boldsymbol{\epsilon}_\alpha\,|A\rangle}{E_I-E_A-\hbar\omega-i\Gamma_I/2}+\frac{\langle B|\,\boldsymbol{p}\cdot\boldsymbol{\epsilon}_\alpha\,|I\rangle\,\langle I|\,\boldsymbol{p}\cdot\boldsymbol{\epsilon}^*_{\alpha'}\,|A\rangle}{E_I-E_A+\hbar\omega'}\right)\right|^2, \tag{2.26}
$$

where the condition $E_B-E_A+\hbar\omega'-\hbar\omega=0$ must satisfy, and r_0 stands for the classical radius of the electron, $r_0=e^2/4\pi mc^2$. Here, the additional term $\Gamma_I=\hbar/\tau_I$ is introduced to take the instability of the intermediate state I due to spontaneous emission into account,τ_I being the finite lifetime of state I [37]. This expression of the cross section is also known as the Kramers-Heisenberg formula. Each of the three terms in Eq. (2.26) represents the scattering process displayed in Fig. 2.1.

When the energy of the incident photon satisfies the condition $E_I-E_A\simeq\hbar\omega$ for a specific intermediate state I, the resonant term in Eq. (2.26) becomes dominant that is given by

$$
\left(\frac{d\sigma}{d\Omega}\right)_{\text{res.}}=r_0^2\left(\frac{\omega'}{\omega}\right)\left(\frac{1}{m^2}\right)\left|\frac{\langle B|\,\boldsymbol{p}\cdot\boldsymbol{\epsilon}^*_{\alpha'}\,|I\rangle\,\langle I|\,\boldsymbol{p}\cdot\boldsymbol{\epsilon}_\alpha\,|A\rangle}{E_I-E_A-\hbar\omega-i\Gamma_I/2}\right|^2, \tag{2.27}
$$

since the real part of the denominator becomes zero, making the magnitude of the term very large. This term is the quantum mechanical origin of resonant scattering. The resonant scattering term is strongly energy-dependent and peaked around the energy of the electronic transition. This enhancement of the scattering typically realized at an absorption edge, when core electrons absorb incident photons and becomes excited

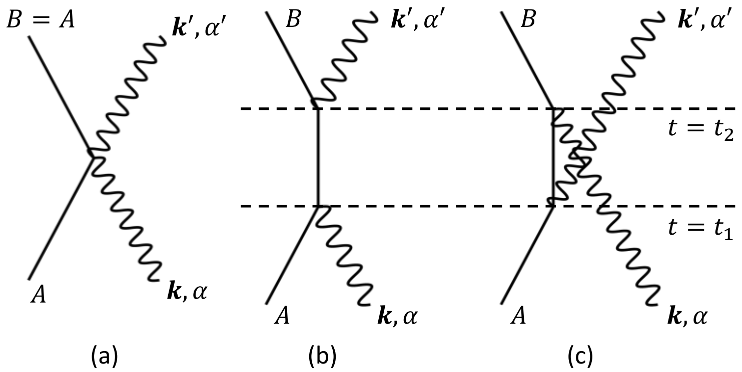

Figure 2.1: Feynman diagrams for scattering of light. Each diagram represents (a) the $\boldsymbol{A} \cdot \boldsymbol{A}$ interaction, (b) the first, and (c) the second type of the second order $\boldsymbol{A} \cdot \boldsymbol{p}$ interaction.

to valence states. Thus, it provides a great sensitivity to, for example, a small modulation of charge density in a valence band [22, 35, 37].

Note that Eq. (2.26) provides the quantum mechanical description of the origin of the complex expression of the atomic form factor, given by Eq. (2.7). By definition, the relation between the atomic form factor f and the differential cross section of the scattering by an atom is given by

$$\frac{d\sigma}{d\Omega} = |f|^2. \tag{2.28}$$

Comparing Eq. (2.28) to (2.26), we find that f can be written as

$$f(\omega, \boldsymbol{\epsilon}_\alpha, \boldsymbol{\epsilon}_{\alpha'}) = f^0(\boldsymbol{\epsilon}_\alpha, \boldsymbol{\epsilon}_{\alpha'}) + f'(\omega, \boldsymbol{\epsilon}_\alpha, \boldsymbol{\epsilon}_{\alpha'}) + if''(\omega, \boldsymbol{\epsilon}_\alpha, \boldsymbol{\epsilon}_{\alpha'}), \tag{2.29}$$

where f^0 is the Thomson scattering term, being the same as the classical expression in Eq. (2.6) in the long-wavelength approximation, and $f' + if''$ is the dispersion correction terms. Here, we can see that f explicitly depends on the polarizations of the incoming and outgoing photons. Rather than a scalar quantity given as Eq. (2.7), the atomic form factor can be written as a tensor in the basis of the polarization vectors,

$$\hat{f}(\omega) = \begin{pmatrix} f_{xx}(\omega) & f_{yx}(\omega) & f_{zx}(\omega) \\ f_{xy}(\omega) & f_{yy}(\omega) & f_{zy}(\omega) \\ f_{xz}(\omega) & f_{yz}(\omega) & f_{zz}(\omega) \end{pmatrix}, \tag{2.30}$$

and $\hat{f}$ is related to f by

$$f(\omega, \boldsymbol{\epsilon}_\alpha, \boldsymbol{\epsilon}_{\alpha'}) = \boldsymbol{\epsilon}^*_{\alpha'} \cdot \hat{f} \cdot \boldsymbol{\epsilon}_\alpha. \tag{2.31}$$

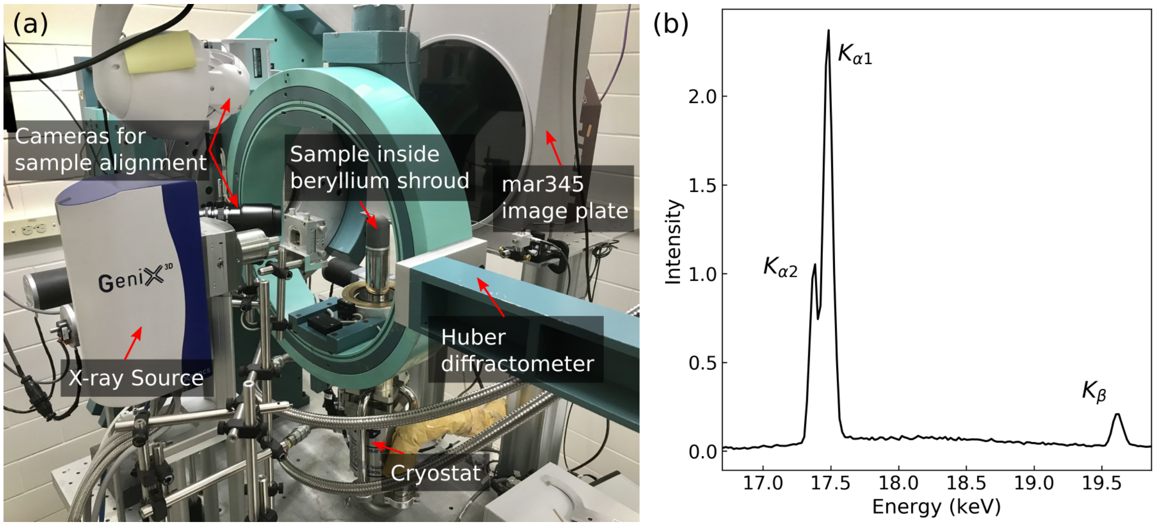

Figure 2.2: (a) The in-lab x-ray instrument at the University of Illinois. (b) Energy spectrum of the Mo K_α x-ray source measured from the angular dispersion of Si 333 Bragg reflection.

Charge scattering does not change the polarization of the incident photon and its contribution appears on the diagonal elements of this tensor, but magnetic scattering contributions can appear on on- and off-diagonal elements, depending on the direction of the local magnetization and the crystal symmetry [38, 39].

2.2 Hard x-ray diffraction

2.2.1 Overview

Structural studies of various single crystals were carried out using the in-lab x-ray instrument at the University of Illinois [Fig. 2.2(a)]. The instrument is equipped with a Xenocs GeniX3D Mo K_α microspot x-ray source with multilayer focusing optics, providing 2.5×10^7 photons/sec in a beam spot of 130 μm at the sample position. As shown in Fig. 2.2(b), the radiation spectrum of the x-ray source shows the most intense peak at $E = 17.48$ keV that corresponds to Mo $K_{\alpha1}$ emission and experiments were performed using this x-ray. In addition to $K_{\alpha1}$ radiation, the source radiates $K_{\alpha2}$ and K_β x-rays and the signals from these x-rays were excluded from data analysis.

Samples were cooled using a closed-cycle helium cryostat (ARS DE-202) with a base temperature of 5 K. Sample motion was done with a Huber four-circle diffractometer and a custom-made cryostat carrier that allows translational motions. Diffraction signals were collected using a Mar345 image plate detector. With the large active area (diameter of 345 mm) and single-photon sensitivity, the detector enables a full-3D reciprocal space mapping of, typically, more than 20 Brillouin zones. This instrument has successfully

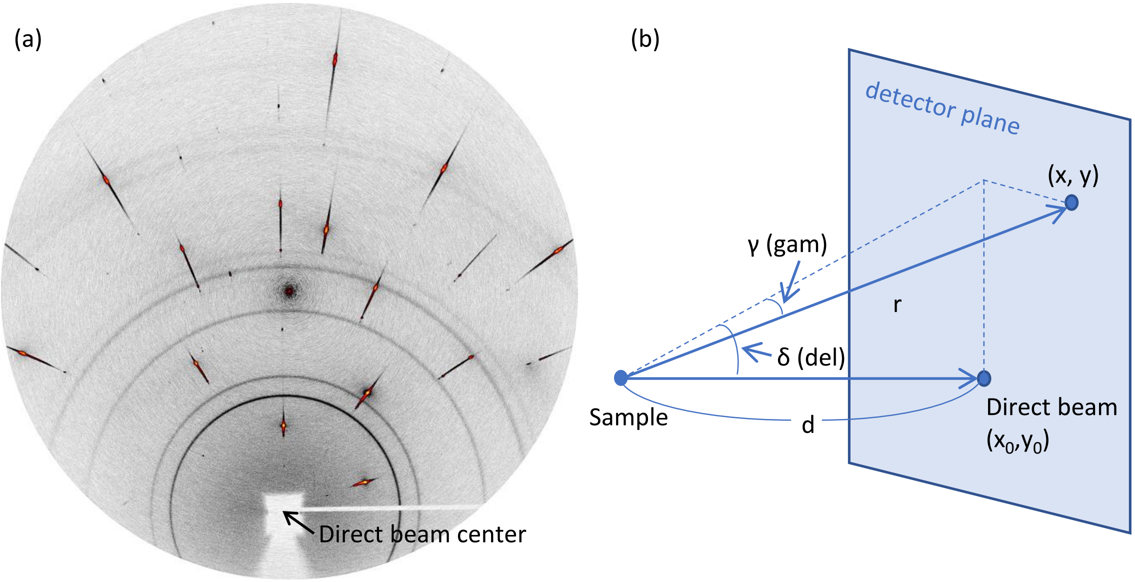

Figure 2.3: (a) Typical angle-integrated diffraction pattern. Bright spots are Bragg reflections from the sample. Direct beam is blocked by the beam-stop. Concentric rings centered at the direct beam center are powder diffraction patterns from the sample holder. (b) Schematic drawing showing the geometrical relationship between the pixel on the detector (x, y) and the detector angle δ and γ in the six-circle diffraction geometry.

measured structural phase transitions and CDW orders in various nickel-pnictide materials and transition metal dichalcogenide materials.

2.2.2 Reciprocal space mapping

Reciprocal space mappings were done by taking diffraction images at different sample angles of θ and mapping each pixel of the images to the corresponding position in the reciprocal space. Typically, for a single data set, 600 images were taken at sample angles θ from 0° to 30° with 0.05° increment step [Fig. 2.3(a)]. Each pixel of the images can be parametrized with (x, y, n) where x and y are the coordinates of the pixel and n is the image number that is related with the sample angle at which the image is taken, $\theta = n \times 0.05$.

In order to obtain the relationship between the pixel coordinate (x, y, n) and the reciprocal space coordinates $\boldsymbol{H} = (H, K, L)$, it is convenient to employ the six-circle diffraction geometry [40]. In the six-circle geometry, the detector position is determined with two angles: the in-plane angle δ and the out-of-plane angle γ. As described in [Fig. 2.3(b)], the pixel coordinate x and y can be expressed in terms of δ and γ as

$$\delta = \tan^{-1}\frac{y - y_0}{d}, \quad \gamma = \sin^{-1}\frac{x - x_0}{r}, \tag{2.32}$$

where (x_0, y_0) is the direct beam position on the detector, d is the distance from the sample to the detector, and r is the distance from the sample to the pixel (x, y), that is $r = \sqrt{(x - x_0)^2 + (y - y_0)^2 + d^2}$. Now we can express the pixel coordinate (x, y, n) with the set of angles (θ, δ, γ). Using the basic diffraction equation for the six-circle diffractometer [40], we can obtain $\boldsymbol{H}$ that is given by

$$\boldsymbol{H} = (\Omega X \Phi U B)^{-1}(\Delta\Gamma - A^{-1})\boldsymbol{K}_{\mathrm{i,lab}}, \tag{2.33}$$

where UB is the orientation matrix that describes the sample orientation with respect to the diffractometer angles [41], which can be easily calculated using the scientific diffraction software SPEC [42], and

$$A = \begin{pmatrix} 1 & 0 & 0 \\ 0 & \cos\alpha & -\sin\alpha \\ 0 & \sin\alpha & \cos\alpha \end{pmatrix}, \ \Gamma = \begin{pmatrix} 1 & 0 & 0 \\ 0 & \cos\gamma & -\sin\gamma \\ 0 & \sin\gamma & \cos\gamma \end{pmatrix}, \ X = \begin{pmatrix} \cos\chi & 0 & \sin\chi \\ 0 & 1 & 0 \\ -\sin\chi & 0 & \cos\chi \end{pmatrix},$$

$$\Delta = \begin{pmatrix} \cos\delta & \sin\delta & 0 \\ -\sin\delta & \cos\delta & 0 \\ 0 & 0 & 1 \end{pmatrix}, \ \Omega = \begin{pmatrix} \cos\omega & \sin\omega & 0 \\ -\sin\omega & \cos\omega & 0 \\ 0 & 0 & 1 \end{pmatrix}, \ \Phi = \begin{pmatrix} \cos\phi & \sin\phi & 0 \\ -\sin\phi & \cos\phi & 0 \\ 0 & 0 & 1 \end{pmatrix}$$

where $\alpha = \phi = 0$, $\chi = 90°$, and $\omega = \theta$ for this case. Once the reciprocal space coordinates $\boldsymbol{H}$ are determined for every pixel, the reciprocal space map can be constructed by mapping the intensity of each pixel to the corresponding reciprocal space point.

2.2.3 Momentum resolution

The momentum resolution of the x-ray instrument can be obtained using a geometric construction method presented. The momentum resolution is determined by three parameters: the energy bandwidth of the x-ray source, the beam divergence, and the opening angle of the detector. First, consider a scattering geometry in

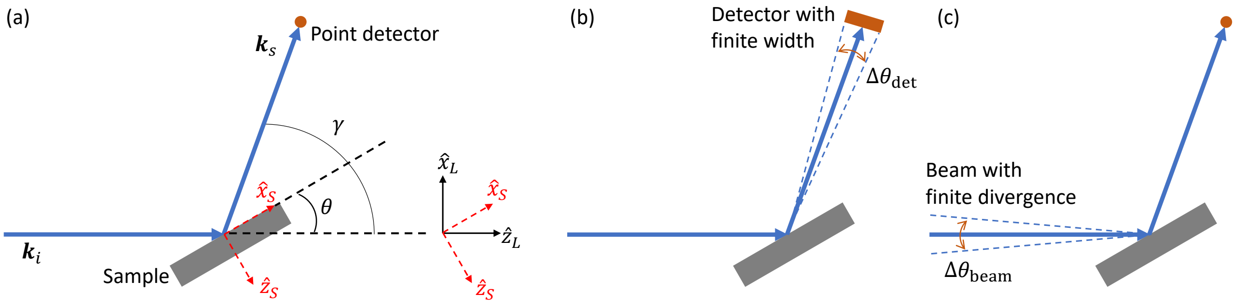

Figure 2.4: Schematic drawings of scattering geometries with (a) a collimated beam and a point-detector with an infinitely small opening width, (b) a collimated beam and a detector with a finite width, and (c) a beam with a finite divergence and a point-detector.

an ideal case with a perfectly monochromatic, collimated beam and a point-detector with an infinitesimal opening angle, as shown in Fig. 2.4(a). The scattering angle is γ and the sample angle is θ. $\hat{x}_L$ and $\hat{z}_L$ are the laboratory coordinate axes, and $\hat{x}_S$ and $\hat{z}_S$ are the sample coordinate axes. The sample coordinate system is rotated by $-\frac{\pi}{2}+\theta$ from the laboratory coordinate system about its y-axis. The wavevectors of the incident and scattered rays in the laboratory coordinate are given by

$$\boldsymbol{k}_i = k_0(0,0,1), \quad \boldsymbol{k}_s = k_0(\sin\gamma, 0, \cos\gamma), \tag{2.34}$$

where k_0 is the magnitude of the monochromatic x-ray wavevector. The momentum transfer of the scattering process is

$$\boldsymbol{q} = \boldsymbol{k}_i - \boldsymbol{k}_s = k_0(-\sin\gamma, 0, 1-\cos\gamma). \tag{2.35}$$

The momentum transfer vector in the sample coordinate can be obtained as $\boldsymbol{q}_s = U\boldsymbol{q}$ where U is a unitary rotation matrix

$$U = \begin{pmatrix} \cos(\frac{\pi}{2}-\theta) & 0 & \sin(\frac{\pi}{2}-\theta) \\ 0 & 1 & 0 \\ -\sin(\frac{\pi}{2}-\theta) & 0 & \cos(\frac{\pi}{2}-\theta) \end{pmatrix} = \begin{pmatrix} \sin\theta & 0 & \cos\theta \\ 0 & 1 & 0 \\ -\cos\theta & 0 & \sin\theta \end{pmatrix}, \tag{2.36}$$

and,

$$\begin{aligned} \boldsymbol{q}_s = U\boldsymbol{q} &= k_0(-\sin\gamma\sin\theta - \cos\gamma\cos\theta + \cos\theta, 0, \sin\gamma\cos\theta - \cos\gamma\sin\theta + \sin\theta) \\ &= k_0(-\cos(\gamma-\theta) + \cos\theta, 0, \sin(\gamma-\theta) + \sin\theta). \end{aligned} \tag{2.37}$$

Detector opening angle

Now, suppose the detector has a finite acceptance angle $\Delta\theta_{\text{det}}$ as shown in Fig. 2.4(b). The x-rays with the scattering angle of $\gamma + \beta_{\text{det}}$ with $-\Delta\theta_{\text{det}}/2 \le \beta_{\text{det}} \le \Delta\theta_{\text{det}}/2$ will be received by the detector. By replacing γ by $\gamma + \beta_{\text{det}}$ in Eq. (2.37),

$$\boldsymbol{q}_{s,\text{det}} = k_0(-\cos(\gamma-\theta+\beta_{\text{det}}) + \cos\theta, 0, \sin(\gamma-\theta+\beta_{\text{det}}) + \sin\theta). \tag{2.38}$$

Suppose we are on the Bragg condition, $\theta = \frac{\gamma}{2}$, then

$$\begin{aligned} \boldsymbol{q}_{s,\text{det}} &= k_0(-\cos(\frac{\gamma}{2}+\beta_{\text{det}}) + \cos\frac{\gamma}{2}, 0, \sin(\frac{\gamma}{2}+\beta_{\text{det}}) + \sin\frac{\gamma}{2}) \\ &= k_0(-\cos\frac{\gamma}{2}\cos\beta_{\text{det}} + \sin\frac{\gamma}{2}\sin\beta_{\text{det}} + \cos\frac{\gamma}{2}, 0, \sin\frac{\gamma}{2}\cos\beta_{\text{det}} + \cos\frac{\gamma}{2}\sin\beta_{\text{det}} + \sin\frac{\gamma}{2}). \end{aligned} \tag{2.39}$$

Since β_{det} is small, we can use $\sin\beta_{\mathrm{det}} \simeq \beta_{\mathrm{det}}$ and $\cos\beta_{\mathrm{det}} \simeq 1$ to obtain

$$\begin{aligned} \boldsymbol{q}_{s,\mathrm{det}} &\simeq k_0(\beta_{\mathrm{det}} \sin\frac{\gamma}{2}, 0, 2\sin\frac{\gamma}{2} + \beta_{\mathrm{det}}\cos\frac{\gamma}{2}) \\ &= 2k_0 \sin\frac{\gamma}{2}\left(\frac{\beta_{\mathrm{det}}}{2}, 0, 1 + \frac{\beta_{\mathrm{det}}}{2}\cot\frac{\gamma}{2}\right). \end{aligned} \tag{2.40}$$

Beam divergence

The effect of the finite beam divergence can be obtained in a similar manner. Suppose now the detector has an infinitesimal opening angle and the beam has a divergence angle of $\Delta\theta_{\mathrm{beam}}$. Then the wavevectors of the incident and scattered x-rays are

$$\boldsymbol{k}_i = k_0(\sin\beta_{\mathrm{beam}}, 0, \cos\beta_{\mathrm{beam}}), \quad \boldsymbol{k}_s = k_0(\sin\gamma, 0, \cos\gamma) \tag{2.41}$$

where $-\Delta\theta_{\mathrm{beam}}/2 \leq \beta_{\mathrm{beam}} \leq \Delta\theta_{\mathrm{beam}}/2$. The momentum transfer vector in the laboratory coordinate system is

$$\begin{aligned} \boldsymbol{q}_{\mathrm{beam}} = \boldsymbol{k}_i - \boldsymbol{k}_s &= k_0(\sin\beta_{\mathrm{beam}} - \sin\gamma, 0, \cos\beta_{\mathrm{beam}} - \cos\gamma) \\ &\simeq k_0(\beta_{\mathrm{beam}} - \sin\gamma, 0, 1 - \cos\gamma) \end{aligned} \tag{2.42}$$

where we used the approximation for the small β_{beam}. In the sample coordinate system,

$$\boldsymbol{q}_{s,\mathrm{beam}} = U\boldsymbol{q}_{\mathrm{beam}} = k_0(\beta_{\mathrm{beam}}\sin\theta + \cos\theta - \cos(\gamma-\theta), 0, -\beta_{\mathrm{beam}}\cos\theta + \sin\theta + \sin(\gamma-\theta)) \tag{2.43}$$

Again, using the Bragg condition $\theta = \frac{\gamma}{2}$,

$$\boldsymbol{q}_{s,\mathrm{beam}} = 2k_0\sin\frac{\gamma}{2}\left(\frac{\beta_{\mathrm{beam}}}{2}, 0, 1 - \frac{\beta_{\mathrm{beam}}}{2}\cot\frac{\gamma}{2}\right). \tag{2.44}$$

Beam energy bandwidth

The effect of the finite beam bandwidth Δk can be included by replacing k_0 in Eq. (2.40) and Eq. (2.44) by k whose range is $k_0 - \Delta k/2 \le k \le k_0 + \Delta k/2$,

$$\boldsymbol{q}_{s,\mathrm{det}}(k, \beta_{\mathrm{det}}) = 2k \sin\frac{\gamma}{2}\left(\frac{\beta_{\mathrm{det}}}{2}, 0, 1 + \frac{\beta_{\mathrm{det}}}{2}\cot\frac{\gamma}{2}\right) \tag{2.45}$$

$$\boldsymbol{q}_{s,\mathrm{beam}}(k, \beta_{\mathrm{beam}}) = 2k \sin\frac{\gamma}{2}\left(\frac{\beta_{\mathrm{beam}}}{2}, 0, 1 - \frac{\beta_{\mathrm{beam}}}{2}\cot\frac{\gamma}{2}\right). \tag{2.46}$$

The traces of $\boldsymbol{q}_{s,\mathrm{det}}$ and $\boldsymbol{q}_{s,\mathrm{beam}}$ will cover an area in momentum space, which represents the momentum resolution.

Figure 2.5 shows the traces of $\boldsymbol{q}_{s,\mathrm{det}}$ and $\boldsymbol{q}_{s,\mathrm{beam}}$ with $k_0 - \Delta k/2 \le k \le k_0 + \Delta k/2$, $-\Delta\theta_{\mathrm{det}}/2 \le \beta_{\mathrm{det}} \le \Delta\theta_{\mathrm{det}}/2$, and $-\Delta\theta_{\mathrm{beam}}/2 \le \beta_{\mathrm{beam}} \le \Delta\theta_{\mathrm{beam}}/2$. The blue area represents the trace of $\boldsymbol{q}_{s,\mathrm{det}}(k, \beta_{\mathrm{det}})$ and the green area represents the trace of $\boldsymbol{q}_{s,\mathrm{beam}}(k, \beta_{\mathrm{beam}})$. The overall momentum resolution (gray area) should combine the effect of the detector opening angle and the beam divergence, since the two effects are not independent. The energy bandwidth of the source is determined to be $\Delta E = 70$ eV ($\Delta k = k\Delta E/E = 0.03547 \mathring{A}^{-1}$), by fitting the $K_{\alpha 1}$ peak in the energy spectrum shown in Fig. 2.2(b) with a Gaussian function. The beam divergence is $\Delta\theta_{\mathrm{beam}} = 5$ mrad, and the opening angle of the detector is determined to be the angular acceptance of a single pixel $\Delta\theta_{\mathrm{det}} = 0.45$ mrad (= size of a pixel/sample-to-detector distance =

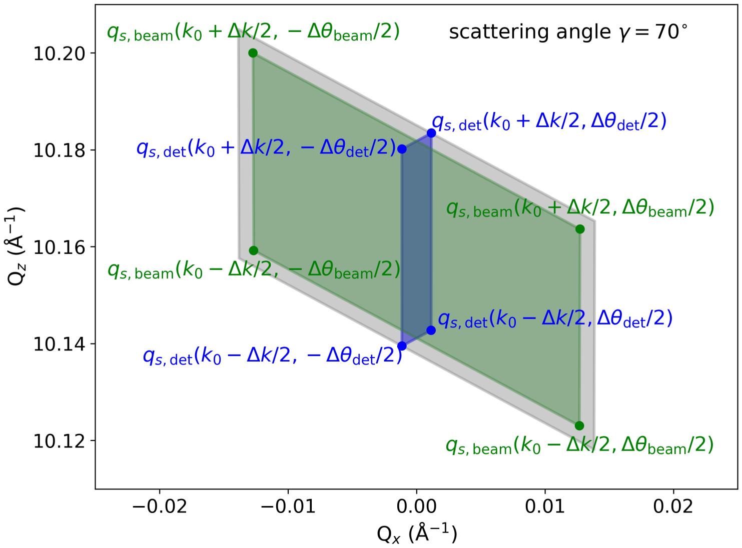

Figure 2.5: Schematic drawing of the momentum resolution at the scattering angle of $\gamma = 70^\circ$, with the experimentally determined values of Δk, $\Delta\theta_{\mathrm{det}}$, and $\Delta\theta_{\mathrm{beam}}$. Blue area represents the trace of $\boldsymbol{q}_{s,\mathrm{det}}(k, \beta_{\mathrm{det}})$ and Green area represents the trace of $\boldsymbol{q}_{s,\mathrm{beam}}(k, \beta_{\mathrm{beam}})$. Gray area represents the overall momentum resolution that combines the effect of the detector opening angle and the beam divergence.

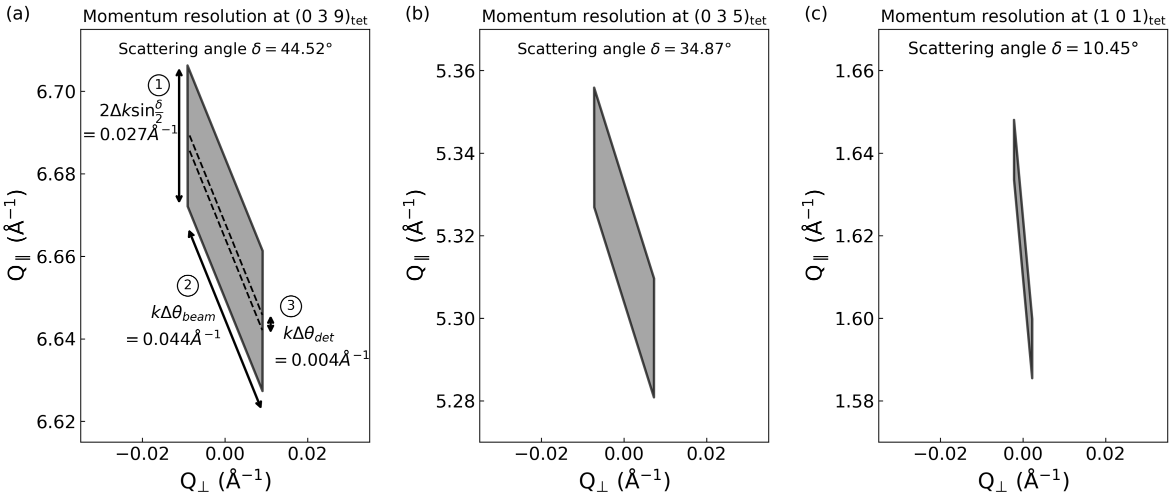

Figure 2.6: Momentum resolution function at three different Bragg reflection positions of $BaNi_2As_2$ at (a) $\boldsymbol{Q} = (0,3,9)_{\mathrm{tet}}$, (b) $\boldsymbol{Q} = (0,3,5)_{\mathrm{tet}}$, and (c) $\boldsymbol{Q} = (1,0,1)_{\mathrm{tet}}$. X- (Y-) axis is the momentum direction perpendicular (parallel) to the momentum transfer vector $\boldsymbol{Q}$ in each case. Each arrow represents the broadening of the resolution due to ① the energy bandwidth, ② the beam divergence, and ③ the detector opening.

100μm/225mm).

The momentum resolution varies depending on the location of the momentum space. As examples, Fig. 2.6 shows 2-D projections of the resolution functions to the detection plane for the cases of the $(0,3,9)_{\mathrm{tet}}$, $(0,3,5)_{\mathrm{tet}}$, and $(1,0,1)_{\mathrm{tet}}$ Bragg reflections of $BaNi_2As_2$ [43]. The projected resolution function has a shape of trapezoid whose dimensions vary from $0.01Å^{-1}$ to $0.08Å^{-1}$, depending on the scattering angle. The momentum resolution in a particular direction can be determined from the width of a line cut through the trapezoid along that direction.

2.3 Resonant soft x-ray scattering

2.3.1 Overview

Resonant soft x-ray scattering (RSXS) studies on CDW in cuprates presented in this thesis were mainly performed at three beamlines: Stanford Synchrotron Radiation Lightsource (SSRL) beamline 13-3, Advanced Photon Source (APS) beamline 29, Linac Coherent Light Source (LCLS) SXR beamline. Soft x-rays are very easily absorbed in air and water. Thus, in order to deliver light from the source to the sample and observe scattering, the entire endstation of soft x-ray beamlines must operate in ultra-high vacuum (UHV) condition, with its pressure being 10^{-8} Torr or lower. In addition, when the sample is at a cryogenic temperature, operating in UHV condition prevents the build-up of ice layers on the surface of the sample, which can seriously deteriorate scattering signals.

The scattering chambers enclose a diffractometer that is attached to a cryostat for cooling, and various types of detectors. For example, the scattering chamber at SSRL beamline 13-3 houses an in-vacuum four-circle diffractometer with a three-axis translation stage. The sample stage is attached to a continuous-flow helium cryostat through a copper braid and can be cooled to 23 K. For detection of x-rays, four detectors are installed inside the scattering chamber: a photodiode, a channeltron, a two-dimensional CCD detector, and a transition-edge sensor (TES) array detector. The photodiode has a wide dynamic range and is suitable for measuring strong signals such as a structural Bragg reflection or the direct beam. The channeltron is an electron multiplier that has a higher sensitivity compared to the photodiode, making it useful for detecting weak signals. The CCD detector has 1024×256 pixels (pixel size: 26×26 μm) and provides a detection of a wide area. The TES detector is an energy-resolving detector with a single-photon sensitivity and can be used for x-ray emission spectroscopy, resonant inelastic x-ray scattering experiments or rejecting fluorescence background in RSXS experiments (more information on TES detector is presented in chapter 5).

2.3.2 Sample preparation and alignment

For the case of cuprates, the penetration depth of lights in the soft x-ray range is less than 500 nm from the surface, and at resonance condition it becomes even smaller. Thus, it is important to prepare samples with good surface quality. LBCO and LESCO crystals grown by the floating zone method are typically in a cylindrical shape with the axial direction approximately being $(1, 1, 0)$ direction, and $(0, 0, 1)$ direction being in a radial direction. Since CDW in LBCO and LESCO lies in H-K plane and has a weak dependence on L direction, it is preferable to have the surface of the sample being the a-b plane and c-axis being perpendicular to the surface.

In order to obtain a surface of a-b plane, the direction of c-axis needs to be first identified. Orienting the crystal axes of the as-grown sample was performed using the back-scattering Laue diffraction instrument at Material Research Laboratory (MRL) at University of Illinois. When the c-axis is aligned parallel to the beam direction, the diffraction image displays a pattern with four-fold symmetry [Fig. 2.7(b)] that is inherited from the tetragonal structure of the crystal. Once the c-axis direction is determined, the sample was cleaved perpendicular to c-axis to reveal a fresh a-b plane. The cleaving was done by placing a razor blade perpendicular to the c-axis and hitting it gently with a hammer. When successful, the cleaved surface is flat and smooth, and reflects light very well [Fig. 2.7(a)]. The sample was glued with silver paint on a thin aluminum disk which was then glued on the sample holder at the beamlines, making it easier to retrieve the sample after the experiment is done.

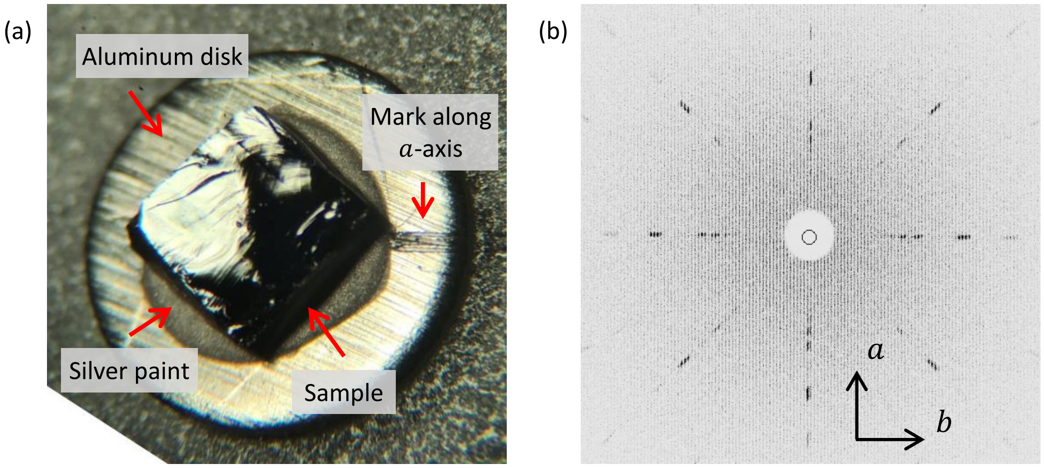

Figure 2.7: (a) Optical microscope picture of $La_{1.905}Ba_{0.095}CuO_4$ sample with a cleaved surface mounted on an aluminum disk with silver paint. The cleaved surface shows a mirror-like reflection of light (bright region on the surface). The scratch on the disk indicates the a-axis direction. The diameter of the aluminum disk is 5 mm. (b) Laue diffraction pattern of $La_{1.905}Ba_{0.095}CuO_4$ sample in the back-scattering geometry where c-axis is parallel to the beam direction.

When the sample is brought to a beamline, the alignment of the sample is accomplished by locating two structural Bragg reflection. In soft x-ray range, because the size of Ewald sphere is small, only few Bragg reflections are reachable. For aligning LBCO and LESCO samples, $(0, 0, 2)$ and $(1, 0, 1)$ reflections were located using 1750 eV x-rays. Often, it is very challenging to locate the two reflections in the vast angle space, and pre-alignment before the actual experiment using a hard x-ray source can save a lot of time. The pre-alignment was performed using the Panalytical X'Pert XRD (Cu K_α source) instrument located at MRL, University of Illinois, by identifying the direction of a-axis and making a mark along that direction on the aluminum disk on which the sample is glued [Fig. 2.7(a)].

2.3.3 O K and Cu L_3 edge

For RSXS experiment, the incident beam energy needs to be tuned at an absorption edge at which an electronic transition to a valence state occurs. Absorption edge energies can be found by measuring an x-ray absorption spectrum and identifying the peaks in the spectrum. In cuprates, the resonant scattering of CDW has been observed at two absorption edges, O K ($1s \rightarrow 2p$) edge and Cu L_3 ($2p \rightarrow 3d$) edge [25,26,44]. To be more specific, the O K resonance occurs at the lower energy pre-edge peak (Zhang-Rice singlet state [45–47]) below the onset of the main O K edge, that is sensitive to the ordering of holes, and the Cu L_3 resonance occurs at the main peak, being sensitive to the distortions of the Cu sublattice [25].

X-ray absorption spectroscopy (XAS) measurements are commonly performed by measuring either the

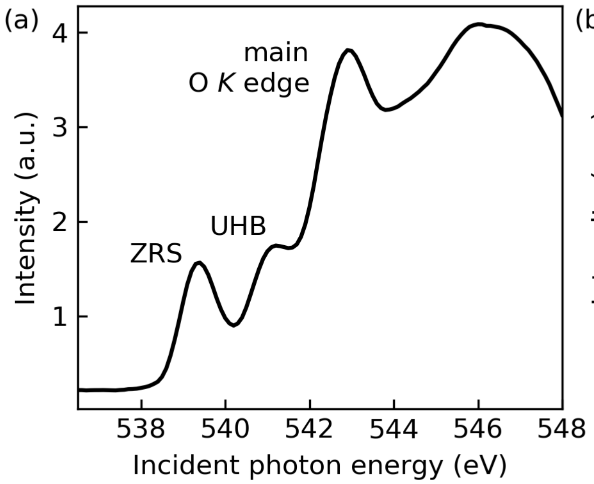

Figure 2.8: XAS spectrum of a LESCO x=0.15 sample at (a) O K and (b) Cu L_3 edge measured in TFY mode using a CCD detector at SSRL beamline 13-3. The O K spectrum exhibit two pre-edge peaks below the main absorption edge: the lower energy peak is often identified as the Zhang-Rice singlet state (ZRS) and the higher energy peak as the upper Hubbard band (UHB).

energy-integrated fluorescence intensity (total fluorescence yield, TFY) or the current through the sample (total electron yield, TEY) while scanning the incident beam energy. Because electrons are much easily absorbed by materials compared to x-rays, TEY method is more surface-sensitive, whereas TFY method is often regarded as a bulk probe. Figure 2.8 shows XAS spectrum of a LESCO $x = 0.1$ sample at O K and Cu L_3 edge measured in TFY mode.

2.3.4 Fluorescence background

One of the obstacles to detecting weak correlations using RSXS is that the RSXS intensities are always accompanied by unwanted fluorescence backgrounds. Fluorescence is incoherent, inelastic scattering and does not carry information of spatial modulation of electron density. The elastic scattering from CDW can be as small as 1 % of the fluorescence background [26, 48], and conventional energy-integrating detectors cannot discriminate the elastic signal from the background. When the CDW is well-ordered, which is often the case in under-doped cuprates, the elastic scattering feature in a RSXS scan is sharp enough to be discerned above the slowly-varying background. However, CDWs in optimally-doped cuprates are often "glassy" with short correlation lengths. The scattering from such orders is not only weak but also distributed over a wide range in momentum space, and is no longer easily discernable from the fluorescence background.

To overcome this problem, the RSXS studies presented in this thesis employed two methods of fluorescence background rejection. The first method is using an energy-resolving detector to discriminate elastic scattering signals from fluorescence backgrounds, and the details are presented in chapter 5. In this section, the second

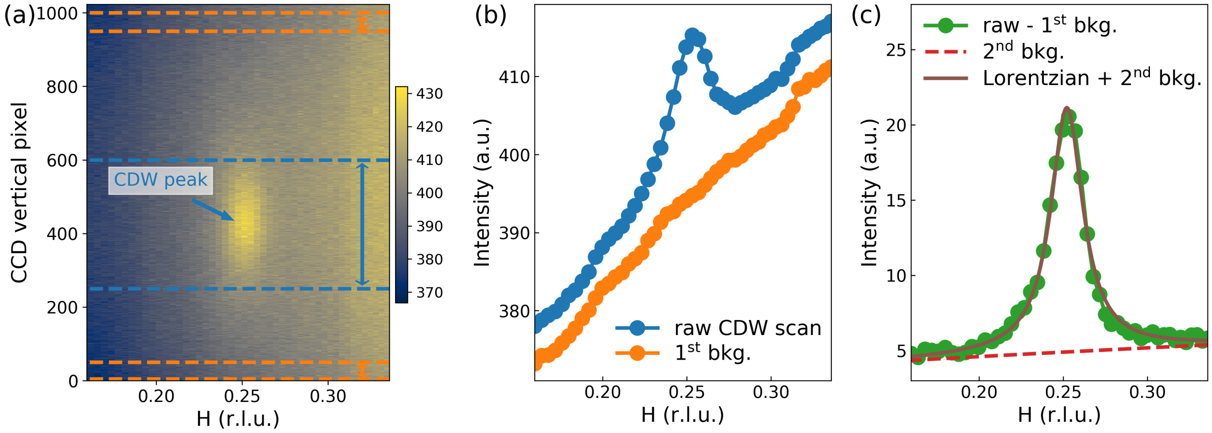

Figure 2.9: (a) Intensity map of H-scan of CDW of LESCO x=0.15 at T = 23 K measured using a CCD detector at SSRL beamline 13-3. The region within the blue (orange) dashed lines captures CDW (fluorescence) signals. (b) Raw CDW H-scan and the first background curve obtained from the blue and orange region, respectively, in (a). (c) The result of the first background subtraction (green curve) that is fitted with the second background modeled with a quadratic function (red dashed line) and a Lorentzian function (brown curve).

method is introduced that is using a two-dimensional (energy-integrating) CCD detector to measure the angular distribution of fluorescence accurately and subtract the background profile from the data.

Figure 2.9 shows the example of the background subtraction from the RSXS scan of CDW in LESCO x=0.15 using a CCD detector. As shown in Fig. 2.9(a), the center part of the CCD images (the region within blue dashed lines) captures the CDW peak profile, while the top and bottom parts (the regions with in orange dashed lines) are far away from the CDW peak and essentially capturing the H dependence of fluorescence intensity. Figure 2.9(b) shows the raw H-scan of CDW (blue curve) and the fluorescence background (orange curve) obtained by averaging intensities within each region of the images, and the first background subtraction is carried out by subtracting the two curves. In Fig. 2.9(c), the result of the first background subtraction (green curve) is plotted, which shows a residual background due to the vertical variation of fluorescence in the CCD images. The remaining background is modeled with a quadratic function (red dashed line) and used for the second background subtraction. The final result after the first and second background subtraction is modeled with a Lorentzian function (brown curve) to obtain the profile of CDW peak.

Chapter 3

Discovery of charge density wave in $BaNi_2As_2$ and Co-, Sr-doped systems

This chapter has been adapted from Ref. [43] and [49].

3.1 Introduction: superconductivity and ordering phenomena in pnictides

The discovery of Fe-based superconductivity in 2008 [6] uncovered an entirely new and fascinating class of unconventional superconducting materials with transition temperatures rivaling those of the high-T_c cuprates [7]. A central but poorly understood feature of these materials concerns the importance of the magnetic Fe cation: Exchange of another transition metal for Fe either quenches superconductivity altogether or strongly suppresses it [50]. For example, the prototypical Fe-based superconductor, $Ba(Fe_{1-x}Co_x)_2As_2$, exhibits a maximum superconducting transition temperature, $T_c = 24$ K when $x = 0.07$ [7,19,51]. However, its Ni homologue, $Ba(Ni_{1-x}Co_x)_2As_2$, exhibits a maximum T_c of only 2.3 K [17,50,52]. Understanding why the superconductivity is suppressed in Ni-pnictide compound is interesting in its own right and could shed light on the mechanism of superconductivity in pnictide superconducting materials.

One common observation found in the phase diagram of high-temperature superconductors is that superconductivity (SC) resides in the vicinity of some other ordered phases, such as CDW, antiferromagnetic (AF) phase, spin density wave (SDW), and nematic phase [7,12,53]. The relationship between these phases has been found to be very intimate, more complex than a simple competition, yet its nature has not been fully understood. For example, in cuprates, CDW is ubiquitously found just above the SC phase boundary [12,54]. While it is believed that static CDW competes with SC [15,16,32], there is a growing number of evidence indicating that fluctuating CDW may be favorable for SC [55,56].

In the case of iron-pnictide superconductors, magnetism has been believed to play a central role on the formation of SC [53], as shown in the fact that the SC phase emerges near the critical point where the AF phase is destroyed [19,57,58]. However, with the recent discoveries of electronic nematic phase in pnictide compounds [13,59,60], charge instability in pnictide superconductors has brought a lot of attention, and it

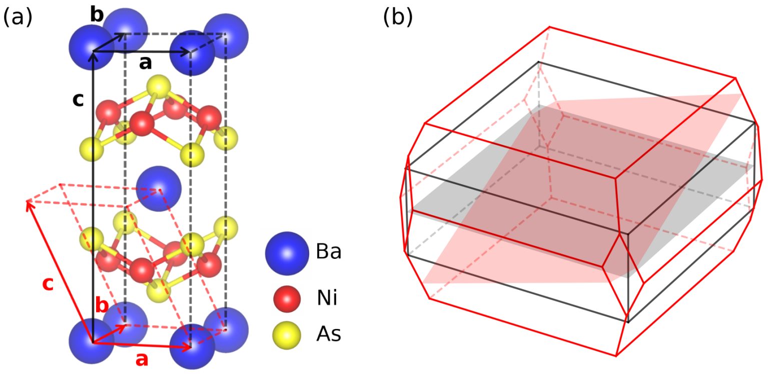

Figure 3.1: (a) The crystal structure and the unit cell of tetragonal (black dashed lines) and triclinic phase (red dashed lines). The arrows represent the crystal axes of each structure. (b) The Brillouin zone boundary of tetragonal (black lines) and triclinic phase (red lines). The planes colored in black and red represent H-K planes of tetragonal and triclinic phase, respectively.

is an interesting question whether there is a charge-ordered phase in pnictides that is comparable to CDW in cuprates, and what their influence on SC is.

3.2 Results

Single crystals of $Ba(Ni_{1-x}Co_x)_2As_2$ (x = 0, 0.071, 0.082, 0.118) and $Ba_{1-x}Sr_xNi_2As_2$ (x = 0.27, 0.42, 0.47, 0.65, 0.73) were studied using the in-lab hard x-ray diffraction instrument at University of Illinois. The crystals were grown using the flux method [13,17] by Chris Eckberg, a former graduate student at the Paglione group at the University of Maryland. First presented are the data on the structural properties and CDW phases of the undoped compound $BaNi_2As_2$. The data on the evolution of the properties upon Co- and Sr-doping are presented in the following sections. In addition, some preliminary results on the nematic response of CDW in $Ba_{1-x}Sr_xNi_2As_2$ under a uniaxial strain are introduced in the last section.

3.2.1 Tetragonal-to-triclinic structural phase transition in $BaNi_2As_2$

The structure of $BaNi_2As_2$ has a tetragonal $I4/mmm$ symmetry at room temperature and it undergoes a phase transition to a triclinic $P\bar{1}$ symmetry at the transition temperature $T_s = 136$ K [18,43]. Figure 3.1(a) and (b) shows the unit cells and the Brillouin zone boundaries of each phase. Note that the H-K planes of the tetragonal and triclinic phases are not parallel to each other, but about 20° rotated. Throughout this letter, we use $(H, K, L)_{\mathrm{tet}}$ and $(H, K, L)_{\mathrm{tri}}$ to denote momentum space locations indexed with the tetragonal and triclinic unit cells, respectively.

Figure 3.2 describes the tetragonal-to-triclinic structural transition in $BaNi_2As_2$. The $(0, 0, 14)_{\mathrm{tet}}$ in-

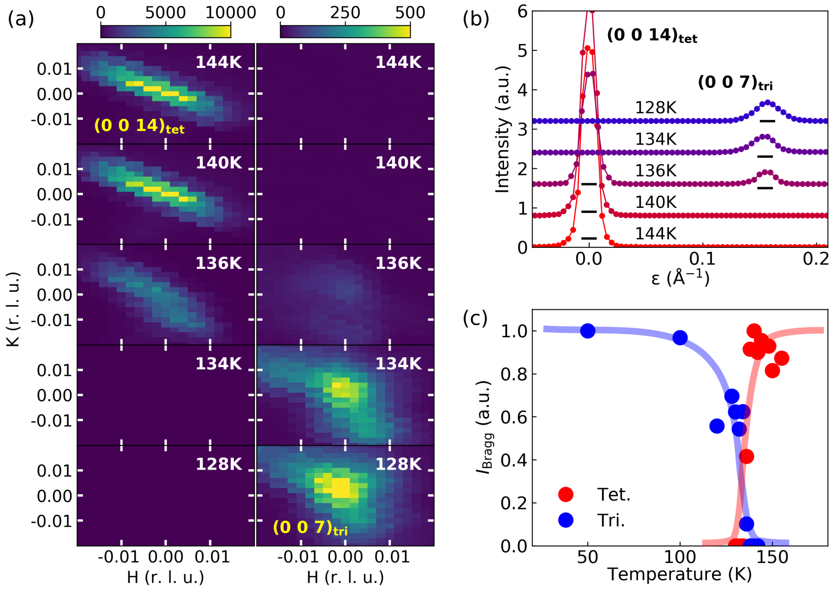

Figure 3.2: Tetragonal-to-triclinic structural phase transition in $BaNi_2As_2$. (a) (H, K) maps of the tetragonal $(0, 0, 14)_{\mathrm{tet}}$ and triclinic $(0, 0, 7)_{\mathrm{tri}}$ reflections from a $BaNi_2As_2$ $(x = 0)$ crystal for a selection of temperatures, showing the change in symmetry at T_{tri}. (b) Line scans through $(0, 0, 14)_{\mathrm{tet}}$ and $(0, 0, 7)_{\mathrm{tri}}$ reflections. ε is the distance in momentum space from $(0, 0, 14)_{\mathrm{tet}}$ along the direction to $(0, 0, 7)_{\mathrm{tri}}$. Horizontal bars represent the instrumental momentum resolution at the specific scattering geometry. (c) Temperature dependence of integrated intensities of the tetragonal and triclinic reflections. All curves are scaled to the maximum observed intensity.

tensity decreases at $T_{\mathrm{tri}} = 136 \pm 1$ K and the $(0, 0, 7)_{\mathrm{tri}}$ appears. After a narrow range of coexistence, $(0, 0, 14)_{\mathrm{tet}}$ peak vanishes and the $(0, 0, 7)_{\mathrm{tri}}$ grows rapidly. This observation validates previous claims that this transition is weakly first order [18].

3.2.2 Charge density wave in $BaNi_2As_2$

The discovery of CDWs in $BaNi_2As_2$ is summarized in Fig. 3.3. While still in the tetragonal phase, as the temperature is lowered toward T_{tri}, a weak reflection with propagation vector $(0.28, 0, 0)_{\mathrm{tet}}$ grows in intensity as the transition is approached. This reflection is visible in multiple Brillouin zones [Fig. 3.3(a)], identifying it as a coherent superstructure and not an errant reflection from another grain. This reflection is incommensurate, meaning its wave vector does not index to a simple rational fraction. Because this reflection occurs only below 150 K, and is not a property of the room temperature structure, it is identified as a CDW.

Below T_{tri} the $(0.28, 0, 0)_{\mathrm{tet}}$ reflection vanishes and is replaced by a much stronger CDW with incommensurate wave vector $(0.31, 0, 0)_{\mathrm{tri}}$ [Fig. 3.3(b), (c)]. Evidently the triclinic transition is associated with the formation of this CDW. Note that, despite the similar Miller indices, the vectors $(0.28, 0, 0)_{\mathrm{tet}}$ and $(0.31, 0, 0)_{\mathrm{tri}}$ are nearly 20° apart and reside in very different regions of momentum space [Fig. 3.1(b), 3.3(c)]. The wave

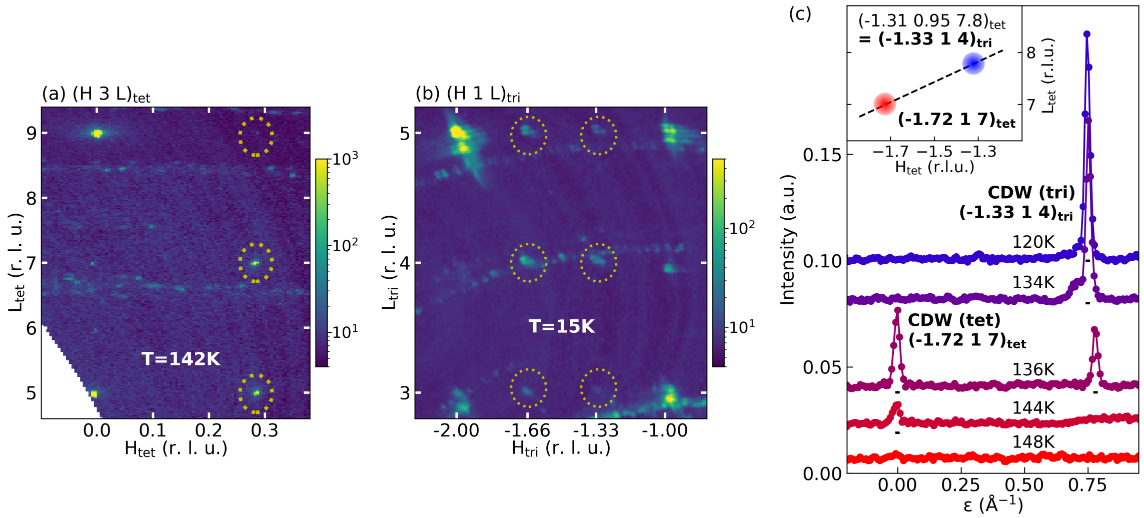

Figure 3.3: CDW phases in $BaNi_2As_2$. (a) Wide (H, L) map of reciprocal space in the tetragonal phase showing the $(0.28, 0, 0)_{\mathrm{tet}}$ CDW reflections in multiple Brillouin zones (dashed circles), establishing it as a coherent diffraction effect. (b) Similar map in the triclinic phase showing $(0.33, 0, 0)_{\mathrm{tri}}$ CDW reflections. (c) Line momentum scans through the $(-1.72, 1, 7)_{\mathrm{tet}}$ and $(-1.33, 1, 4)_{\mathrm{tri}}$ reflections showing the evolution of the CDW phases with temperature. ε is the distance from $(-1.72, 1, 7)_{\mathrm{tet}}$ along the direction to $(-1.33, 1, 4)_{\mathrm{tet}}$. Horizontal scale bars indicate the momentum resolution. (Inset) Schematic of the momentum scan displayed in panel (c).

vector of the CDW shifts as the temperature is lowered and pins to the commensurate value $(1/3, 0, 0)_{\mathrm{tri}}$ at a lock-in transition $T_L = 129$ K [Fig. 3.6(a), (d)]. Lock-in effects are an established consequence of lattice pinning in other CDW materials, suggesting pinning plays an important role in stabilization of this CDW phase [61–65].

The amplitude of the CDW distortion is of the same order of magnitude as that in Peierls materials. An estimate of its magnitude can be obtained by comparing the intensities of a few CDW satellites with their associated primary Bragg reflections. A single pair of reflections cannot, of course, provide a complete 3D mapping of the CDW structure, which would require a Rietveld refinement incorporating thousands of reflections. However, it is possible to obtain a *crude estimate* of the amplitude by making some simplifying assumptions.

The distortion model of the period-3a CDW in the triclinic phase is depicted in Fig. 3.4(a). The estimation from this model is made by assuming that all atoms in the unit cell move the same distance, i.e., the second unit cell is displaced by Δ in a direction, and the atoms in the third unit cell in the opposite direction. Even though it does not give information of particular direction and amplitude of the displacement of each atom in a unit cell, this estimation provides an overall distortion amplitude of a unit cell averaged over atoms reflected on its structure factor.

Δ can be obtained by comparing the integrated intensity of the structure Bragg peak at $\boldsymbol{Q}_{\mathrm{Bragg}}$ and

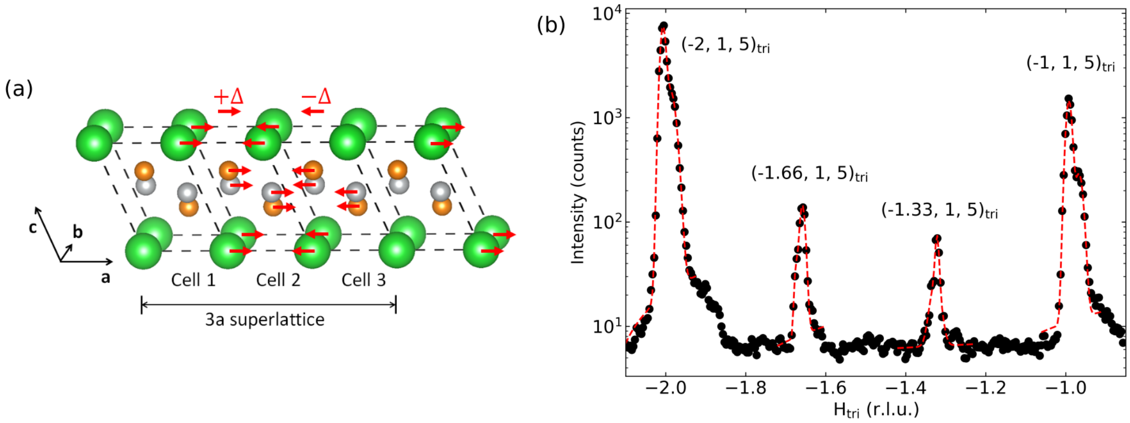

Figure 3.4: (a) Simplified distortion model of $(1/3,0,0)_{\text{tri}}$ CDW phase. (b) H-scan on $(-2,1,5)_{\text{tri}}$, $(-1,1,5)_{\text{tri}}$ structure Bragg peaks and satellite CDW peaks from a BaNi_2As_2 sample at T = 15 K. Each peak shows a secondary peak due to twinning and fitted with two Gaussian functions (red dashed curves). Integrated intensity of each peak is obtained from the Gaussian fit of the main peak.

CDW peak at $\boldsymbol{Q}_{\text{CDW}} = \boldsymbol{Q}_{\text{Bragg}} + (1/3,0,0)_{\text{tri}}$. The structure factor of the 3a superlattice cell is given by

$$\begin{aligned} S(\boldsymbol{Q}) &= \sum_n f_n e^{-i\boldsymbol{Q}\cdot\boldsymbol{r}_n} + \sum_n f_n e^{-i\boldsymbol{Q}\cdot\left\{\boldsymbol{r}_n+\left(1+\frac{\Delta}{a}\boldsymbol{a}\right)\right\}} + \sum_n f_n e^{-i\boldsymbol{Q}\cdot\left\{\boldsymbol{r}_n+\left(2-\frac{\Delta}{a}\boldsymbol{a}\right)\right\}} \\ &= \sum_n f_n e^{-i\boldsymbol{Q}\cdot\boldsymbol{r}_n}\left[1+e^{-i\boldsymbol{Q}\cdot\boldsymbol{a}}e^{-i\frac{\Delta}{a}\boldsymbol{Q}\cdot\boldsymbol{a}}+e^{-2i\boldsymbol{Q}\cdot\boldsymbol{a}}e^{i\frac{\Delta}{a}\boldsymbol{Q}\cdot\boldsymbol{a}}\right] \\ &= \sum_n f_n e^{-i\boldsymbol{Q}\cdot\boldsymbol{r}_n}\left[1+e^{-i\boldsymbol{Q}\cdot\boldsymbol{a}}+e^{-2i\boldsymbol{Q}\cdot\boldsymbol{a}}-i\frac{\Delta}{a}\boldsymbol{Q}\cdot\boldsymbol{a}e^{-i\boldsymbol{Q}\cdot\boldsymbol{a}}+i\frac{\Delta}{a}\boldsymbol{Q}\cdot\boldsymbol{a}e^{-2i\boldsymbol{Q}\cdot\boldsymbol{a}}\right], \end{aligned}$$

where f_n is the form factor of the nth atom, $\boldsymbol{r}_n$ is the coordinate of the nth atom in the first unit cell and $\boldsymbol{a}$ is the real space lattice vector along a-axis. In the last step, we have assumed $\Delta \ll a$. The intensity ratio of a structural Bragg peak and a CDW satellite is then given by

$$\frac{I_{\text{CDW}}}{I_{\text{Bragg}}} = \frac{|S(\boldsymbol{Q}_{\text{CDW}})|^2}{|S(\boldsymbol{Q}_{\text{Bragg}})|^2} = \frac{(\boldsymbol{Q}_{\text{CDW}}\cdot\boldsymbol{a})^2}{3}\left|\frac{\sum_n f_n e^{-i\boldsymbol{Q}_{\text{CDW}}\cdot\boldsymbol{r}_n}}{\sum_n f_n e^{-i\boldsymbol{Q}_{\text{Bragg}}\cdot\boldsymbol{r}_n}}\right|^2\left(\frac{\Delta}{a}\right)^2.$$

Figure 3.4(b) shows an H-scan through the $(-2,1,5)_{\text{tri}}$ and $(-1,1,5)_{\text{tri}}$ structural Bragg peaks, as well as the two CDW satellite peaks between them, for the BaNi_2As_2 ($x = 0$) sample at T = 15 K. The integrated intensity of each peak is obtained from Gaussian fitting and taking the area under the fitted curve. The intensity ratio of the $\boldsymbol{Q}_{CDW} = (-1.33,1,5)_{\text{tri}}$ and $\boldsymbol{Q}_{Bragg} = (-1,1,5)_{\text{tri}}$ reflections is found to be 0.034, and the ratio of $\boldsymbol{Q}_{CDW} = (-1.66,1,5)_{\text{tri}}$ to $\boldsymbol{Q}_{Bragg} = (-2,1,5)_{\text{tri}}$ is found to be 0.02. These ratios give the estimation of $\Delta \sim 0.154\mathring{A}$ and $0.133\mathring{A}$, respectively. This distortion is of the same order as in Peierls materials TaS_2 and TaSe_2, which are 0.23 Å and 0.052 Å, respectively [62]. This is only an order-of-magnitude estimate, and should not be considered as a quantitative determination of the size of the lattice

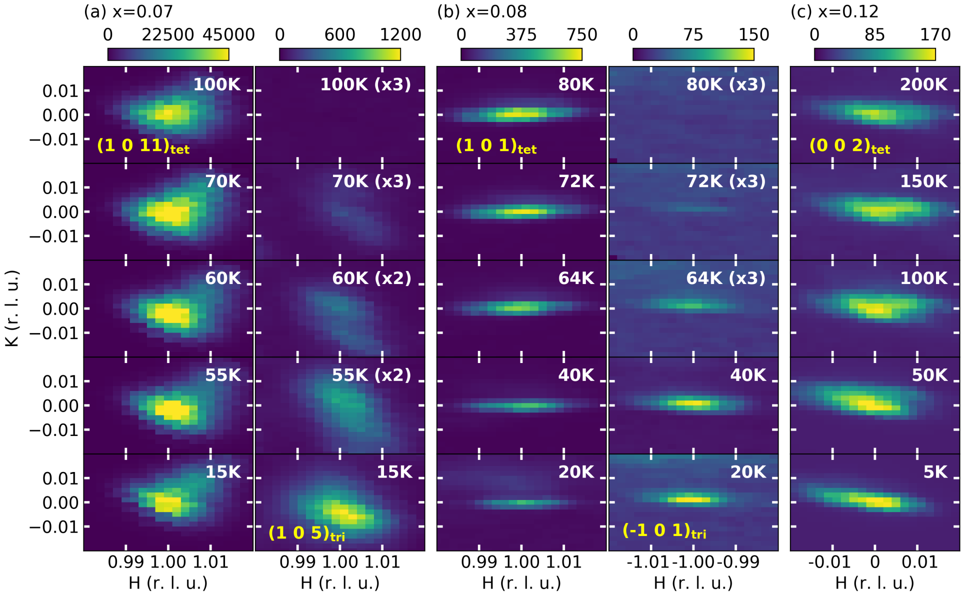

Figure 3.5: Evolution of the tetragonal-to-triclinic structural phase transition upon Co-doping in $Ba(Ni_{1-x}Co_x)_2As_2$. (a) (H, K) maps of $(1, 0, 11)_{\mathrm{tet}}$ and $(1, 0, 5)_{\mathrm{tri}}$ reflections from a Co-doped crystal with $x = 0.07$, showing the suppression of T_{tri} and phase coexistence. (b) Same measurement for the $(1, 0, 1)_{\mathrm{tet}}$ and $(-1, 0, 1)_{\mathrm{tri}}$ reflections from a crystal with $x = 0.08$. (c) Same measurement for the $(0, 0, 2)_{\mathrm{tet}}$ reflection of a crystal with $x = 0.12$, which remains purely tetragonal down to 5 K.

distortion. However, it suggests the CDW in $BaNi_2As_2$ is likely driven at least in part by the electron-lattice interaction.

3.2.3 Effect of Co doping

In Co-doped samples $Ba(Ni_{1-x}Co_x)_2As_2$, the triclinic phase is suppressed to $T_{\mathrm{tri}} = 75 \pm 5$ K at $x = 0.07$ and $T_{\mathrm{tri}} = 74 \pm 2$ K at $x = 0.08$ [Fig. 3.5(a), (b)], respectively. The tetragonal phase does not vanish below T_{tri} at these compositions, however, but persists down to our base temperature of 5 K. Also, the development of the intensity of the triclinic Bragg reflection is more gradual in these crystals than in the $x = 0$ case. These observations suggest that Co doping suppresses and broadens the triclinic transition and leads to an extended region of coexistence between tetragonal and triclinic phases. No structural phase transition was observed in the $x = 0.12$ crystal [Fig. 3.5(c)], which remained tetragonal down to 5 K.

The CDW in the tetragonal phase is no longer observed in Co-doped samples. However, at $x = 0.07$ and $x = 0.08$ an incommensurate CDW still appears at the (reduced) triclinic transition (Fig. 3.6(b)-(c)). Both materials still exhibit lock-in transitions, at $T_L = 47.5$ K for $x = 0.07$ and $T_L = 25$ K for $x = 0.08$ (Fig. 3.6(e)-(f)). The commensurate CDW in both crystals has the same wave vector as the $x = 0$ compound. However, strangely, the CDW in the $x = 0.07$ sample is oriented in the K direction, with wave vector

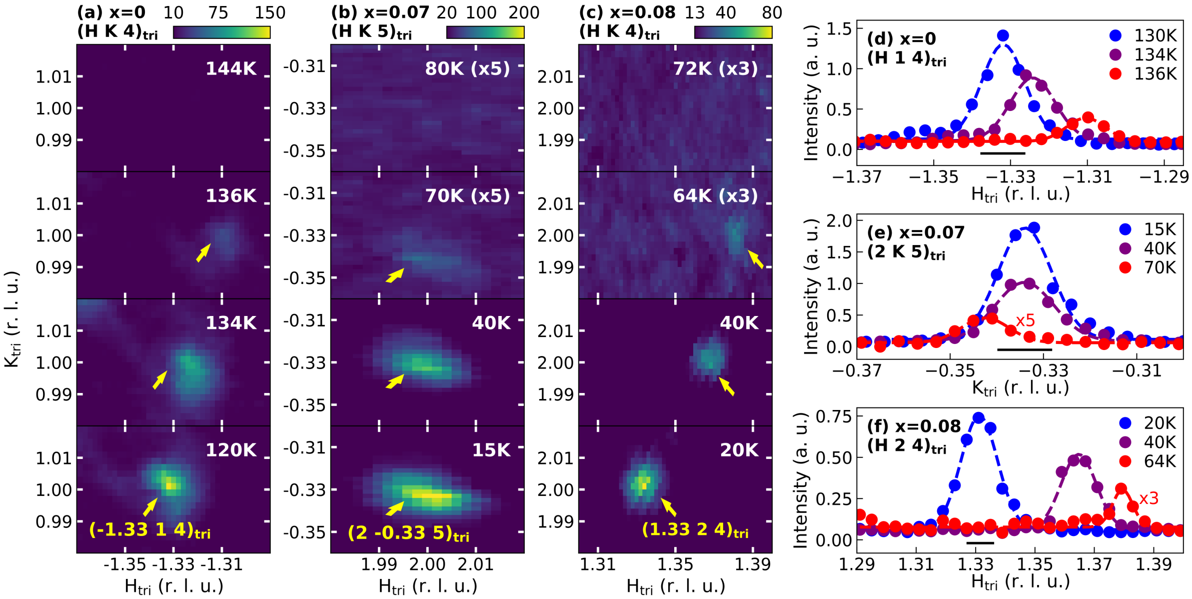

Figure 3.6: CDW in the triclinic phase of $\mathrm{Ba(Ni_{1-x}Co_x)_2As_2}$ and lock-in transition. (a), (b), (c) Narrow (H, K) maps of reciprocal space of the CDW in the triclinic phase of $x = 0, 0.07, 0.08$ crystals, respectively, for a selection of temperatures. (d), (e), (f) Line momentum scans on the CDW reflections of $x = 0, 0.07, 0.08$ crystals along modulation direction (H for $x = 0, 0.08$ and K for $x = 0.07$) showing lock-in behavior. The horizontal scale bars in panels (d)-(f) indicate the momentum resolution.

$(0, 1/3, 0)_{\mathrm{tri}}$, while in $x = 0$ and 0.08 it is along H. We conclude that, although H and K directions are not equivalent in the triclinic phase, the anisotropy is too small to pin the direction of the CDW modulation, which is nevertheless unidirectional in all samples. No CDW was observed in the $x = 0.12$ sample, which also exhibits no triclinic transition.

The overall picture that emerges is as follows (see the phase diagram in Fig. 3.7). The $x = 0$ compound develops weak, precursor CDW fluctuations with wave vector $(0.28, 0, 0)_{\mathrm{tet}}$ in tetragonal phase upon cooling. These fluctuations are preempted at $T_{\mathrm{tri}} = 136$ K by the first order, tetragonal-to-triclinic transition and the appearance of a strong, primary CDW with wave vector $(0.31, 0, 0)_{\mathrm{tri}}$. Upon further cooling the CDW shifts and pins to the commensurate value $(1/3, 0, 0)_{\mathrm{tri}}$ at $T_L = 129$ K. Magnetic measurements show a drop in the susceptibility at T_{tri} [43], suggesting the spin configuration changes when the CDW forms, though neutron measurements have not detected antiferromagnetic order [20].

3.2.4 Effect of Sr doping

The tetragonal-to-triclinic structural phase transition is observed in the Sr-doped compound as well. Figure 3.8 summarizes the structural transition at $x = 0.42$. When cooled across the phase transition, the $(0, 1, 9)_{\mathrm{tet}}$ structural Bragg reflection in the tetragonal phase splits into four reflections due to the formation of twin

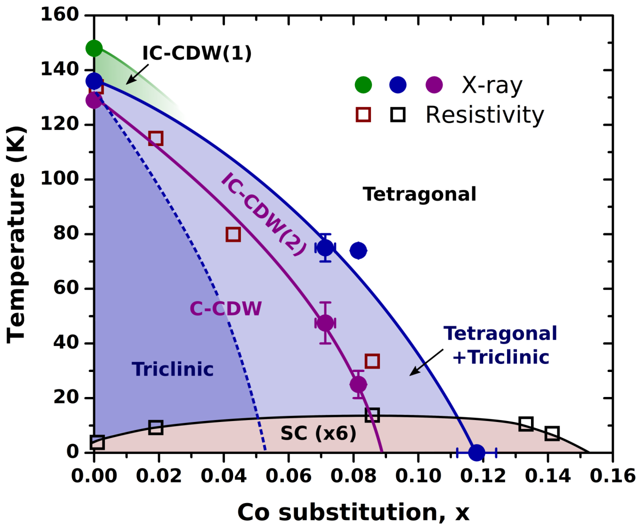

Figure 3.7: Phase diagram of $Ba(Ni_{1-x}Co_x)_2As_2$. (green) Incommensurate CDW in the tetragonal phase. (dark purple) Triclinic phase exhibiting a commensurate CDW. (light purple) Heterogeneous region exhibiting coexisting tetragonal and triclinic phases as well as either an incommensurate CDW (IC-CDW) or a commensurate CDW (C-CDW). (beige) Superconducting phase, whose maximum T_c arises in a region of heterogeneous coexistence (data points taken from Ref. [17]).

domains in triclinic phase [Fig. 3.8(a)]. One domain is chosen among the four, and the reflection from the domain is indexed to be $(-1, 0, 5)_{\mathrm{tri}}$. The line scans through $(0, 1, 9)_{\mathrm{tet}}$ and $(-1, 0, 5)_{\mathrm{tri}}$ show a sharp transition in their integrated intensity at $T_s = 112.5 \pm 2.5$ K, indicating the change in symmetry of crystal structure [Figs. 3.8(b), (c)].

The evolution of the structural transition over the full range of Sr doping x is summarized in Fig. 3.11. At $x = 0.27$, the transition temperature T_s is slightly higher than that of $x = 0$, and it decreases upon further doping up to $x = 0.65$. At $x = 0.73$, no structure change is observed and the sample remains tetragonal down to 8 K, being consistent with the previous report of the abrupt disappearance of the triclinic phase above the critical doping $x_c = 0.7$ [13]. Note that, as expected from its first-order nature, the structural transition exhibits a hysteresis on temperature (Fig. 3.11). As opposed to the Co-doped compounds, $Ba(Ni_{1-x}Co_x)_2As_2$, which exhibit an extended region of coexistence between tetragonal and triclinic phase in their phase diagram, the structural transition in $Ba_{1-x}Sr_xNi_2As_2$ occurs in a very narrow temperature range and no significant coexistence region is observed.

$Ba_{1-x}Sr_xNi_2As_2$ exhibit an interesting CDW instability, which leads to three distinct CDW phases. Especially at $x = 0.42$, the three CDW transitions take place sequentially upon cooling the sample, showing a competition between different CDWs. The first CDW phase that appears upon cooling is the incommensurate CDW (IC-CDW) that starts to form at $T_{\mathrm{IC}} = 132.5 \pm 2.5$ K, about 20 K above the tetragonal-triclinic phase

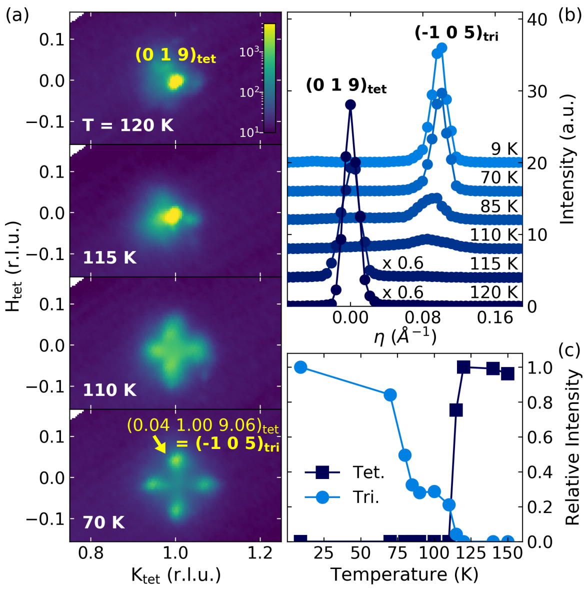

Figure 3.8: Tetragonal-to-triclinic structural phase transition in $Ba_{0.58}Sr_{0.42}Ni_2As_2$. (a) H-K maps at a selection of temperatures showing the evolution of $(0,1,9)_{\mathrm{tet}}$ structural Bragg reflection across the phase transition. The splitting of the reflection below $T = T_{\mathrm{s}}$ is due to the formation of twin domains in triclinic phase. (b) Line momentum scans through tetragonal $(0,1,9)_{\mathrm{tet}}$ and triclinic $(-1,0,5)_{\mathrm{tri}}$ Bragg reflections. η is the distance in momentum space from $(0,1,9)_{\mathrm{tet}}$ along the direction to $(-1,0,5)_{\mathrm{tri}}$. (c) Integrated intensities of the tetragonal (Tet.) and triclinic (Tri.) Bragg reflections, showing the change in symmetry of crystal structure.

boundary [Figs. 3.9(a), (d)]. The wave vector of the IC-CDW is $(0, 0.28, 0)_{\mathrm{tet}}$ and it is consistent with the IC-CDW phase that was previously observed in the parent compound $BaNi_2As_2$ [43].

As the sample is further cooled, the second CDW transition occurs at T_{C1}, which coincides with T_s, where the IC-CDW is replaced by a commensurate CDW (C-CDW-1) phase with the wave vector of $(0, 1/3, 0)_{\mathrm{tri}}$ [Figs. 3.9(b), (e)]. While a lock-in effect is observed in the parent and Co-doped compounds [43], no significant shift of the wave vector is observed in Sr-doped compounds. The third CDW transition occurs at $T_{C2} = 95 \pm 5$ K, where another commensurate CDW (C-CDW-2) phase arises with the wave vector of $(0, 1/2, 0)_{\mathrm{tri}}$, and the intensity of C-CDW-2 reflections develops down to the base temperature [Figs. 3.9(c), (f)]. The intensity of C-CDW-1 reflections drastically drops at T_{C2} and a very weak signal coexist with C-CDW-2.

Figure 3.10 shows the temperature dependence of the integrated intensities of the CDW reflections that summarizes the evolution of the CDWs upon Sr doping. The IC-CDW phase is present from $x = 0$ to 0.47 within 20 K above the tetragonal-triclinic phase boundary. Unlike Co doping which suppresses the IC-CDW very quickly, the IC-CDW in Sr-doped compounds persists up to relatively higher doping. While it is absent in the lower Sr-doping, the C-CDW-2 phase first appears at $x = 0.42$ and replaces C-CDW-1 from the low

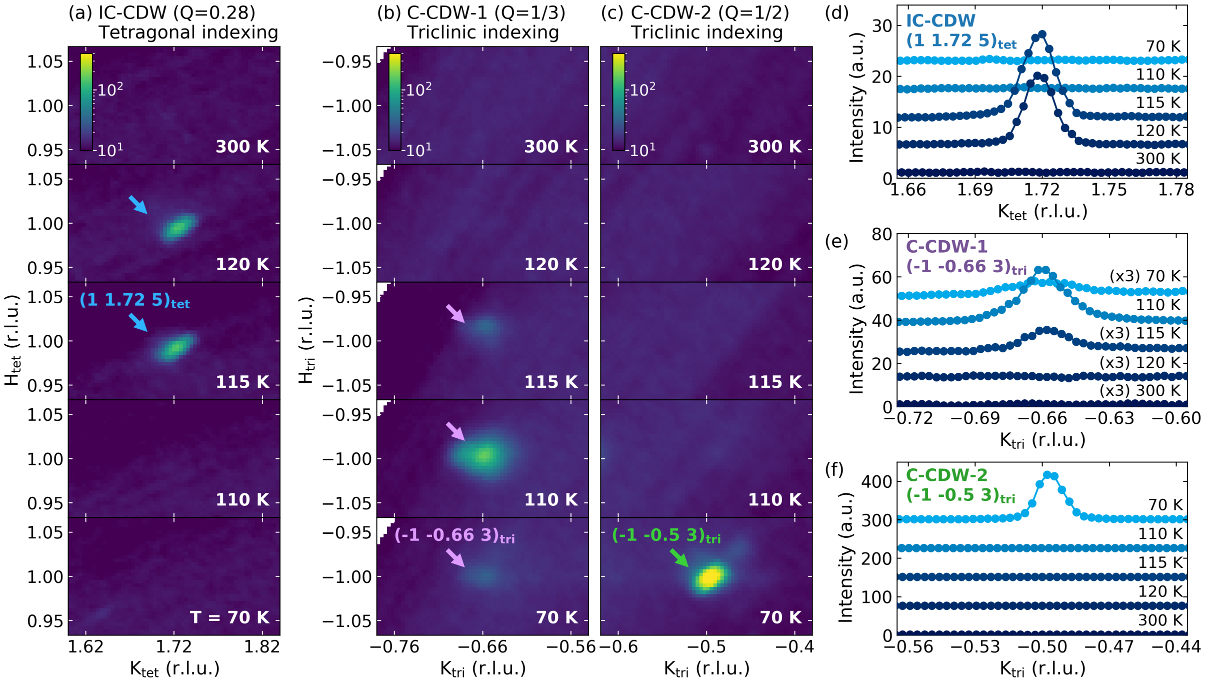

Figure 3.9: Three distinct CDWs in $Ba_{0.58}Sr_{0.42}Ni_2As_2$. (a), (b), (c) H-K maps of IC-CDW, C-CDW-1, and C-CDW-2, respectively, at a selection of temperatures. (d), (e), (f) Line momentum scans of the CDW reflections shown in (a), (b), and (c), respectively, along the modulation direction. The panels (a) and (d) are indexed in the tetragonal coordinates, and (b), (c), (e), and (f) are in the triclinic coordinates.

temperature ground state up to $x = 0.65$. This evolution tendency shows a clear competition between the three CDWs in a sense that two different CDWs never have their intensity maximized at the same time. At $x = 0.73$, no CDW transition is observed. The overall phase diagram of $Ba_{1-x}Sr_xNi_2As_2$ is presented in Fig. 3.11.

Recently, an elastoresistivity study discovered that $BaNi_2As_2$ exhibits a divergent nematic susceptibility, and the nematic order parameter linearly scales with the amplitude of IC-CDW [13], which suggests there is some connection between this CDW and the existence of nematic order. Upon Sr doping, $Ba_{1-x}Sr_xNi_2As_2$ shows an enhancement of nematic fluctuations, until the doping reaches the critical point $x_c = 0.7$ where the structural transition is abruptly suppressed to 0 K. As shown in Fig. 3.11, the IC-CDW phase directly overlaps on the region where the nematic susceptibility exhibits a strong divergent behavior. This observation further supports the possible connection between the IC-CDW and the nematic order.

3.2.5 Nematic response of charge density wave in $Ba_{0.73}Sr_{0.27}Ni_2As_2$

To investigate the possible nematic property of the IC-CDW in the tetragonal phase, its response to a uniaxial strain is measured using a piezoelectric actuator cell. Figure 3.12(a) shows a schematic drawing

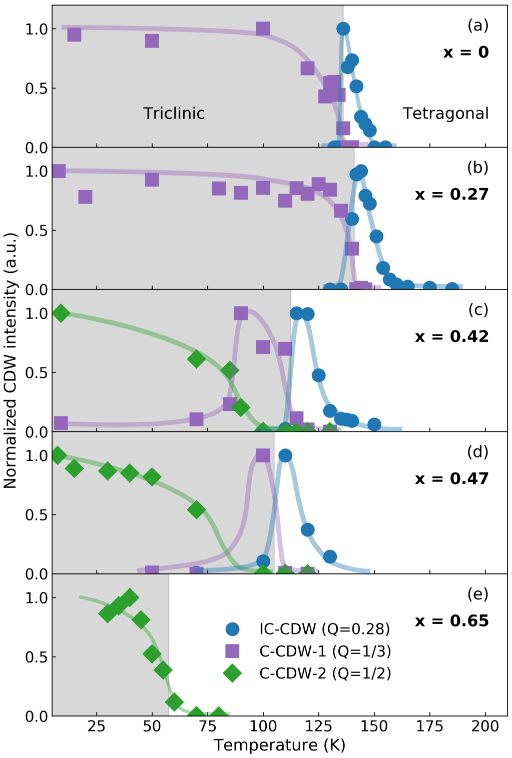

Figure 3.10: Temperature dependence of the integrated intensities of the IC-CDW (blue circles), C-CDW-1 (purple squares), and C-CDW-2 (green diamonds) reflections in $Ba_{1-x}Sr_xNi_2As_2$. The Sr doping, x, is shown in each panel. The shaded region with gray color represents the temperature range of the triclinic phase. Each curve is scaled from 0 to 1 and the solid lines are guides to the eye.

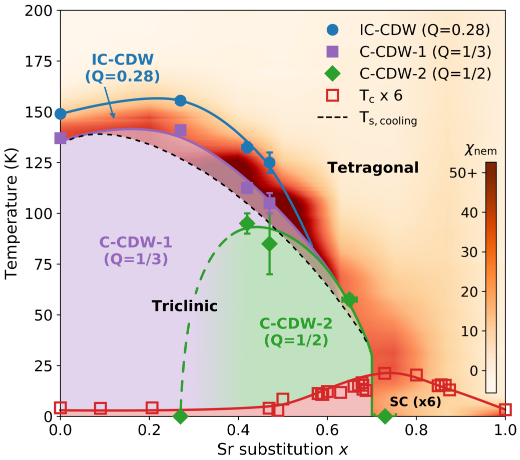

Figure 3.11: Phase diagram of $Ba_{1-x}Sr_xNi_2As_2$ showing the IC-CDW (blue circles), C-CDW-1 (purple squares), C-CDW-2 (green diamonds) phase boundaries. The color scale overlaid in the tetragonal phase region represents the nematic susceptibility, χ_{nem}. The triclinic phase boundary on warming coincides with the boundary of C-CDW-1 and C-CDW-2 against the tetragonal phase. The cooling transition, $T_{\mathrm{s,cooling}}$, (dashed black line) determined by transport measurements is shown together, and the shaded region between two boundaries represents the hysteresis of the first-order structural transition. The superconducting transition temperatures, T_{c}, (red hollow squares) determined by transport measurements are shown together for comparison. χ_{nem}, $T_{\mathrm{s,cooling}}$, and T_{c} data are from Ref. [13].

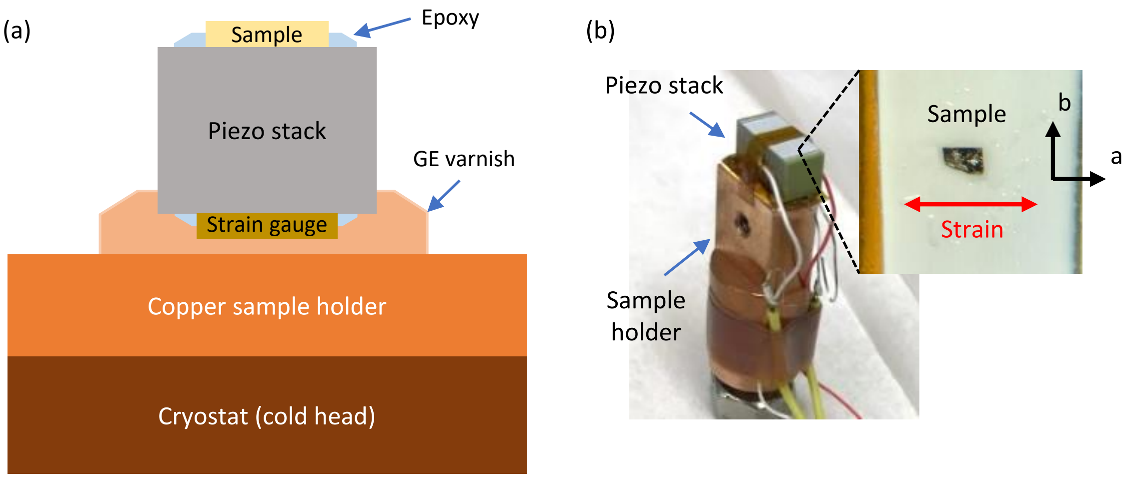

Figure 3.12: (a) Schematic drawing of a strain device. (b) Picture of a strain device mounted on a sample holder. Sample is mounted with its crystal a-axis parallel to the pulling direction of the piezo stack.

of the strain device. Samples were mounted on a piezoelectric stack (NEC-Tokin AE0505D08DF) using an epoxy (Devcon 5min epoxy), and the strain was controlled by applying a variable voltage to the stack. The thickness of the epoxy layer was kept being minimal to ensure it transmits strain to the sample. The strain was measured using a strain gauge (HBM 1-LC11-1.5/350) attached on the other side of the stack using the same type of epoxy. The strain device is attached on a sample holder using GE Varnish, which is electrically insulating and thermally conducting. In order to achieve a homogeneous strain distribution over the sample, samples were polished to a suitable thickness ($\leq 60\mu$m) using a Allied Multiprep System polisher at MRL, University of Illinois. Since $BaNi_2As_2$ and Co-, Sr-doped crystals are air-sensitive, the time that the sample is exposed to air was limited to 1-2 hours.

Preliminary measurements were performed on a $Ba_{0.73}Sr_{0.27}Ni_2As_2$ sample. The sample was mounted with its a-axis parallel to the pulling direction of the piezo stack, $\boldsymbol{\epsilon} \parallel (1,0,0)_{\text{tet}}$. Firstly, the temperature dependence of an IC-CDW reflection at $Q = (2, 1.28, 11)_{\text{tet}}$ was measured upon cooling with and without a finite strain, $\epsilon = 7 \times 10^{-4}$ (Fig. 3.13). The modulation vector of the IC-CDW reflection $\Delta Q = (0, 0.28, 0)_{\text{tet}}$ is perpendicular to the strain direction. The result shows that the development of IC-CDW is suppressed when the sample is under a strain, showing a lower onset temperature [Fig. 3.13(b)] and a suppressed peak with its intensity decreased by about 30 % [Fig. 3.13(a)]. The tetragonal-to-triclinic structural phase transition temperature, at which the IC-CDW is preempted by C-CDW-1 phase, is unchanged.

Secondly, the response of IC-CDWs whose modulation vector is parallel and perpendicular to the strain direction $\boldsymbol{\epsilon}$ are compared. The two IC-CDWs measured are $Q_1 = (-1.72, 1, 5)_{\text{tet}}$, which is parallel to the strain ($\Delta Q_1 = (0.28, 0, 0) \parallel \boldsymbol{\epsilon}$), and $Q_2 = (2, 1.28, 11)_{\text{tet}}$, perpendicular to the strain ($\Delta Q_2 = (0, 0.28, 0) \perp \boldsymbol{\epsilon}$).

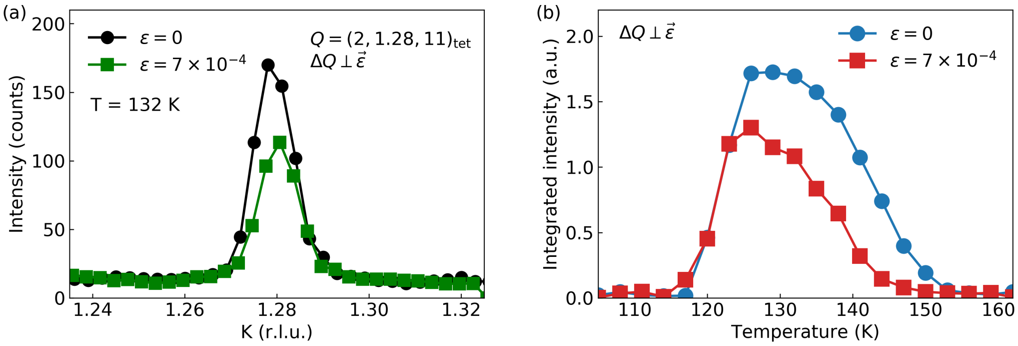

Figure 3.13: Strain response of IC-CDW at whose modulation vector is perpendicular to the strain direction. (a) K-scan of IC-CDW at $Q = G + \Delta Q = (2, 1, 11)_{\mathrm{tet}} + (0, 0.28, 0)_{\mathrm{tet}}$ at $\epsilon = 0$ and 7×10^{-4}, at $T = 132$ K. (b) Temperature dependence of IC-CDW intensity at $\epsilon = 0$ and 7×10^{-4}.

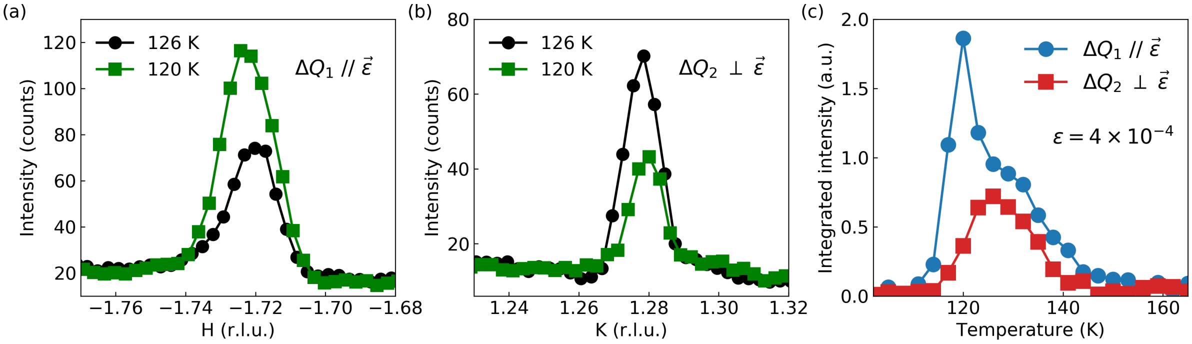

Figure 3.14: Comparison of temperature dependence of IC-CDWs whose modulation vector is perpendicular and parallel to the strain direction at $\epsilon = 4 \times 10^{-4}$. (a) H-scan of IC-CDW at $Q_1 = (-1.72, 1, 5)_{\mathrm{tet}}$ ($\Delta Q_1 = (0.28, 0, 0) \parallel \boldsymbol{\epsilon}$) and (b) K-scan of IC-CDW at $Q_2 = (2, 1.28, 11)_{\mathrm{tet}}$ ($\Delta Q_2 = (0, 0.28, 0) \perp \boldsymbol{\epsilon}$) at $T = 120$ K and 126 K. (c) Temperature dependence of IC-CDW at Q_1 and Q_2.

Temperature dependence of the two reflections under a finite strain $\epsilon = 4 \times 10^{-4}$ was measured (Fig. 3.14). Interestingly, the integrated intensity of IC-CDW at Q_1 showed a diverging behavior just above the structural transition temperature [Fig. 3.14(a), (c)], which resembles the temperature dependence of the nematic susceptibility measured by an elastoresistivity method [13]. Unlike Q_1, the IC-CDW at Q_2 did not show such diverging behavior and the intensity decreased to disappear across the structural phase transition. This preliminary observation of the different properties of IC-CDW depending on its relative modulation direction with respect to the strain provides an evidence that the IC-CDW phase is closely related to the nematic phase in $\mathrm{Ba}_{1-x}\mathrm{Sr}_x\mathrm{Ni}_2\mathrm{As}_2$.

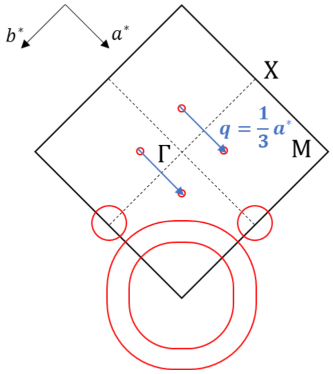

Figure 3.15: Schematic drawing of the two-dimensional projection of Brillouin zone (black lines) of $BaNi_2As_2$, and Fermi surface in triclinic phase (red circles). The CDW wave vector $(1/3, 0, 0)_{\mathrm{tri}}$ (blue arrows) roughly connects the small hole-like Fermi surfaces around Γ point. The drawing of the Fermi surface is adapted from Ref. [66].

3.3 Discussion

In summary, we showed using x-ray scattering that the pnictide superconductor $Ba(Ni_{1-x}Co_x)_2As_2$ and $Ba_{1-x}Sr_xNi_2As_2$ exhibit a CDW instability. Upon Co and Sr doping, the CDW orders are suppressed and a dome-shaped superconducting phase appears, that suggests CDW in this material plays a role analogous to antiferromagnetism in iron-pnictide superconductors. Interestingly, in $Ba_{1-x}Sr_xNi_2As_2$, it has been observed that transport and magnetic susceptibility measurements show an enhancement of T_{c} centered at $x_{\mathrm{c}} = 0.7$, but heat capacity measurements show that the bulk thermodynamic signature of T_{c} remains unchanged for $0.4 \leq x \leq x_{\mathrm{c}}$ [13]. The doping range where this filamentary SC state is observed coincides with that where C-CDW-2 is present, and the bulk SC is only established for $x \geq x_{\mathrm{c}}$, where the C-CDW-2 is not present. Similarly, C-CDW-2 phase is not present in $Ba(Ni_{1-x}Co_x)_2As_2$ and the SC phase is found to be a bulk property [17]. These observations suggest that this filamentary SC state is closely related to the presence of C-CDW-2 phase, presumably due to the formation of SC at CDW domain boundaries, which has been previously observed in iron-pnictides and transition metal dichalcogenide materials [67–70].

The commensurate CDW in $BaNi_2As_2$ coincides with unusual changes in the electronic structure. Angle-resolved photoemission spectroscopy (ARPES) studies of $BaNi_2As_2$ found that its α-band shifts significantly with temperature and opens Fermi surface pockets below T_{tri} [66]. The CDW wave vector, $(1/3, 0, 0)_{\mathrm{tri}}$, nests these hole-like α pockets (Fig. 3.15), suggesting they may have some connection to the CDW formation. However, no energy gap is observed to open at T_{tri}, and no evidence for band folding, which would be expected when translational symmetry is broken, is observed. We conclude that the observed CDW is unconventional in that it is connected to electronic structure changes but does not follow a traditional Fermi surface nesting paradigm [61].

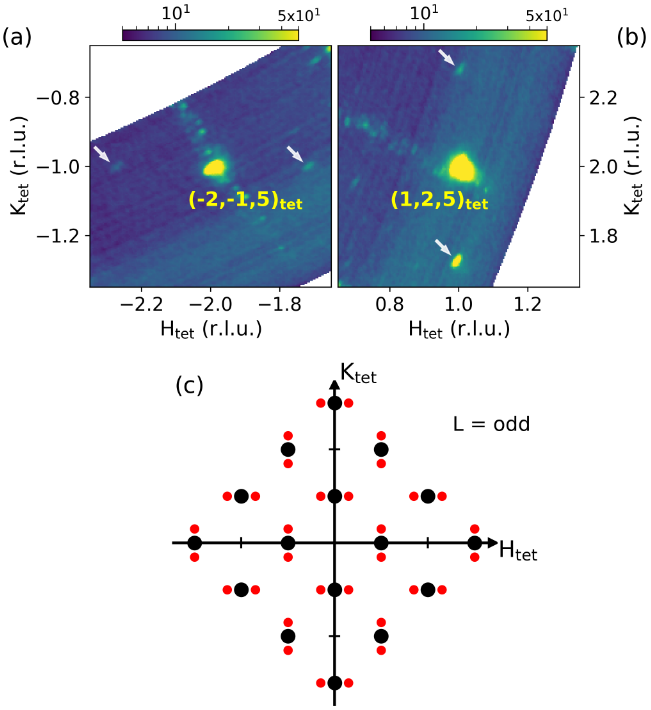

Figure 3.16: H-K maps at $L = 5$ in $x = 0.42$ at $T = 120$ K around (a) $(-2,-1,5)_{\text{tet}}$ and (b) $(1,2,5)_{\text{tet}}$. The structural Bragg reflections are shown at the center of the maps, and the satellite IC-CDW reflections are indicated with white arrows. (c) Schematic drawing of the symmetry pattern of the IC-CDW in H-K maps when L is an odd number showing the location of IC-CDW reflections (red dots) around the structural Bragg reflections (black dots).

While the IC-CDW was reported to be unidirectional in an earlier report, Ref. [43], a wide momentum space mapping revealed that the IC-CDW is actually bidirectional, but with a peculiar symmetry. In any Brillouin zone, the IC-CDW reflections appear only along one direction, either H or K direction, but never along both directions. Figure 3.16 shows the symmetry pattern of IC-CDW found in $x = 0.42$. The IC-CDW phase appears when the system is in tetragonal crystal structure in which H and K directions are equivalent. However, the H-K maps show that the satellite IC-CDW reflections appear only along one direction, either H or K. For example, in $x = 0.42$, around (H, K, L) = (-2, -1, 5)$_{\text{tet}}$ Bragg reflection, the IC-CDW reflections appear at $(-2 \pm 0.28$, -1, 5)$_{\text{tet}}$, but not at (-2, -1 ± 0.28, 5)$_{\text{tet}}$ [Fig. 3.16(a)]. Interestingly, the pattern is the opposite around (1, 2, 5)$_{\text{tet}}$ Bragg reflection that the IC-CDW reflections appear at (1, 2 ± 0.28, 5)$_{\text{tet}}$, but not at (1 ± 0.28, 2, 5)$_{\text{tet}}$ [Fig. 3.16(b)]. Unlike the IC-CDW, C-CDW-1 and C-CDW-2 were found to be unidirectional (Fig. 3.17), which is consistent with the fact that the underlying lattice of the commensurate phases is in triclinic structure in which H and K directions are not equivalent.

While the observation of H- and K-direction satellites establishes that the IC-CDW is bidirectional, the fact that the satellites in a specific Brillouin zone never appears on both directions implies that the

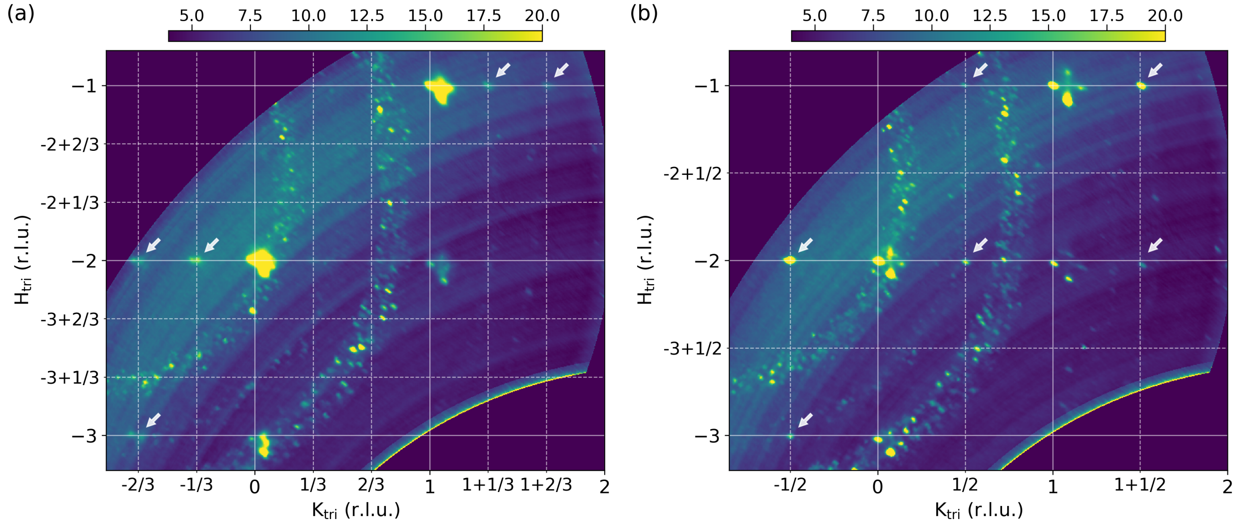

Figure 3.17: (a) H-K map at $L = 6$ in $x = 0.42$ at $T = 110$ K showing C-CDW-1 reflections along K direction, not along H direction, in multiple Brillouin zones, indicating the C-CDW-1 is unidirectional. (b) Similar map at $T = 9$ K showing C-CDW-2 reflections along K direction, not along H direction, in multiple Brillouin zones, indicating the C-CDW-2 is unidirectional.

symmetry of the IC-CDW phase imposes a non-trivial extinction rule [Fig. 3.16(c)]. Moreover, as presented in the previous section, the H- and K-satellites show different behaviors under a uniaxial strain, and further strain response measurements will help understanding the characteristics of the symmetry and a possible nematicity of IC-CDW phase.

Chapter 4

Evolution of charge order wave vector in $La_{1.8-x}Eu_{0.2}Sr_xCuO_4$

This chapter has been adapted from Ref. [71].

4.1 Introduction: distinct properties of charge density waves in different cuprate families

While CDW is recognized as a universal phenomenon in high-T_c cuprates, different families of cuprates exhibit distinct properties of CDW [12, 22, 54]. One of the differences is the evolution of the CDW wave vector upon hole doping. In the case of some families of cuprates including $YBa_2Cu_3O_{6+\delta}$ (YBCO) [72, 73], $Bi_2Sr_{2-x}La_xCuO_{6+\delta}$ [28] and $Bi_2Sr_2CaCu_2O_{8+\delta}$ [27, 74], the CDW wave vector decreases with increasing doping, and it was reported that the Fermi surface nesting model can explain the doping evolution very accurately [28]. On the contrary, La-based cuprates such as $La_{2-x}Ba_xCuO_4$ (LBCO) [14] and $La_{2-x}Sr_xCuO_4$ [16] exhibit the opposite relationship that the CDW wave vector increases upon doping. This apparent disparity between the La-based family and the others has raised a question whether the CDWs sharing the same origin are subjected to different environments, or they are just totally unrelated. The answer is yet to be found and it has been a great obstacle in the search for a unified mechanism of CDW phenomenon in high-T_c cuprates.

The spin density wave (SDW), which is absent in YBCO and Bi-based compounds, is believed to play an important role on the low-temperature properties of CDW in La-based cuprates. The coupling between the two orders is manifested in the relationship between their wave vectors, that the CDW wave vector is twice of the SDW wave vector when the two orders coexist [23, 75, 76]. The SDW wave vector is observed to follow the so-called Yamada relationship, in which it has the same value as the hole doping x for $x \leq \frac{1}{8}$, and then saturates at $\frac{1}{8}$ for $x > \frac{1}{8}$ [29]. Following this relationship, the CDW wave vector of La-based cuprates with $\frac{1}{8}$ doping is close to $\frac{1}{4}$ [25] and it is distinct from the case of YBCO whose CDW wave vector is close to $\frac{1}{3}$ [26]. However, a study on $\frac{1}{8}$ doping LBCO found that above 55 K the CDW wave vector is unlocked from the SDW wave vector and shifts toward a higher value that is closer to the CDW wave vector of YBCO [31].

This finding suggests that the presence of SDW and its coupling to CDW may be playing a crucial role in the distinct CDW behavior in La-cuprates.

In this chapter, we present a direct evidence that the cuprates share the same underlying CDW mechanism by showing that the doping evolution of CDW wave vector in a La-cuprate at a high-temperature follows the same trend that is observed in YBCO and Bi-based compounds.

4.2 Results

We used resonant soft x-ray scattering (RSXS) to measure changes of CDW wave vector upon doping and temperature in $La_{1.8-x}Eu_{0.2}Sr_xCuO_4$ (LESCO). LESCO is an ideal system for studying properties of CDW since, unlike other La-cuprates, the low-temperature tetragonal (LTT) structural transition temperature is high enough that the observation of the occurrence of CDW does not suffer from complications of being coupled to the LTT transition [24, 77, 78]. Moreover, a recent high-resolution resonant inelastic x-ray scattering (RIXS) study showed that the CDW in $\frac{1}{8}$ doping LESCO persists above the LTT transition temperature and its peak amplitude continuously decays, suggesting that the CDW and LTT phase are unrelated [79].

Single crystals of $La_{1.8-x}Eu_{0.2}Sr_xCuO_4$ with $x = 0.07$, 0.10, 0.125, 0.15, 0.17, and 0.20 were studied using RSXS at SSRL beamline 13-3. In order to subtract fluorescence backgrounds accurately, and thereby enhance sensitivity of RSXS measurements, we employed a two-dimensional CCD detector which measures CDW signals and backgrounds simultaneously. The background subtraction method is described in the section 2.3.4. The crystals were grown using floating-zone method by Thomas Johnson and Alexander Zakrzewski, from the MacDougall group at the University of Illinois.

4.2.1 Determination of hole doping levels

Hole doping levels of the LESCO samples are determined by two factors: Sr concentration and oxygen non-stoichiometry. In order to confirm that oxygen non-stoichiometry is minimal and the doping is controlled by Sr concentration, we have performed x-ray absorption spectroscopy (XAS) experiments as a direct measurement of hole concentration of the samples. It has been observed that O K edge XAS spectra of hole-doped high-T_c cuprates exhibit two pre-edge peaks and the intensity of the lower energy peak increases linearly with hole concentration in the doping range of 0 to 20% [46, 80–82]. The XAS measurements were performed using a transition-edge-sensor detector [83, 84] in total fluorescence yield mode.

Figure 4.1(a) shows the O K edge XAS spectra of the LESCO samples that were used in this study, which resemble the spectra of $La_{2-x}Sr_xCuO_4$ reported in Ref. [80]. The pre-edge regions of the result are analyzed

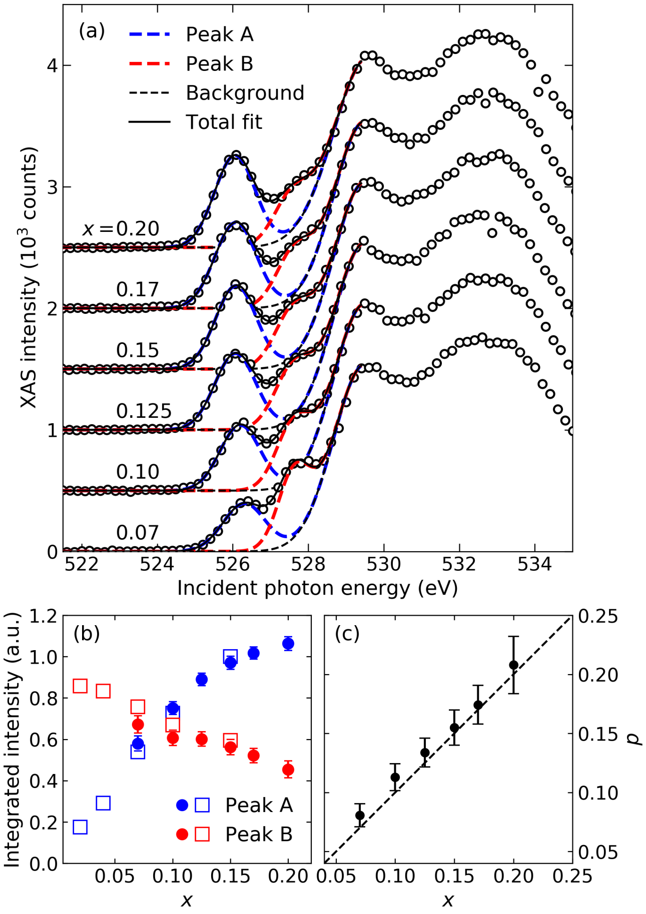

Figure 4.1: (a) Oxygen K-edge XAS spectra of LESCO samples. The pre-edge regions of the spectra exhibit two distinct peaks which are fitted with two Gaussian functions (peak A: blue dashed curves, peak B: red dashed curves) and a background (gray dashed curves). The total lineshapes (solid lines) fit well to the XAS data points. (b) Doping evolution of integrated intensities of peak A and B (filled circles). For a comparison, data points from the same analysis on LSCO in Ref. [80] are plotted together (hollow squares). (c) Measured hole doping p plotted against Sr concentration x. Dashed line represents $p = x$.

in the same way described in Ref. [80], where the background is modeled with a Gaussian function and the two pre-edge peaks (the lower-energy peak: peak A, the higher-energy peak: peak B) are fitted with two Gaussian lineshapes, and the integrated intensities of peak A and B are obtained [Fig. 4.1(b)]. According to Ref. [80], the relationship between the ratio of the intensities of two pre-edge peaks, $I_{\text{peakA}}/I_{\text{peakB}}$ and the hole doping p is found to be $I_{\text{peakA}}/I_{\text{peakB}} = (11.6 \pm 0.4)p - (0.076 \pm 0.03)$. Using this relationship, we estimated the doping level p of the LESCO samples [Fig. 4.1(c)] and it agrees well with Sr concentration x.

4.2.2 RSXS scans of charge density wave

RSXS measurements of CDW were performed using a photon energy of Cu L_3 edge. CDW was observed in the samples with $0.10 \leq x \leq 0.20$, but not in the sample with the lowest doping $x = 0.07$. RSXS

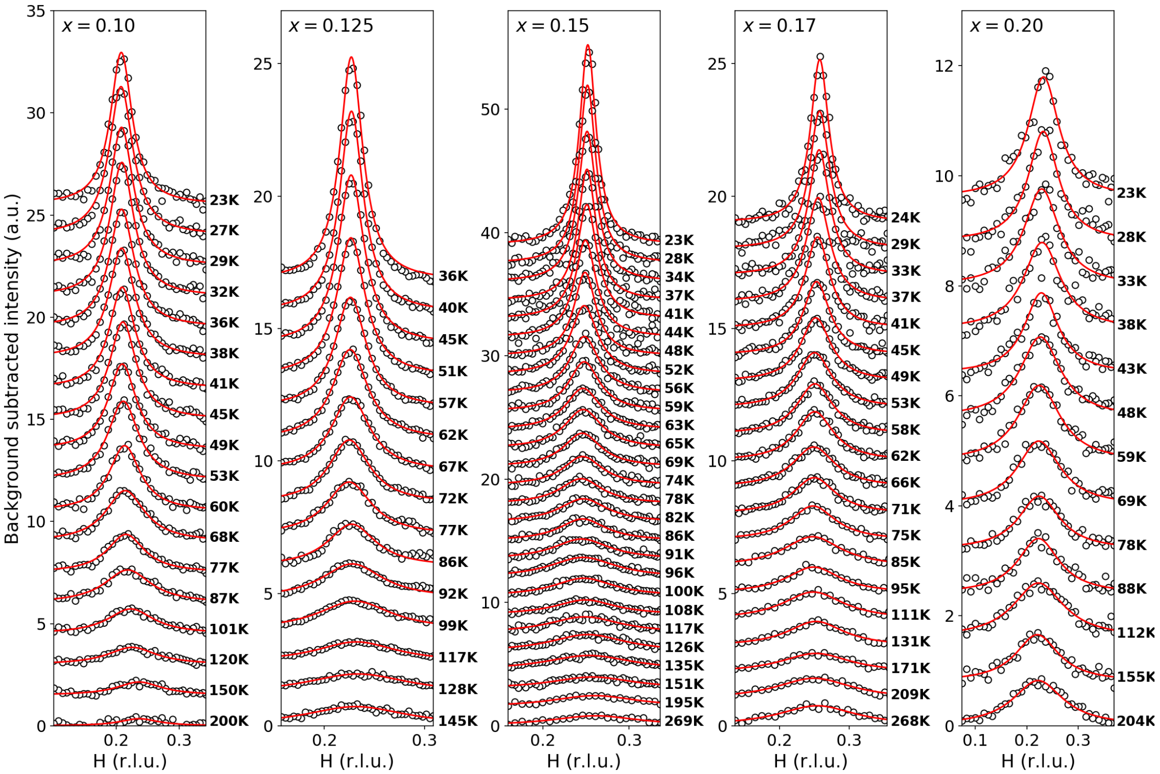

Figure 4.2: Background subtracted H-scans of CDW of LESCO x=0.10, 0.125, 0.15, 0.17 and 0.20 at a wide range of temperature. The red solid lines are Lorentzian fits.

scans of CDW in LESCO $0.10 \leq x \leq 0.20$ are shown in Fig. 4.2. The CDW peak profiles along the in-plane momentum direction H were measured by performing scans of the sample angle θ with respect to the incident x-ray beam. There have been attempts in the past to characterize the onset of CDW in LESCO. RSXS studies on LESCO $0.10 \leq x \leq 0.15$ showed that the CDW exhibits a phase transition at T_{CDW} with its maximum of 80 K at $x = 0.125$ [24,44], while a high-resolution RIXS study on LESCO $x = 0.125$ revealed high-temperature correlations above the T_{CDW} [79]. In this study, agreeing with the latter observation, we observed that the CDW correlations persist above the previously determined T_{CDW} without a clear phase transition. In every sample with $0.10 \leq x \leq 0.20$, the CDW peak weakens and broadens on warming, but does not disappear up to the highest measured temperature, $T = 270$ K in the case of $x = 0.15$.

To quantify the evolution of the CDW peak profiles, H-scans at each doping and temperature are fitted with a Lorentzian function (Fig. 4.2). From the fits, we obtained the peak intensity I_{peak}, the correlation length ξ, and the H component of wave vector Q_{CDW}. The correlation length ξ is defined by a/half-width at half-maximum (HWHM). Figure 4.3(a) and 4.3(b) shows the temperature dependence of I_{peak} and ξ, respectively, that exhibits a gradual ordering of CDW upon cooling in all dopings with the absence of a sharp transition. One intriguing aspect of the ordering was recently found in LESCO $x = 0.125$ that $I_{\mathrm{peak}} \propto \xi^2$,

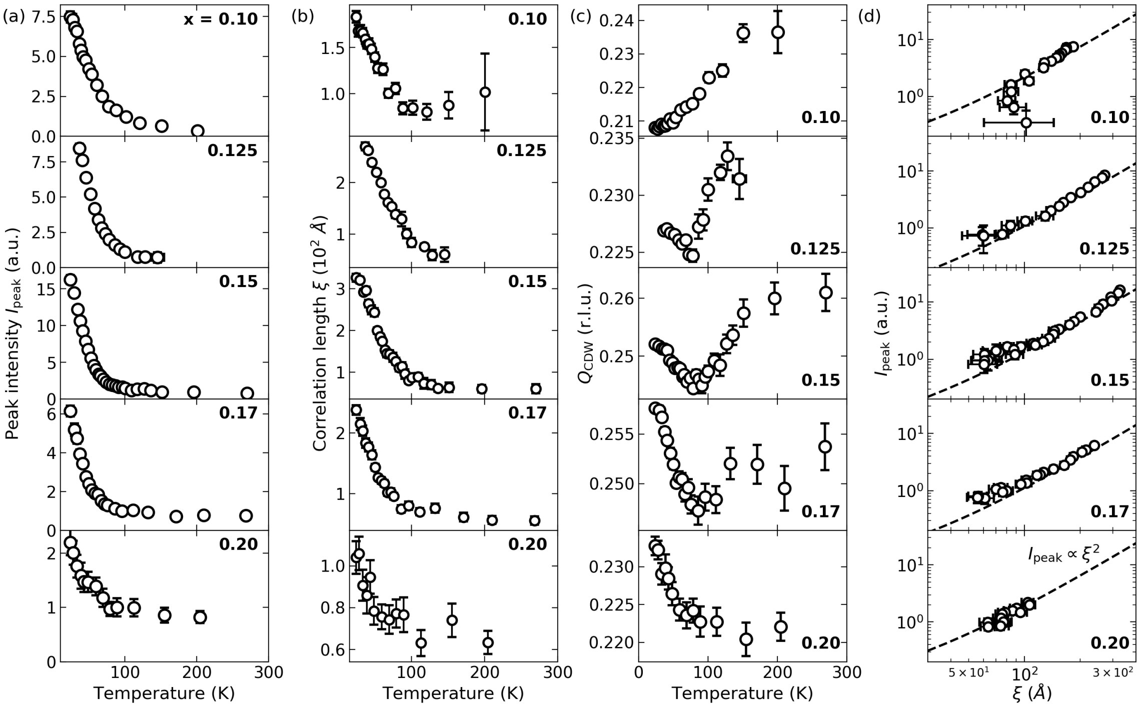

Figure 4.3: Temperature dependence of CDW peak profile obtained from fits with a Lorentzian function: (a) peak intensity, (b) correlation length, and (c) Q_{CDW}. (d) Peak intensity plotted against correlation length in logarithmic scale. Dashed lines represents the best fits of $I_{\text{peak}} \propto \xi^2$ to the data points.

suggesting that the in-plane integrated intensity of CDW is independent on temperature [79]. Our results confirm that this relationship is found in all dopings [Fig. 4.3(d)], making it an universal phenomenon of CDW in LESCO.

Unlike I_{peak} and ξ whose temperature dependences are similar in all dopings, Q_{CDW} exhibits a distinct behavior in different dopings. In Fig. 4.3(c), we displayed the nonmonotonic evolution of Q_{CDW} upon doping and temperature. At $x = 0.10$, Q_{CDW} continuously decrease upon cooling from 0.236 reciprocal lattice units (r.l.u.) at T = 200 K to 0.208 r.l.u. at T = 24 K. At x = 0.125 and 0.15, while the same tendency of continuous decrease of Q_{CDW} is observed at higher temperatures, a kink in its temperature dependence appears around $T \sim 75$ K and Q_{CDW} increases below the kink: at $x = 0.15$, Q_{CDW} decrease from 0.261 r.l.u. at T = 270 K to 0.244 r.l.u. at T = 78 K, and then increase to 0.251 r.l.u. at T = 24 K. The downward tendency above the kink becomes less significant at $x = 0.17$ and is no longer seen at $x = 0.20$ making Q_{CDW} increase for the entire temperature range, from 0.222 r.l.u. at T = 207 K to 0.233 r.l.u. at T = 24 K, while the kink at $T \sim 60$ K is still present.

There have been observations of Q_{CDW} shifting in several different materials with stripe order. In $La_{2-x}Ba_xCuO_4$, for example, the variation of Q_{CDW} at high-temperatures was observed due to the unlocking of CDW from SDW [31], and in $La_{2-x}Sr_xNiO_4$ the commensurability effect toward 1/3 r.l.u. was observed

[85]. Such materials exhibit a monotonic change of Q_{CDW} from its intrinsically favored high-temperature value to a low-temperature value to which the ordering is locked as a result of coupling to another ordering phase. However, the nonmonotonic evolution of Q_{CDW} in LESCO presented in this study implies that there are two or more effects that compete to determine Q_{CDW}.

4.2.3 Lineshape analysis: phase fluctuation model

For all dopings, the evolution of the spectra with temperature is gradual and we do not find any indication of a sharp transition, or even a rounded transition. This may suggest that the CDW is weak and that the spectra indicate merely incipient CDW fluctuations. However, such an interpretation is at odds with the significant correlation length, approaching ~ 100 unit cells at low temperature. Another possibility is that the nominal CDW transition temperature, in the absence of disorder, is higher than the highest temperatures considered. In this scenario, the amplitude of the CDW is already well-formed at all temperatures considered, and gradual evolution of the spectra reflect the coupling of disorder with CDW order and the suppression of phase fluctuations as temperature is lowered. This perspective is supported by our finding that $I_{\text{peak}} \propto \xi^2$ over the range of measured temperatures [Fig. 4.3(d)]. If a similar temperature dependence of the correlation length in the K direction is assumed, this suggests that the in-plane integrated intensity, expected to be proportional to the CDW amplitude, is not significantly temperature dependent.

For a quantitative test of whether phase fluctuations can account for the temperature dependence of the spectra, we used a non-linear sigma model described in Ref. [86]. The effects of disorder are taken into account by writing the structure factor S in terms of an ideal disorder-free susceptibility G

$$S(\boldsymbol{Q}_{\text{CDW}} + \boldsymbol{q}) = TG(\boldsymbol{q}) + \sigma^2 G^2(\boldsymbol{q}) \tag{4.1}$$

$$G(\boldsymbol{q}) = \frac{1}{\kappa_{\parallel} q_x^2 + \kappa_{\perp} q_y^2 + \mu}, \tag{4.2}$$

where σ characterizes the disorder strength, $\kappa_{\parallel}$ and $\kappa_{\perp}$ are coefficients of gradient terms in the effective Hamiltonian given in Ref. [86]. The peak width is determined by the ratio of μ to $\kappa_{\parallel}$ and its temperature dependence is contained implicitly in μ. The self-consistency of the model imposes a sum rule on the integrated scattering intensity,

$$1 = \int \frac{d^2 q}{(2\pi)^2} S(q), \tag{4.3}$$

from which μ can be determined. Note that this condition accounts for the observation of temperature

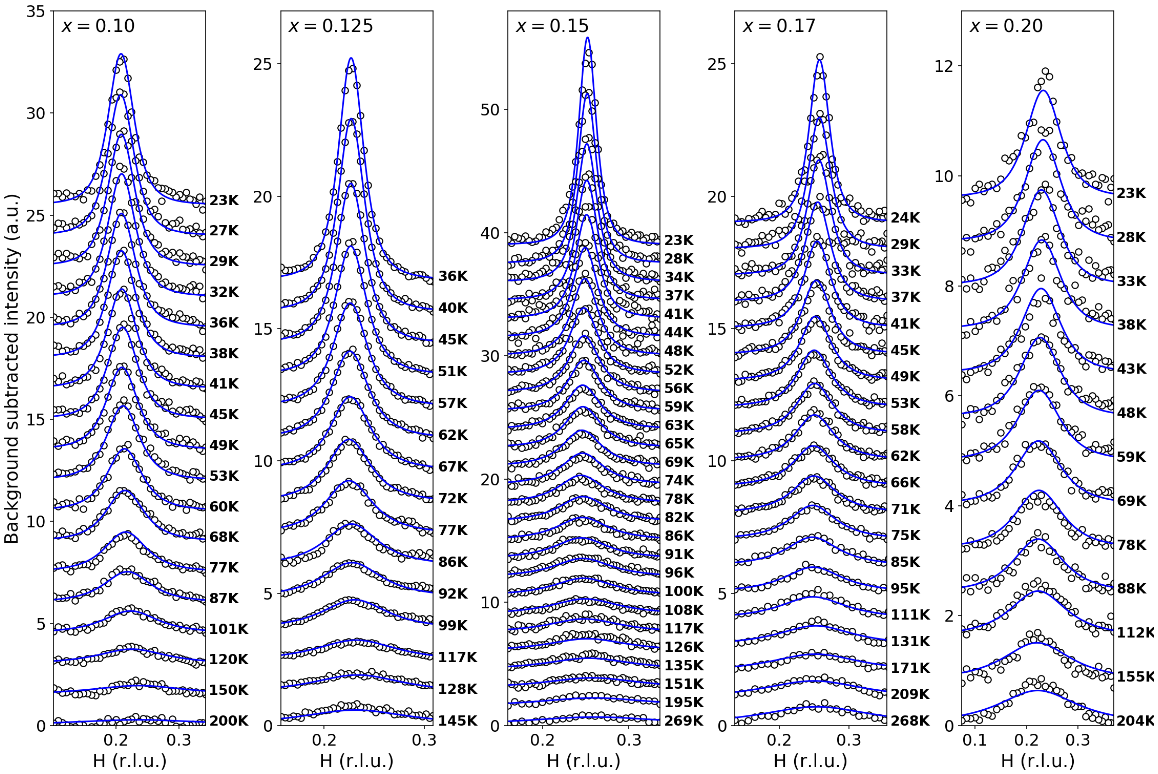

Figure 4.4: Fits of CDW scans using the non-linear sigma model. The blue solid lines are fits with $S(q,T)$ given by Eq. (4.1).

independent integrated intensity [Fig. 4.3(d)]. From (4.1), the self-consistency condition gives

$$1 = TA_1(\mu) + \sigma^2 A_2(\mu) \tag{4.4}$$

where

$$A_n(\mu) = \int \frac{d^2q}{(2\pi)^2} [G(q)]^n. \tag{4.5}$$

Evaluating for $n = 1, 2$,

$$A_2(\mu) = \frac{1}{4\pi\sqrt{\kappa_\parallel \kappa_\perp}} \frac{1}{\mu}, \quad A_1(\mu) = \frac{1}{4\pi\sqrt{\kappa_\parallel \kappa_\perp}} \int_\mu^\Gamma \frac{dx}{x} = \frac{1}{4\pi\sqrt{\kappa_\parallel \kappa_\perp}} \ln\left[\frac{\Gamma}{\mu}\right] \tag{4.6}$$

where Γ is a UV cutoff. If we assume that the CDW is isotropic, that is $\kappa_\parallel = \kappa_\perp = \kappa$, the temperature dependence of μ is determined by

$$4\pi\kappa = T \ln\left[\frac{\Gamma}{\mu}\right] + \frac{\sigma^2}{\mu}. \tag{4.7}$$

We performed a fit of the CDW scans with the lineshape given by Eq. (4.1) with $G = \frac{1}{\kappa q^2 + \mu(T)}$. The model has only four free parameters: κ, σ, Γ, and an overall normalization factor A. For each doping, the

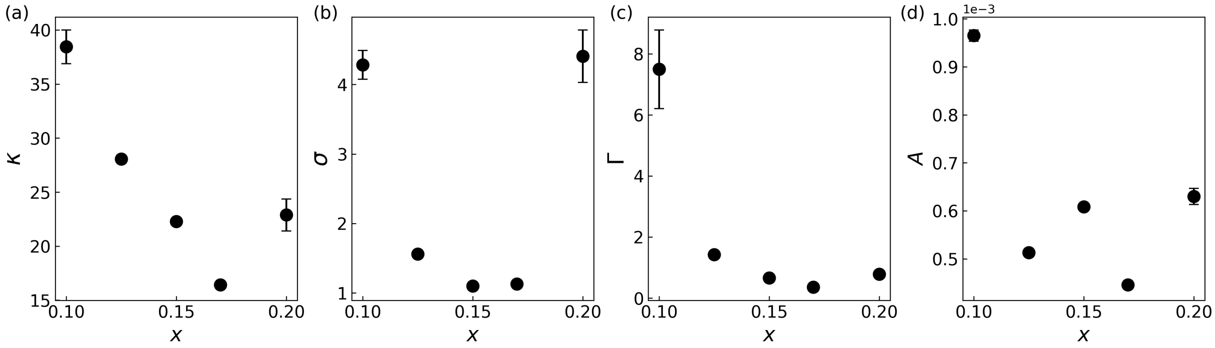

Figure 4.5: $S(q,T)$ fitting result. Doping dependence of fit parameters: (a) κ, (b) σ, (c) Γ, and (d) A.

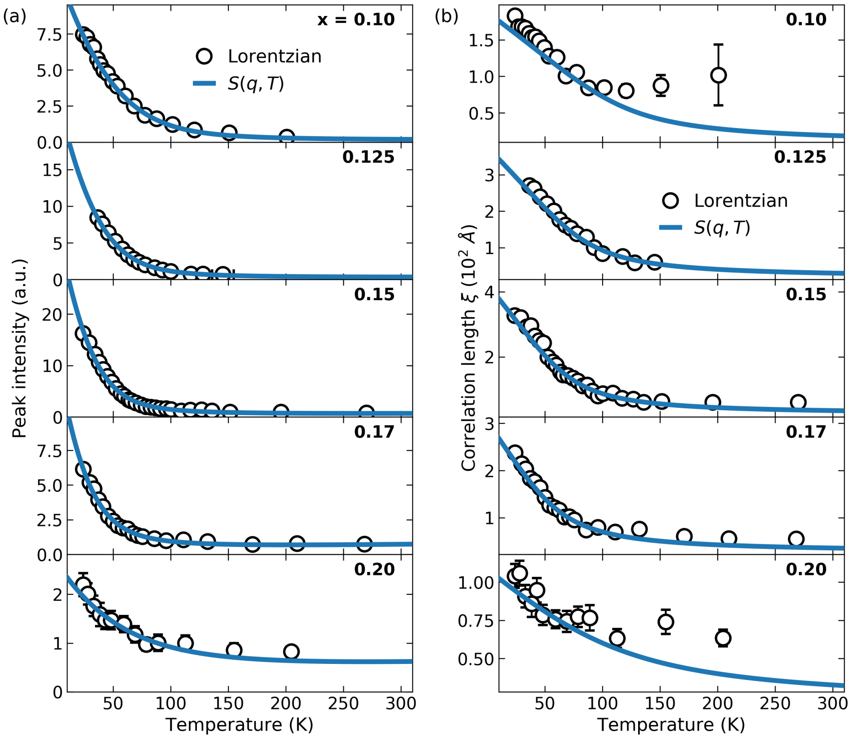

Figure 4.6: Temperature dependence of (a) CDW peak intensity and (b) correlation length obtained from fits with a Lorentzian function (open circles) and $S(q,T)$ in Eq. (4.1) (solid lines).

fitting with $S(q,T)$ uses a single set of parameters to fit the entire dataset of momentum- and temperature-dependent scattering intensity, and the fit parameters were temperature independent. Here, since we are only fitting the lineshape, we always consider momentum q that is relative to Q_{CDW}. Despite the simplicity of the model, having only four temperature independent parameters, we find that for every doping the model lineshape $S(q,T)$ fits well to the entire two-dimensional set of data (Fig. 4.4, 4.5). Indeed, the solid lines in Fig. 4.6 compare remarkably well to the results of the Lorentzian fits where parameters are temperature-dependent. This analysis strongly suggests that the temperature dependence of the lineshape is predominantly related to the effects of disorder on thermal phase fluctuations of the CDW, and that the CDW amplitude is strong up to the highest experimental temperatures.

4.2.4 Q_{CDW} shifting analysis: Landau-Ginzburg theory

The non-monotonic behavior of Q_{CDW}, with a pronounced kink in the temperature dependence, suggests the role of multiple effects that interact to determine the ordering wavevector. Noting that the kink occurs at temperatures comparable to the onset temperature of SDW order seen in LESCO $x = 0.15$ by neutron scattering [87], and that the mutual commensurability of CDW and SDW orders is known to be strong in La-based cuprates, we posit that the low-temperature behavior of Q_{CDW} is related to the onset of SDW order. The behavior at higher temperatures would be related to other effects. While the microscopic mechanism of CDW order in cuprates is not fully understood, we can still describe the data by an effective theory. Because of the significant variation of Q_{CDW} with temperature and doping, even in the absence of SDW order, such a theory must account for the finite electronic compressibility of the system.

Thus, for a minimal theoretical description of the non-monotonic temperature dependence of Q_{CDW}, we start with the Landau-Ginzburg theory for an incommensurate CDW in a system with finite compressibility discussed in Ref [88], which is an extension of the standard Landau theory for CDW due to McMillan [89] for a system with finite compressibility. We will first consider the case when there is only CDW order, and the SDW order and the CDW-SDW coupling will be included later on.

CDW only (without SDW)

The approach in this section closely follows Ref. [89]. We will consider a three-dimensional system with a unidirectional CDW, with ordering wave vector $\boldsymbol{Q} = Q\hat{\boldsymbol{Q}}$. In a CDW phase the local charge density has the expansion

$$\rho(\boldsymbol{x}) = \psi_0(\boldsymbol{x}) + i\Lambda\psi^*(\boldsymbol{x})\hat{\boldsymbol{Q}} \cdot \boldsymbol{\nabla}\psi(\boldsymbol{x}) + \text{c.c.} + \psi(\boldsymbol{x})\exp(i\boldsymbol{Q}\cdot\boldsymbol{x}) + \psi^*(\boldsymbol{x})\exp(-i\boldsymbol{Q}\cdot\boldsymbol{x}) + \dots \tag{4.8}$$

where $\psi(\boldsymbol{x})$ is the CDW complex order parameter and $\psi_0(\boldsymbol{x})$ is the "normal" component of charge density that is not tied to the CDW. The dimensionless parameter Λ reflects the change of the density which results from a compression of the CDW. Finally, $\boldsymbol{Q}$ is the "ideal" CDW ordering wave vector.

The Landau-Ginzburg free energy is given by

$$\begin{aligned} F_{\text{CDW}} = &\int d^3x \Big\{ \frac{1}{2} K_c \Big| \Big(i\hat{\boldsymbol{Q}} \cdot \boldsymbol{\nabla} + \delta_0 \Big) \psi(\boldsymbol{x}) \Big|^2 + \frac{r_c}{2} |\psi(\boldsymbol{x})|^2 + u_c |\psi(\boldsymbol{x})|^4 \Big\} + \int d^3x \frac{\kappa_0}{2} (\psi_0(\boldsymbol{x}) - \rho_N)^2 \\ &+ \frac{1}{2} \int d^3x \int d^3y (\rho(\boldsymbol{x}) - \bar{\rho}) V(|\boldsymbol{x} - \boldsymbol{y}|)(\rho(\boldsymbol{y}) - \bar{\rho}) \end{aligned} \tag{4.9}$$

where K_c is the stiffness of the CDW order parameter, $\bar{\rho}$ is the average charge density given by $L^3 \bar{\rho} = \int d^3x \rho(\boldsymbol{x})$, and $r_c = T - T^0_{\text{CDW}}$ with T^0_{CDW} being the usual mean field CDW critical temperature. The last term represents the long-range Coulomb interaction of the charge configurations $\rho(\boldsymbol{x})$ given in Eq. (4.8), and

$$V(|\boldsymbol{x} - \boldsymbol{y}|) = \frac{e^2}{\varepsilon} \frac{1}{|\boldsymbol{x} - \boldsymbol{y}|} \tag{4.10}$$

where ε is the dielectric constant.

The second term in Eq. (4.9) governs the fluctuations of the normal density from the preferred density ρ_N, and κ_0 is the inverse compressibility of the normal fluid. The normal density and the CDW order parameter are coupled through the Coulomb interaction, as given in the last term of Eq. (4.9). Integrating out the fluctuations results in an effectively screened Coulomb interaction, with a screening length $\xi = \left(\frac{4\pi\varepsilon}{e^2} \kappa_0\right)^{1/2}$ tuned by κ_0. This means that if $\kappa \to 0$ the interaction is ultra-local due to the perfect screening, and if $\kappa \to \infty$ there is no screening. In this effective interaction, we also determine the average value of normal charge density $\bar{\psi}_0$ is given by

$$\bar{\psi}_0 = \bar{\rho} - 2\Lambda |\psi|^2 \delta \tag{4.11}$$

which shows that the incommensuration δ shifts the average value of the compressible charge density away from the average density $\bar{\rho}$.

We will assume the incommensurate CDW order parameter has the form of $\psi(x) = \phi_0 \exp(i\delta \hat{\boldsymbol{Q}} \cdot \boldsymbol{x})$, where δ is the incommensuration and ϕ_0 is the CDW amplitude. Hence, the actual CDW ordering wave vector has a magnitude $Q_{\text{CDW}} = Q + \delta$, along the direction $\hat{\boldsymbol{Q}}$. Under this ansatz, the free energy density of the CDW state is

$$f_{\text{CDW}} = \frac{1}{2} K_c (\delta - \delta_0)^2 |\phi_0|^2 + \frac{1}{2} \left(r_c + 2\tilde{V}_{\text{eff}}(Q_{\text{CDW}}) \right) |\phi_0|^2 + u_c |\phi_0|^4 + \frac{\kappa_0}{2} (\Delta\bar{\rho} + 2\Lambda |\phi_0|^2 \delta)^2. \tag{4.12}$$

where $\Delta\bar{\rho} = \bar{\rho} - \rho_N$ which qualitatively represents the doping level and

$$\tilde{V}_{\text{eff}}(Q_{\text{CDW}}) = \frac{\frac{e^2}{4\pi\varepsilon}}{Q_{\text{CDW}}^2 + \xi^{-2}} \tag{4.13}$$

is the Fourier transform of the screen Coulomb interaction at the wave vector Q_{CDW} and ξ is the screening length.

Upon extremizing the free energy density Eq. (4.12) with respect to δ, we obtain

$$\delta = \delta_0 \left(\frac{b^2 - a^2}{b^2 + |\phi_0|^2} \right) \tag{4.14}$$

which shows that the incommensuration δ depends explicitly on ϕ_0, the amplitude of the CDW, which depends on the temperature, where a and b are defined as

$$a^2 = \frac{\Delta\bar{\rho}}{2\Lambda\delta_0}, \qquad b^2 = \frac{K_c}{4\Lambda^2\kappa_0}. \tag{4.15}$$

By substituting δ in Eq. (4.12) with Eq. (4.14), we obtain

$$f_{\text{CDW}} = \frac{1}{2}K_c\delta_0^2 \, \frac{(a^2 + |\phi_0|^2)^2}{b^2 + |\phi_0|^2} + \frac{1}{2}(r_c + 2\tilde{V}_{\text{eff}}(Q_{\text{CDW}}))|\phi_0|^2 + u_c|\phi_0|^4. \tag{4.16}$$

This expression differs from the conventional expression of CDW free energy density, which can be obtained by taking the limit of $\kappa \to 0$, that does not consider a case of a finite compressibility. For $\kappa = 0$, the incommensurability is determined by $\delta = \delta_0$, which can be obtained from Eq. (4.14), without a temperature dependence. For a system with a finite compressibility, thus having imperfectly screened Coulomb interactions, the optimal value of δ is determined by a combination of δ_0, a and b.

By numerically minimizing the CDW free energy density, Eq. (4.16), we obtain the incommensurability δ as a function of temperature. Figure 4.7 shows the temperature dependence of δ for several values of $z = \frac{b^2}{a^2}$, where temperature is parametrized by $s = (r_c + 2\tilde{V}_{\text{eff}}(Q_{\text{CDW}})/K_c\delta_0^2$. This result shows that a monotonic temperature dependence of the CDW ordering wave vector can be explained as a consequence of the finite compressibility. However, these expressions alone cannot describe the non-monotonic behavior seen in the experiments. Next we will see that the non-monotonicity can be explained by the interaction between the CDW and the SDW.

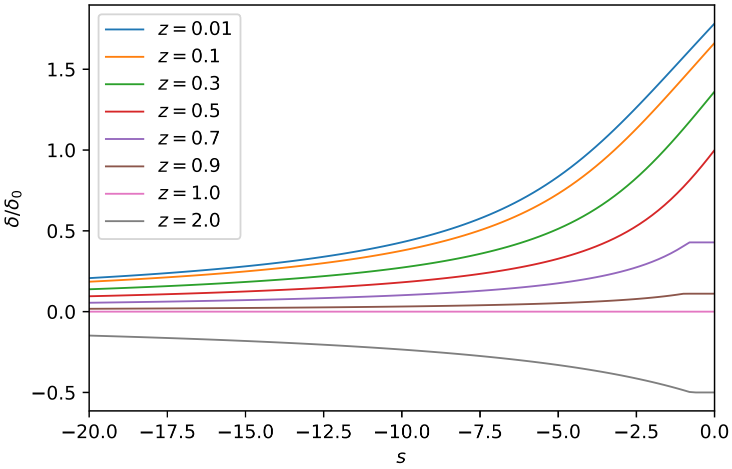

Figure 4.7: Incommensurability δ of Eq. (4.14) as a function of temperature (represented by s) for different values of z, controlled by the compressibility κ_0.

CDW with SDW

We now include the SDW and its interaction with the CDW. The free energy of the full system is

$$F = F_{\mathrm{CDW}} + F_{\mathrm{SDW}} + F_{\mathrm{int}} \tag{4.17}$$

where F_{CDW} is given in Eq. (4.9) and F_{SDW} is given by [90, 91]

$$F_{\mathrm{SDW}} = \int d^3x \Big\{ \frac{1}{2} K_s \left| \boldsymbol{\nabla} S_a(\boldsymbol{x}) \right|^2 + \frac{1}{2} r_s |\boldsymbol{S}(\boldsymbol{x})|^2 + u_s |\boldsymbol{S}(\boldsymbol{x})|^4 + \tilde{u}_s |\boldsymbol{S}^*(\boldsymbol{x}) \times \boldsymbol{S}(\boldsymbol{x})|^2 \Big\} \tag{4.18}$$

where $r_s = T - T_0^{\mathrm{SDW}}$, and the interaction between CDW and SDW is

$$F_{\mathrm{int}} = \int d^3x \Big\{ \lambda \psi^*(\boldsymbol{x}) \boldsymbol{S}(\boldsymbol{x}) \cdot \boldsymbol{S}(\boldsymbol{x}) \exp(i(2\boldsymbol{K} - \boldsymbol{Q}) \cdot \boldsymbol{x}) + \text{c.c.} + \gamma |\psi(\boldsymbol{x})|^2 |\boldsymbol{S}(\boldsymbol{x})|^2 \Big\}, \tag{4.19}$$

where λ is a coupling constant that describes the effects of mutual commensurability of the CDW and SDW orders. Since, in LESCO, the SDW onset temperature is much lower than the CDW onset temperature ($T^0_{\mathrm{SDW}} \ll T^0_{\mathrm{CDW}}$), we will consider the case that the CDW is well developed at the SDW onset temperature.

The ansatz now is

$$\psi(\boldsymbol{x}) = \phi_0 \exp(i 2\ell\, \hat{\boldsymbol{Q}} \cdot \boldsymbol{x}), \qquad \boldsymbol{S}(\boldsymbol{x}) = \boldsymbol{S}_0 \exp(i(\ell - q) \hat{\boldsymbol{Q}} \cdot \boldsymbol{x}) \tag{4.20}$$

where the magnitudes of the ordering wave vectors are parametrized by

$$Q_{\text{CDW}} = Q + 2\ell, \qquad K_{\text{SDW}} = K + \ell - q. \tag{4.21}$$

Here, $\delta = 2\ell$ and q measures the mutual incommensurability of the CDW and the SDW. The full free energy density for this ansatz is

$$\begin{aligned} f =& f_{\text{CDW}} + f_{\text{SDW}} + f_{\text{int}} \\ =& \frac{1}{2} K_c (2\ell - \delta_0)^2 \phi_0^2 + \frac{1}{2} \left(r_c + 2\tilde{V}_{\text{eff}}(Q_{\text{CDW}}) \right) \phi_0^2 + u_c \phi_0^4 + \frac{\kappa_0}{2} (\Delta\bar{\rho} + 2\Lambda |\phi_0|^2 \delta)^2 \\ +& \frac{1}{2} (r_s + K_s(\ell - q)^2)\ \boldsymbol{S}_0^2 + u_s\ \boldsymbol{S}_0^4 + 2\lambda \phi_0^2 \boldsymbol{S}_0^2 + \gamma \phi_0^2 \boldsymbol{S}_0^2. \end{aligned} \tag{4.22}$$

Extremizing the free energy of Eq. (4.22) with respect to ℓ, we now find

$$\ell = \frac{\delta_0}{2} \left[\frac{x^2(z-1) + 2ty^2}{x^2(z + x^2) + y^2} \right] \tag{4.23}$$

using the parametrization

$$x = \frac{\phi_0}{a}, \qquad y = \frac{S_0}{c}, \qquad t = \frac{q}{\delta_0}, \qquad c^2 = \frac{16\Lambda^2 \kappa_0}{K_s} a^4. \tag{4.24}$$

The equilibrium state is now found by finding the minimum of the free energy with respect to ϕ_0 and S_0. The free energy density of eq. (4.22) takes the form

$$f = \frac{1}{2} K_c \delta_0^2 a^2 F(x, y) \tag{4.25}$$

where

$$\begin{aligned} F(x,y) =& \left[\frac{x^2(x^2+1) - (2t-1)y^2}{x^2(x^2+z) + y^2} \right]^2 x^2 + \frac{x^2}{z} \left[\frac{z(x^2+1) + 2ty^2}{x^2(x^2+z) + y^2} \right]^2 + \mu y^2 \left[\frac{x^2(z - 1 - 2t(x^2+z)}{x^2(x^2+z) + y^2} \right]^2 \\ +& \tilde{r}_c x^2 + w_c x^4 + \tilde{r}_s y^2 + w_s y^4 + \tilde{\gamma} x^2 y^2 + \tilde{\lambda} x y^2. \end{aligned} \tag{4.26}$$

Here we used the rescaled parameters

$$\begin{aligned} \tilde{r}_c =& \frac{(r_c + 2\tilde{V}(Q)}{K_c \delta_0^2}, \qquad w_c = \frac{2a^2}{K_c \delta_0^2} u_c, \qquad \tilde{r}_s = \frac{c^2}{K_c a^2 \delta_0^2} r_s, \qquad w_s = \frac{2c^4}{K_c \delta_0^2 a} u_s \\ \tilde{\gamma} =& \frac{2c^2}{K_c \delta_0^2} \gamma, \qquad \tilde{\lambda} = \frac{4c^2}{K_c \delta_0^2 a} \lambda, \qquad \mu = \frac{1}{z} \end{aligned} \tag{4.27}$$

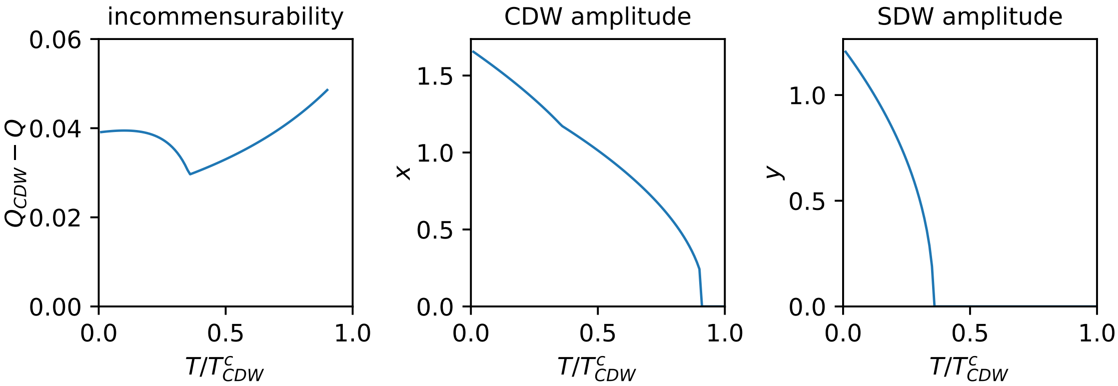

Figure 4.8: Incommensurability ℓ, CDW order parameter x and SDW order parameter y as a function of temperature for typical values of the parameters of the free energy of eq. (4.26).

Figure 4.8 shows an example of wave vector evolution of the resulting equilibrium state. Above the SDW onset temperature, Q_{CDW} shows monotonic decrease upon lowering temperature as observed in the CDW-only case in the previous section. Then a kink appears as the SDW onsets when the mutual commensurability effect begins to appear, and Q_{CDW} increases toward a state in which CDW and SDW orders mutually commensurate.

Fitting of data

We performed a fit of the incommensurability Q_{CDW} using the Landau-Ginzburg theory developed above (Fig. 4.9). The temperature dependence of the incommensurability can be fit to the model by considering the parameters in Eq. (4.27), minimizing Eq. (4.26) with respect to the rescaled order parameters x and y, and determining the ordering wavevectors via Eq. (4.21) and Eq. (4.23). Temperature dependence is contained implicitly in the parameters $\tilde{r}_c = a_c(T - T^c_{\text{CDW}})$ and $\tilde{r}_s = a_s(T - T^c_{\text{SDW}})$. Here we have introduced the parameters a_c and a_s, to convert $\tilde{r}_c$ and $\tilde{r}_s$ into Kelvin. T^c_{CDW} and T^c_{SDW} represent nominal ordering temperatures of CDW and SDW, respectively, i.e. the ordering temperatures in the absence of compressibility effects and coupling between CDW and SDW. The actual ordering temperatures, determined by minimizing Eq. (4.26), can vary slightly for the CDW transition and moderately for the SDW transition.

To reduce the number of parameters involved, we fix a few parameters as follows. Noting that the experimental data does not show a clear transition up to $\sim$ 300K, we interpret the charge ordering as having a very high mean-field transition temperature and hence fix $T^c_{\text{CDW}} = 400$K. While we do not know the actual value of the CDW transition temperature, fixing the value to 400K assures the resulting calculation is not sensitive to the exact value of the transition temperature. For the nominal SDW ordering temperature, we fix $T^c_{\text{SDW}} = 35$K to be roughly consistent with the SDW onset temperature seen in a neutron scattering measurement on LESCO $x = 0.15$ [87]. Finally, the effect of the coupling $\tilde{\gamma}$ can be mimicked by varying the magnitude of $\tilde{\lambda}$. Therefore, $\tilde{\gamma}$ is not strongly constrained and we set it to 0 for simplicity; the quality of the final fits is not affected.

The remaining parameters $Q, \delta_0, \tilde{\lambda}, z, t, a_c, a_s$ are free. We numerically optimize over the space of these parameters, minimizing $F(x, y)$ and calculating Q_{CDW} as a function of T for each parameter set, to obtain a least-squares fit to the experimental data of incommensurability (Fig. 4.10). In all cases, the fit is successful, with the statistic $\chi^2 \sim N$, where N is the number of experimental data points.

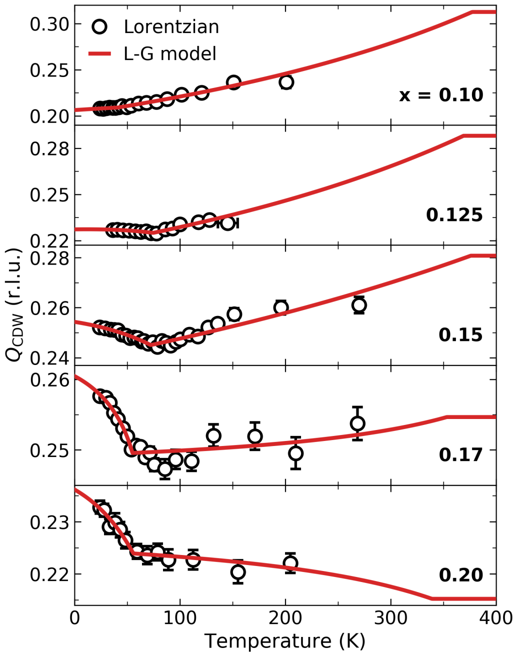

Figure 4.9: Temperature dependence of Q_{CDW} obtained from fits with a Lorentzian function (open circles) and Landau-Ginzburg theory (solid lines).

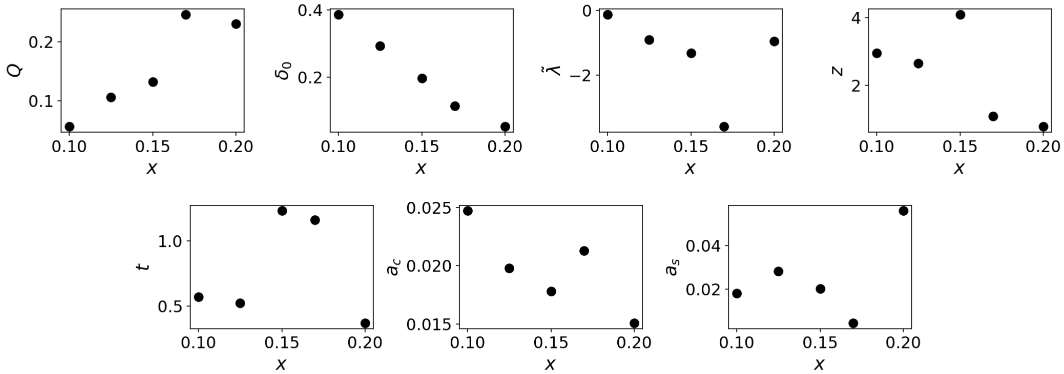

Figure 4.10: Result of fit parameters $Q, \delta_0, \tilde{\lambda}, z, t, a_c, a_s$ from fits of Q_{CDW} with the Landau-Ginzburg theory for each doping.

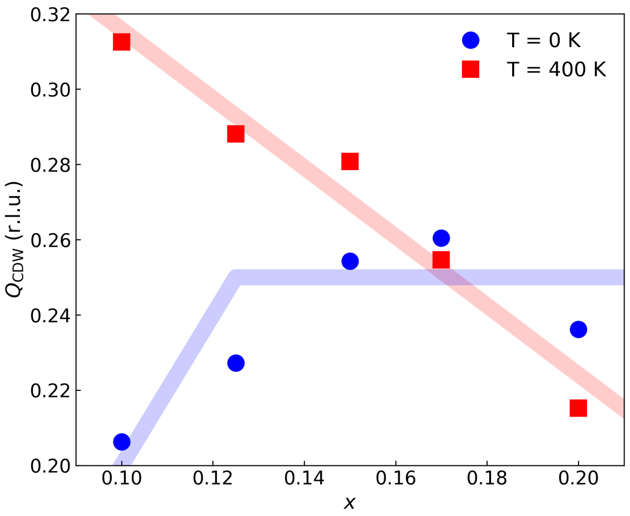

Figure 4.11: Doping dependence of Q_{CDW} at T = 0 K (blue circles) and 400 K (red squares) extrapolated by the Landau-Ginzburg model described in the text. Solid lines are guides to the eye.

4.3 Discussion

In describing the data for Q_{CDW} by the Landau-Ginzburg theory, we have incorporated our knowledge from the previous lineshape analysis, that the in-plane integrated intensity remains significant at the highest temperatures in the experiment, by assuming a very high nominal CDW transition temperature $\sim 400K$. It is therefore interesting to consider the behavior of Q_{CDW} determined by extrapolating the result of the Landau-Ginzburg theory to beyond the experimental temperatures.

Figure 4.11 shows the values of Q_{CDW} at T = 0 K and 400 K that are extrapolated from the fitting result using the Landau-Ginzburg model. The doping dependence of Q_{CDW} at $T = 0$ K follows the Yamada relationship, that is Q_{CDW} is close to twice of the doping value for $x \leq \frac{1}{8}$ and saturates at 0.25 for $x \geq \frac{1}{8}$, and this behavior can be explained as the result of the mutual commensurability effect between CDW and SDW.

Interestingly, the doping dependence at 400 K is completely different from the one at 0 K. At $T = 400$ K, Q_{CDW} is close to 0.31 at $x = 0.10$, and as the doping increases Q_{CDW} continuously decreases, reaching 0.22 at $x = 0.20$. Although the absolute values are slightly different, this trend of monotonic decrease of Q_{CDW} upon increasing doping is the behavior observed in YBCO and Bi-based compounds. This observation that the doping evolution of CDW wave vector in a La-cuprate at a high-temperature follows the same trend that is observed other cuprate families suggests that there may be a universal CDW mechanism that applies to all cuprates. The distinct low-temperature CDW property of La-cuprate may originate from the coupling of CDW with SDW, while other cuprate families do not exhibit SDW.

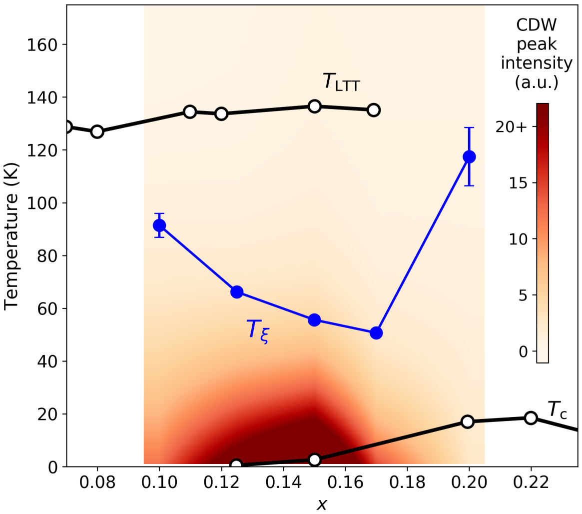

Figure 4.12: Phase diagram of $\mathrm{La}_{1.8-x}\mathrm{Eu}_{0.2}\mathrm{Sr}_x\mathrm{CuO}_4$ displaying the continuous development of CDW peak intensity and T_ξ as given in Eq. (4.29). LTT structural transition temperature T_{LTT} and superconducting transition temperature T_{c} are taken from Ref. [24].

Previous studies reported that the phase diagram of LESCO exhibits a dome-shaped phase boundary of CDW centered at $x = \frac{1}{8}$ with its onset temperature at $T \approx 80$ K [24, 44]. However, our study revealed that the in-plane integrated intensity of CDW is temperature-independent for the entire measured temperature range. The peak intensity of CDW exhibit a continuous increase upon cooling due to suppression of phase fluctuation, without any clear signature of phase transition. Thus, a onset temperature cannot be defined for such evolution of CDW and existing phase diagrams of LESCO, such as the one in Ref. [24], can be misleading about the nature of CDW in LESCO.

Instead of a onset temperature, it is possible to define a temperature scale that reflects the degree of the suppression of phase fluctuations of CDW by disorder. The lineshape of CDW is well-described by Eq. (4.1), and Eq. (4.7) governs the temperature dependence of the parameters. Eq. (4.7) can be rewritten as

$$1 = \frac{T}{4\pi\kappa/\ln\left[\frac{\Gamma}{\mu}\right]} + \frac{\sigma^2}{4\pi\kappa\mu}. \tag{4.28}$$

In the limit of $T \to 0$, the value of μ is given by $\mu_0 = \mu(T \to 0) = \frac{\sigma^2}{4\pi\kappa}$. We can define a temperature scale T_ξ as

$$1 = \frac{T}{T_\xi} + \frac{\sigma^2}{4\pi\kappa\mu}\bigg|_{T\to 0}, \quad T_\xi = 4\pi\kappa/\ln\left[\frac{\Gamma}{\mu_0}\right] = 4\pi\kappa/\ln\left[\frac{4\pi\kappa\Gamma}{\sigma^2}\right]. \tag{4.29}$$

Here, T_ξ represents a temperature scale that marks a crossover from a low temperature regime, where CDW is pinned by disorder and thermal effects are negligible, to a high temperature regime, where disorder plays a relatively smaller role and the correlations of CDW are determined by thermal fluctuations. Figure 4.12 shows the phase diagram of LESCO displaying the evolution of peak intensity and the temperature scale T_ξ. Curiously, it exhibits a local minimum around $x = 0.15{-}0.17$, unlike the local maximum of the reported onset temperature around $x = 0.125$ in LESCO [24], as well as in other materials such as $La_{2-x}Ba_xCuO_4$ [14] and $La_{2-x}Sr_xCuO_4$ [16]. In the previous reports, the onset temperatures were defined based on the temperature evolution of the peak intensity or the intensity integrated in one dimension. Our study suggests that such onset temperature alone cannot fully capture the nature of the evolution of CDW, and the effect of disorder must be taken into account.

Chapter 5

Detecting fluctuating orders in $La_{2-x}Ba_xCuO_4$ using a transition-edge sensor array detector

This chapter has been adapted from Ref. [84].

5.1 Introduction

5.1.1 CDW and subharmonic order

As discussed in the previous chapters, nearly all unconventional superconductors exhibit a CDW phase is found in the vicinity of the superconducting phase. Although there have been experimental observations that suggest a competition between CDW and superconductivity [15, 16, 32], there is growing evidence that the relationship between superconductivity and CDW order parameter is more complex than a simple competition.

In 2007, Li *et al.* discovered that LBCO $x = 1/8$ exhibits in-plane superconductivity at $T \sim 40$ K, while its three-dimensional superconducting transition appears at a much lower temperature at $T \sim 10$ K. The observation was followed by a development of a theoretical model which suggested that the CDW can be coherently coupled to the phase of the superconducting order parameter which leads to the decoupling of the CuO_2 layers at the temperature range of 10 K $\leq T \leq$ 40 K, and to the in-plane superconductivity [12,92–94]. In such state where the superconducting order parameter is coherently coupled to other orders such as CDW or SDW, the superconducting order itself will be spatially modulated. This new quantum phase of matter is named as pair density wave (PDW). Moreover, the theory predicted that in PDW phase a subharmonic component of the CDW order whose ordering wave vector is $Q_{\text{CDW}}/2$ should develop with an amplitude proportional to the uniform superconducting order parameter [12, 93, 94]. The subharmonic modulation, if one exists, should be observable in an x-ray scattering experiment, and it will provide a strong evidence of the PDW theory.

Using RSXS would certainly help the detection of the subharmonic reflection, as the technique greatly enhance the sensitivity to modulations of valence electrons. However, when an x-ray beam is tuned to resonance, it is not only the resonant scattering that is amplified but also the photoabsorption, which is the

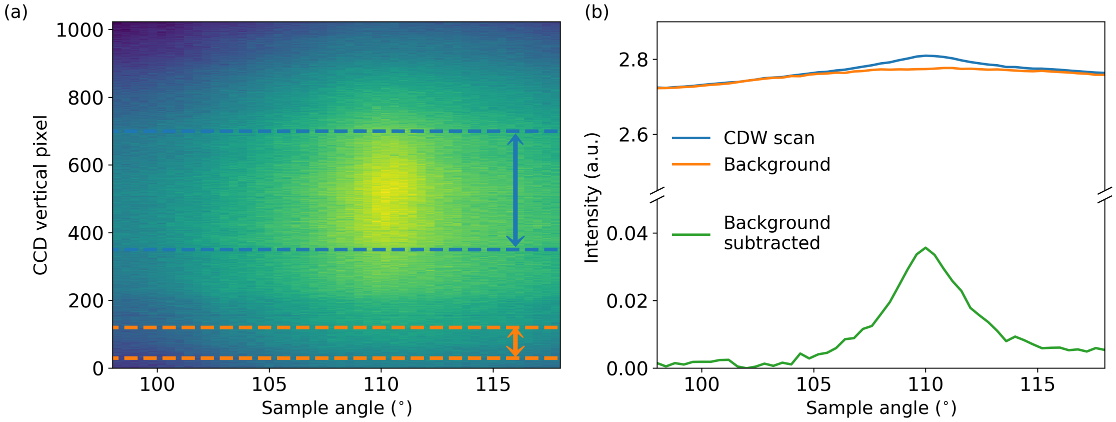

Figure 5.1: Scan of CDW in LBCO $x = 0.155$ at $T = 23$ K measured using a CCD detector at SSRL beamline 13-3. (a) Intensity map of CDW measured using a CCD. The region within the blue (orange) dashed lines captures CDW (background) signals. (b) Comparison between the energy-integrated signal of CDW scan and the background. The bump in the CDW scan above the background represent the elastic CDW signal. The background subtracted signal shows that the CDW intensity (~ 0.04) is only 1.5% of the background intensity (~ 2.75).

first step in resonant scattering. The vast majority of photoabsorbed excited states decay through radiative channels and don't contribute to coherent scattering. The size of the photoabsorption cross section in the soft x-ray regime makes core level fluorescence the dominant signal in RSXS. This inelastic background is a serious limitation on the RSXS technique, particularly when trying to detect faint signals from glassy or fluctuating order, such as the subharmonic ordering, in which the scattering structure factor is spread over momentum space in a diffuse manner.

To illustrate the problem, a measurement of CDW in $La_{1.845}Ba_{0.155}CuO_4$, which is an candidate material to exhibit a PDW state, is performed using a CCD detector at SSRL beamline 13-3. The CCD detector is an energy-integrating detector and cannot discriminate the elastic CDW signal from the inelastic fluorescence background. Exploiting its large detection area, the profile of background without CDW signal can be measured as discussed in Section 2.3.4. The elastic CDW signal can be estimated by subtracting the background intensity from the energy-integrated scan. Figure 5.1(b) shows the result of the background subtraction that the elastic CDW signal is only 1.5% of the background intensity. If a subharmonic order exists in this material, it is expected to be fluctuating, having a shorter correlation length compared to the CDW. In order to detect such weak and diffused signals, it is crucial to discriminate elastic signals from background signals precisely, and a possible solution is to use a detector with an energy-resolving capability and a high detection efficiency.

5.1.2 Transition-edge sensor array detector

Transition-edge sensors (TES) are highly sensitive energy-resolving photon detectors exploiting a sharp superconducting-to-normal transition of a superconducting thin film. TES detectors have been used for many applications including x-ray emission spectroscopy [95–97], time resolved x-ray absorption spectroscopy [98], and cosmic microwave background surveys [99, 100]. Thanks to recent advancements in their performance and usability, such detectors have begun to be adopted at large-scale x-ray facilities [83, 101]. State of the art TES array detectors offer superior energy resolution to solid state detectors (about 1.5 eV FWHM at 900 eV), excellent quantum efficiency, and solid angle coverage similar to spectrometers based on diffraction gratings [83]. Moreover, modern TES instruments comprise hundreds of such sensors, each of which acts as an independent, energy-resolving spectrometer. This significantly boosts the data collection rate by allowing parallel studies of multiple reciprocal space points.

TESs operate in an electrothermal steady state in contact with a cryogenic heat bath and in constant voltage bias, which puts the TES at its superconducting transition. When an x-ray impinges on a TES, its temperature and, in turn, resistance increase through a continuous superconducting-to-normal transition. Consequently, the current through the TES temporarily drops. Shortly after, it recovers to its quiescent level aided by negative electrothermal feedback. This transient current drop is measured by a SQUID readout system through mutual inductance. The magnitude of the current pulse is roughly proportional to the energy of the x-ray.

Johnson noise and thermal fluctuation between a TES and the heat bath are the dominant limiting factors determining the energy resolution [99]. The resolution of a TES depends on its heat capacity, C, and is approximately given by

$$\Delta E \sim \sqrt{k_{\mathrm{B}} T_{\mathrm{op}}^2 C / \alpha_I} \tag{5.1}$$

where $\alpha_I = (T_{\mathrm{op}}/R_{\mathrm{op}})\, \partial R/\partial T|_{I_{\mathrm{op}}}$, $T_{\mathrm{op}} = 107$ mK is the operating temperature of the TES, R_{op} is its resistance in its quiescent state, and the derivative of the resistance curve, $R(T)$, is evaluated at T_{op} and at the bias current, I_{op}.

The TES detector used in this study was built by the Quantum Sensors Group at NIST (Boulder, CO, USA) [83]. The detector was first installed and operated at the APS beamline 29 from 2014 to 2017, and then relocated to SSRL beamline 13-3 in 2018. The detector consists of an array of 240 sensors (Fig. 5.2(a)). The sensor array is maintained at a bath temperature of 70 mK via an adiabatic demagnetization refrigerator (ADR) and is mounted on the end of a long snout so it can be positioned near the sample in the sample chamber used for RSXS experiments (Fig. 5.2(b)). The quantum efficiency of the TES detector is limited

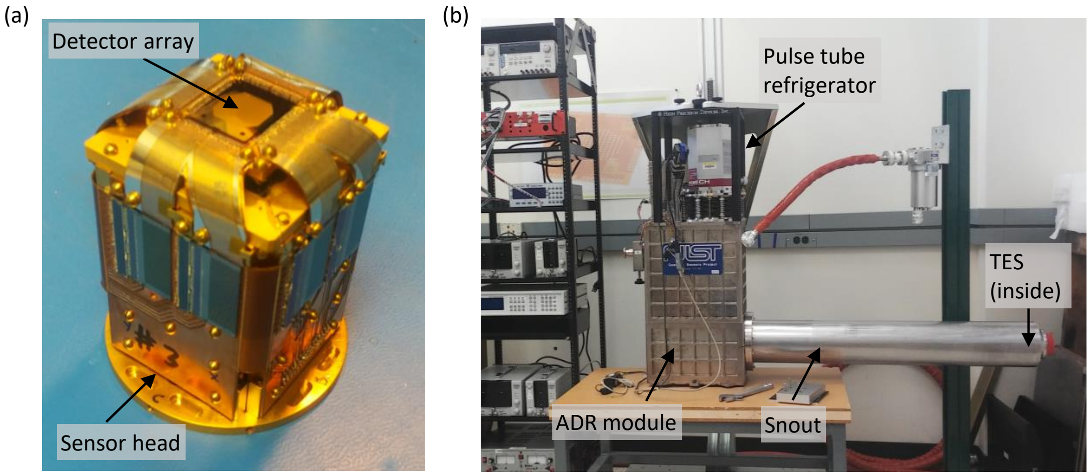

Figure 5.2: (a) Picture of a TES module. (b) Picture of a TES detector setup with a snout and a cryogenic system. Pictures are taken when the detector was at NIST for refurbishing, before being installed at SSRL beamline 13-3.

by transmission through a series of vacuum and radiation windows, and is about 24% at the O K edge and 57% at the Cu $L_{3/2}$ edge [83].

5.2 Results

5.2.1 Proof of concept: $La_{1.875}Ba_{0.125}CuO_4$ as a test case

To demonstrate the background rejection capabilities of a TES detector and quantify the advantages of introducing energy discrimination, RSXS measurements were performed on CDW in LBCO $x = 0.125$, a prototypical high T_c cuprate exhibiting long-ranged CDW. The experiments were carried out at the RSXS endstation of the APS beamline 29. The TES detector was mounted on the RSXS chamber on a fixed port at a scattering angle of approximately $2\theta = 125°$. Out of 240 sensors, a 24-sensor subsector of the TES was used to illustrate the advantages of multiplexing while operating close to the optimal resolution. A single crystal of LBCO $x = 0.125$ used in this study was grown using floating-zone method by Genda Gu at Brookhaven national laboratory.

The energy resolution of the TES detector was determined by measuring diffuse elastic scattering from a thin layer of gold on polished silicon, as illustrated in Fig. 5.3(a). The energy bandwidth of the elastic scattering is the same as that of the incident beam, which was about 0.1 eV. Since the resolution of TES is significantly larger than the elastic energy bandwidth, the observed spectrum is an excellent measure of the intrinsic resolution of the TES. The FWHM resolution varied slightly among different sensors but was

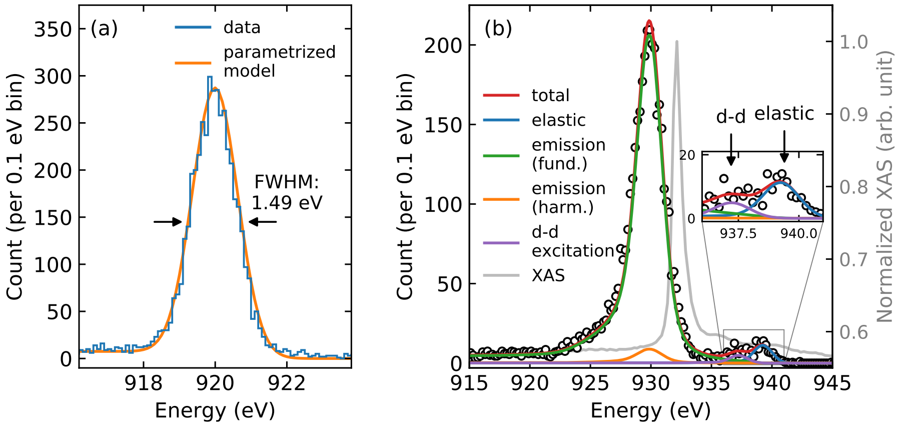

Figure 5.3: (a) Resolution function of the TES (blue curve) determined from diffuse elastic scattering from a thin layer of gold on polished silicon at a fixed incident beam energy of 920 eV. (orange curve) Fit function used in analysis of the data. (b) LBCO spectrum taken with sensor #15 far from the CDW Bragg condition showing elastic, *d*-*d*, and fluorescence emission features in the data. The colored lines represent the different components of the fit model (see text). The spectrum is measured at a fixed incident beam energy of 938.9 eV. Cu $L_{3/2}$ XAS spectrum of LBCO showing the absorption maximum. The XAS curve is plotted against incident photon energy while the other curves are plotted against scattered photon energy.

approximately $\Delta E = 1.5$ eV (Fig. 5.3(a)).

A representative TES spectrum illustrating the basic features of the data is shown in Fig. 5.3(b). This histogram shows the number of photon events detected by sensor #15 at an incident beam energy of 938.9 eV for an integration time of 2 min, as a function of detected photon energy. For comparison, plotted together is the Cu $L_{3/2}$ x-ray absorption spectrum (XAS) taken in total electron yield mode from the LBCO sample. This spectrum is plotted against incident photon energy and shows that the absorption maximum occurs at 932.2 eV.

While the 1.5 eV energy resolution is modest, the expected features in the spectra are clearly visible, including the elastic scattering, *d*-*d* excitations which are offset from the elastic peak by about 2 eV, and an incoherent emission peak at 930 eV that dominates the overall signal. The *d*-*d* excitations are actually a coherent inelastic scattering effect, making Fig. 5.3(b) an example of a valence band resonant inelastic x-ray scattering (RIXS) spectrum taken using the intrinsic energy resolution of a solid state detector. Note that the incident beam is highly detuned from the absorption maximum at 932.2 eV. That the *d*-*d* excitations are nevertheless visible is a demonstration of the high sensitivity of the TES detector.

The incident energy dependence of the CDW scattering, as observed with the TES array, is summarized in Fig. 5.4, which shows the measured intensity as a function of both incident and detected photon energy on a color plot for each of the 24 active sensors. The sample angle was adjusted in coordination with the incident energy to keep the in-plane component of the momentum transfer fixed, with sensor #25 aligned to

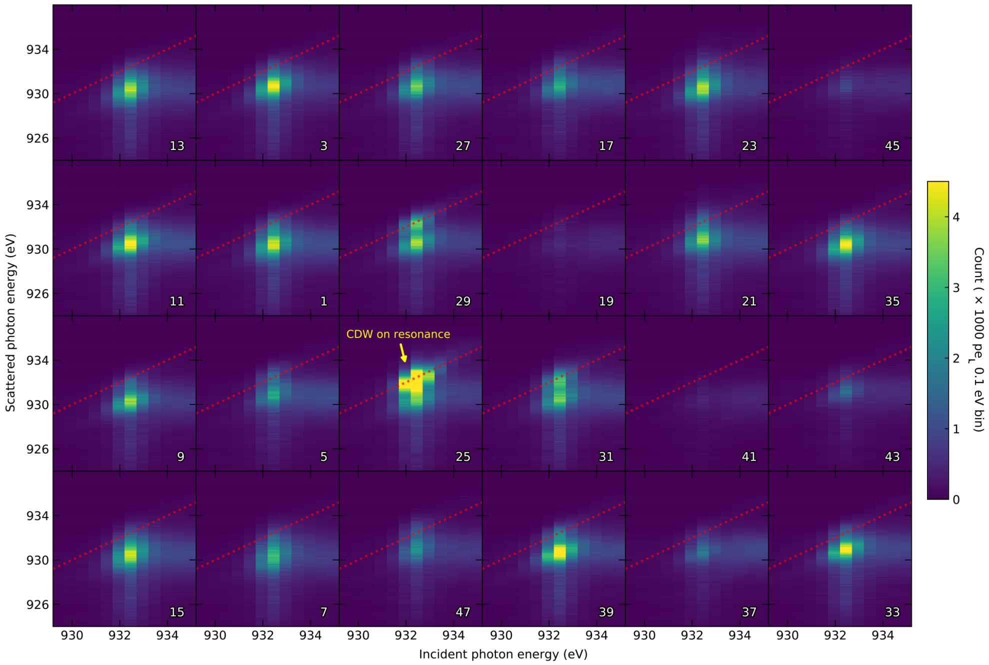

Figure 5.4: Incident energy dependence of the scattered intensity from LBCO as measured by the 24 active sensors in the TES array. The incident photon energy was tuned from 929.2 eV to 935.8 eV in 0.5 eV steps. The sample angle was changed from 35.1° to 35.3°, in coordination with the incident beam energy, to keep the in-plane component of the momentum transfer fixed during the scan. The CDW signal is observed in sensor #25 whose location corresponds to a momentum vector $\mathbf{q} = (0.23, 0, 1.54)$. The red lines indicate the location of the elastic scattering ($\omega_i = \omega_s$).

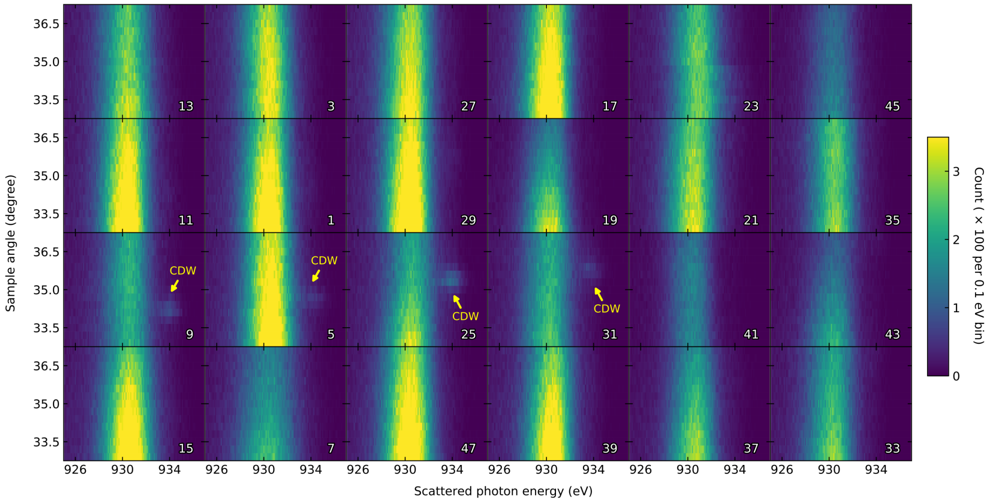

Figure 5.5: Sample angle dependence of the scattered intensity from LBCO. This data set is essentially a scan of the momentum transfer vector of each of the 24 active sensors of the TES detector. The CDW is visible as a peak at the scattered energy of 933.7 eV which corresponds to the incident beam energy. The CDW sweeps across sensors 9, 5, 25, and 31.

a momentum of (0.23, 0, 1.54) to detect diffraction from the CDW. The integration time for each distinct incident energy was 5 min. The incident photon energy was stepped in 0.5 eV increments through the Cu $L_{3/2}$ edge at 932.2 eV, which corresponds to electric-dipole transitions into the $3d$ shell, enhancing sensitivity to valence band order [25].

Fig. 5.4 demonstrates a few important general features of resonant scattering that illustrate how to best use a TES detector for RSXS experiments. Below resonance, photoabsorption from Cu $2p \rightarrow 3d$ transitions is not allowed. However, resonant scattering–both elastic and inelastic–can still take place. The scattering will be "off-shell," meaning whatever energy denominators are present in the cross section are not perfectly minimized, but resonant scattering can still take place albeit with somewhat reduced intensity. The elastic scattering, which is the signal of interest here, shows up on the diagonals in each panel in Fig. 5.4 (red lines). When the incident beam energy is above the resonance, the Cu^{2+} fluorescence line becomes strong and sits at fixed emitted photon energy [102]. At the incident x-ray beam energy of 932.2 eV, which corresponds to the resonance maximum, the intensity of both the elastic scattering and the x-ray fluorescence is maximized. However, the different spectral components are intermixed and cannot be resolved using the 1.5 eV resolution of the TES. Optimal background rejection therefore requires slight detuning of the energy from the resonance. For this reason, studies of the charge order were carried out at an incident beam energy of 933.7 eV at which the scattering retains a considerable amount of the resonant enhancement and the elastic component is energetically resolvable using the resolution of the TES.

Having chosen an incident beam energy, we performed momentum scans through the charge order peak by rotating the θ angle of the sample, in 0.1° increments, at fixed incident energy (Fig. 5.5). In this scan the CDW sweeps across sensors #9, #5, #25, and #31, in which it is clearly visible as a peak at 933.7 eV that is resolvable from the fluorescence line at 930.1 eV. The data in Fig. 5.5 contain enough information to determine a quantitative, energy-resolved elastic lineshape of the CDW, which should be superior to what was possible in early studies [25]. However, doing so requires some means to extract the coherent elastic signal from the data.

The individual spectra [Fig. 5.3(b)] consist of three main features: (1) the elastic line itself, which is resolution-limited and always resides in the spectrum at the incident beam energy, (2) the d-d excitations, which reside $\sim$2 eV below the elastic line and are also resolution limited, and (3) the fluorescence line, which is the primary source of background. As shown in Fig. 5.4, the behavior of the fluorescence feature is complicated, evolving from a Raman-like excitation to an incoherent emission feature at 930 eV as the beam energy is tuned through the resonance [102]. A detailed spectroscopic model of these features is needed to quantify the amount of elastic scattering in the spectra. This model should properly account for the finite

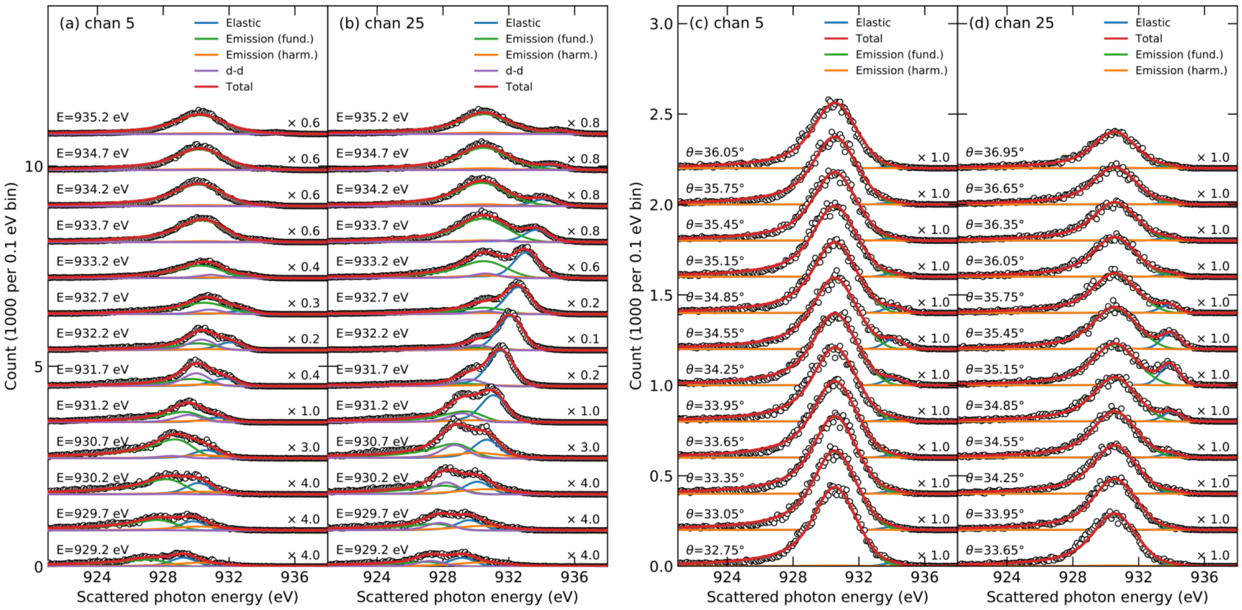

Figure 5.6: Application of the fit model to the TES spectra from sensors #5 and #25. Each curve represents a cut as a function of scattered photon energy through panels #5 and #25 in Figs. 5.4 and 5.5. Some of the spectra have been scaled for visibility. (a), (b) Individual TES spectra for various incident beam energies. Solid lines show different terms in the fit model and open circles are the experimental data points. At each incident beam energy the sample angle is changed in a coordinated way to keep the momentum transfer vector fixed. (c), (d) Individual TES spectra for various sample angles. The angle-dependent spectra were taken at a fixed incident energy of 933.7 eV.

detector resolution, which is similar to the separation between the elastic and fluorescence features in most of the data, by convolving with the response curve in Fig. 5.3(a).

The elastic scattering and *d*-*d* excitations are both resolution-limited. We therefore model both as Dirac delta functions, which will broaden into replicas of the resolution function of the instrument when convolved with the response curve [Fig. 5.3(a)]. To model the fluorescence feature, we apply a modified version of the Eisenberger-Platzman-Winick (EPW) model of x-ray emission [84].

A least-squares fit of this model to a sample spectrum, properly convolving the resolution function of the detector, is shown in Fig. 5.3(b). The quality of the fit is reasonable and accounts for all the primary spectral features. A small amount of fluorescence is present even when the x-ray energy is below the edge because of second harmonic contamination in the x-ray beam, i.e., photons with double the nominal energy. This extra component was explicitly included in the fit [Fig. 5.3(b), orange curve].

We now use this model to extract the elastic counts from sensors #25 and #5, which correspond to the integrated intensity of the elastic feature at the peak of the CDW reflection and a location on its tail, respectively. The result of the fits to the individual curves is shown in line plots in Fig. 5.6. The model allows each spectrum to be decomposed into discrete components, the counts being assigned to bins corresponding to d-d, fluorescence, and the elastic counts of interest.

We are keenly interested in how the statistical quality of RSXS data is improved by introducing energy resolution into the measurement. The two values of interest are the elastic counts, N_{elastic}, and the total photon counts, N_{total}. N_{total} is the energy-integrated total counts collected by a TES sensor, and represents how a given measurement would look had it been done with an energy-integrating detector of the same quantum efficiency under the same conditions.

We assigned error values to the elastic counts in each spectrum by taking the square root of the corresponding diagonal value of the variance-covariance matrix of fit parameters [103]. This error value obtained in this manner, $\Delta N_{\text{elastic}}$, accounts for statistical error as well as systematic error resulting from imperfection of the fit model. If the model were perfect, the error would reduce to the Poisson result, $\Delta N_{\text{elastic}} = \sqrt{N_{\text{elastic}}}$. In practice, we expect the error to exceed the Poisson value since the model will not fit the spectrum perfectly. The error in the energy-integrated counts is determined purely by Poisson counting statistics, $\Delta N_{\text{total}} = \sqrt{N_{\text{total}}}$.

The attribute of a TES detector that provides a performance increase for RSXS measurements is its ability to separate out the elastic counts, N_{elastic}, from all the photon events, $N_{\text{total}} = N_{\text{elastic}} + N_{\text{background}}$. The noise level, which in all cases is limited by Poisson counting statistics, is $\sqrt{N_{\text{elastic}}}$ for the former quantity and $\sqrt{N_{\text{total}}}$ for the latter. The TES therefore provides a significant reduction in noise and improvement in data quality, even in cases where the average background is known. The TES is particularly effective when the elastic signal is weak and the background level is high.

The results of the fits in Fig. 5.6 are summarized Fig. 5.7, which shows the elastic counts, N_{elastic}, for sensors #5 and #25 plotted against energy and angle. The error bars in Fig. 5.7 represent $\pm\Delta N_{\text{elastic}}$. For comparison, on the same plots we show the energy-integrated counts, N_{total}, with the error bars corresponding to $\pm\Delta N_{\text{total}} = \pm\sqrt{N_{\text{total}}}$.

Focusing first on the energy spectrum from sensor #25 (Fig. 5.7(b)), the elastic curve differs from the energy-integrated curve in that the edge jump, seen as an increased intensity for energies greater than about 934 eV, is absent. This indicates that there is enhanced fluorescence background when the energy is tuned far above the edge, but there is little enhancement of the resonant elastic scattering there. In other words, the apparent jump is entirely due to background fluorescence, and is not a property of the RSXS signal itself.

A dramatic difference is seen in the angle scans through the CDW peak. Had the measurement been done with an energy-integrating detector, it would have resembled Fig. 5.7(d), which shows a CDW peak with a background similar to past studies [25]. Using the fit model to extract the elastic scattering results in

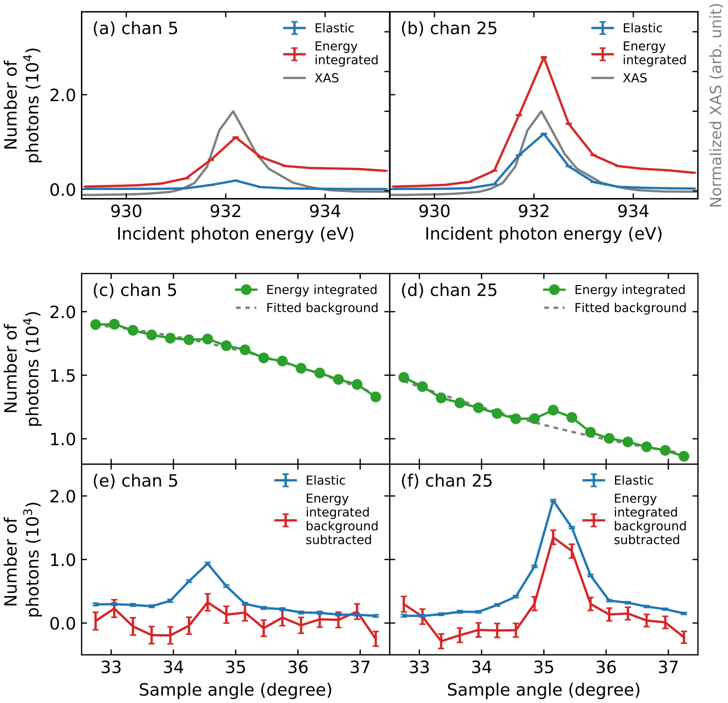

Figure 5.7: Incident energy and angle dependence of the elastic scattering, as determined by the data fits in Fig. 5.6, compared to what would have been measured with an equivalent, energy-integrating detector (energy-integrated curves have been scaled to allow visual comparison). (a) Energy dependence of the elastic CDW scattering in sensor #5 (blue) compared to the energy-integrated result (red). The XAS spectrum is displayed for comparison. (b) Same plot as panel (a) for sensor #25. (c) Angle-dependence of the energy-integrated CDW scattering in sensor #5. The CDW peak is barely visible above the fluorescence background. (d) Same plot as panel (c) for sensor #25. (e) Angle-dependence of the elastic CDW scattering in sensor #5 (blue) compared to the energy-integrated result (red). The background was removed from the energy-integrated data by subtracting a second order polynomial fit, allowing a direct visual comparison between the points. (f) Same plot as panel (e) for sensor #25.

the curve shown in Fig. 5.7(f), which is plotted next to the energy-integrated spectrum with a background line subtracted. The curves in Fig. 5.7(f) differ in two important respects. First, the noise level in the elastic curve is lower. Second, the elastic curve does not go to zero when the crystal is rotated far from the Bragg condition (see, for example, the value at $\theta = 33°$). This indicates that the elastic scattering peak has long tails, which cannot be detected without an energy-resolving detector. These tails could be a property of the CDW, or they could arise from some other effect, such as a rough sample surface. Using an energy-resolving TES detector opens up the possibility of studying these tails and determining their physical origin.

We turn now to sensor #5, which only detects a distant tail of the CDW so is a good test case for how the TES performs when applied to weak signals. The result of the energy spectrum [Fig. 5.7(a)] is similar to sensor #25, with the edge jump being eliminated. The angle scans, however, show a qualitative difference:

While the CDW peak is hardly visible above the noise level in the energy-integrated curve [Figs. 5.7(c), (e)], the elastic spectrum shows a well-defined peak with a width similar to what was observed in sensor #25. In this case the ability to see the CDW peak at all requires an energy-resolved detector. Evidently the performance advantages of a TES are particularly significant for weak signals that are at or below the noise level of the fluorescence background.

We are now in a position to make a quantitative statement about the advantage of introducing modest energy resolution into RSXS experiments. We focus on four data points in Fig. 5.7 corresponding to the peak in sensor #5 ($\theta = 34.55°$) , a location on the tail in the same curve ($\theta = 36.35°$), the peak in sensor #25 ($\theta = 35.15°$), and a location in its tail ($\theta = 36.35°$). At these points we compare the magnitudes of the elastic counts, N_{elastic}, the energy-integrated counts, N_{total}, and the error values on these quantities, $\Delta N_{\text{elastic}}$ and ΔN_{total}. N_{total} represents the value after having subtracted a background line, as illustrated in Fig. 5.7(e),(f).

We begin our comparison with the peak count rate in sensor #25. A useful figure of merit is the quality ratio, $N/\Delta N$, which would reduce to the signal-to-noise ratio in cases where ΔN is limited by counting statistics. For the energy-integrated measurement, $N_{\text{total}}/\Delta N_{\text{total}}$=12.1. For the elastic case, this ratio $N_{\text{elastic}}/\Delta N_{\text{elastic}}$=75.2. We conclude that using energy analysis provides a factor of 6 improvement in data quality in this case.

Turning now to the peak in sensor #5, the relevant ratios are $N_{\text{total}}/\Delta N_{\text{total}} = 2.4$ and $N_{\text{elastic}}/\Delta N_{\text{elastic}} = 24.5$. In this case adding energy resolution results in a factor of 10 improvement in signal quality. This seems consistent with the qualitative observation that, while a peak is hardly visible in the energy-integrated measurement, it is clearly visible in the energy-resolved curve [Fig. 5.7(e)]. This result illustrates an important point about the applicability of TES detectors in scattering: the performance improvement is higher when studying weak signals that lie at or below the noise level from the fluorescence background.

This point is further validated by examining the tails of the peak. In the case of sensor #25, the ratios are $N_{\text{total}}/\Delta N_{\text{total}}$=1.5 and $N_{\text{elastic}}/\Delta N_{\text{elastic}}$=12.6, implying a performance enhancement of 8.4. For the case of #5, we have $N_{\text{total}}/\Delta N_{\text{total}}$=0.47 and $N_{\text{elastic}}/\Delta N_{\text{elastic}}$=3.2, implying a performance improvement of 7.0.

These numbers represent the enhancement in performance *purely* from the introduction of moderate energy resolution in RSXS studies. An explicit performance comparison between a TES and a specific detector would also require accounting for quantum efficiency, solid angle coverage, number of pixels or sensors in the device, etc. Nevertheless, it is clear that, all other things being equal, introducing even modest energy resolution can improve RSXS studies by an order of magnitude.

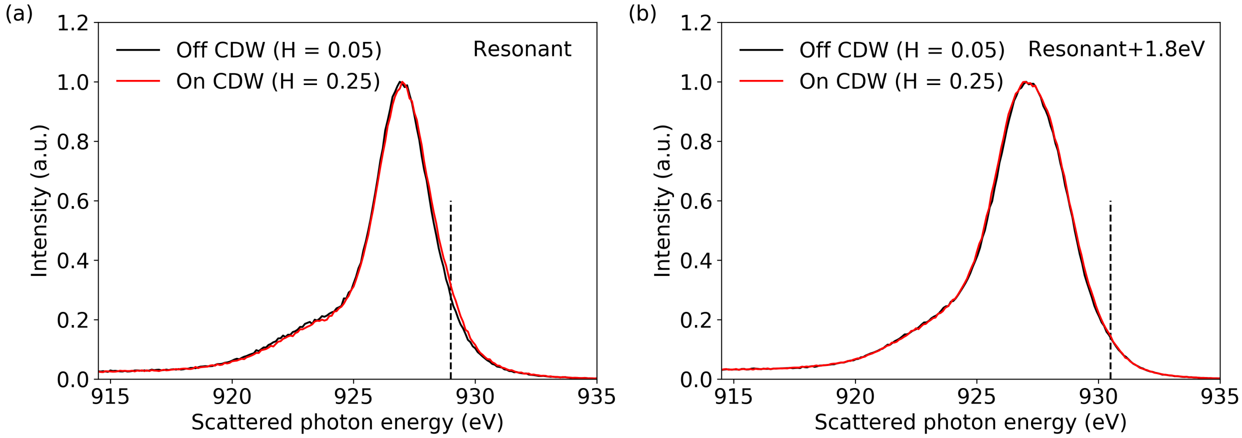

Figure 5.8: Spectra of LBCO $x = 0.155$ at $T = 23$ K ,with the incident beam energy of (a) 929 eV, the Cu L_3 edge resonant condition, and (b) 930.8 eV, 1.8 eV above the resonant condition at two momenta: $H = 0.25$ which is at the CDW peak, and $H = 0.05$, off from the CDW peak. Dashed lines indicate the elastic energy (same as the incident beam energy).

5.2.2 Preliminary results on $\mathrm{La}_{1.845}\mathrm{Ba}_{0.155}\mathrm{CuO}_4$

After we confirmed the benefit of using a TES detector for detecting fluctuating orders, we studied CDW in a optimally-doped LBCO at $x = 0.155$ and looked for possible subharmonic order. LBCO is a system that exhibits charge and spin stripe orders that coexist with superconductivity [14] and considered as a candidate material for showing PDW and, thus, subharmonic charge order reflections in x-ray experiments. Considering that the base temperature of soft x-ray scattering instruments is typically above 15 K, we chose to study a sample with $x = 0.155$ as it shows the highest T_c of 30 K, making it possible to study CDW in the presence of coexisting superconductivity. The experiments were performed at the SSRL beamline 13-3 and the base temperature was 23 K. The TES detector was relocated from the APS beamline 29 and installed at a fixed port at a scattering angle of $2\theta = 150°$. The entire array of 240 sensors were used to enhance the statistics of signals accumulated, but with a slightly compromised energy resolution of $\Delta E \approx 1.8eV$. A single crystal of LBCO $x = 0.155$ was grown using floating-zone method by Genda Gu at Brookhaven national laboratory.

We first started with measuring the CDW spectra using the TES detector at the Cu L_3 edge (Fig. 5.8). Two incident beam energies were used: 929 eV, the Cu L_3 resonant condition, to maximize the CDW signal and 930.8 eV, 1.8 eV above the resonant condition, to make the elastic component better resolvable from the inelastic components. However, unlike the case of LBCO $x = 0.125$ presented in the previous section, the elastic CDW signal was hardly identified from the spectra, presumably due to its fluctuating nature leading to a weak intensity of CDW. Although a small difference between the on- and off-CDW spectra was

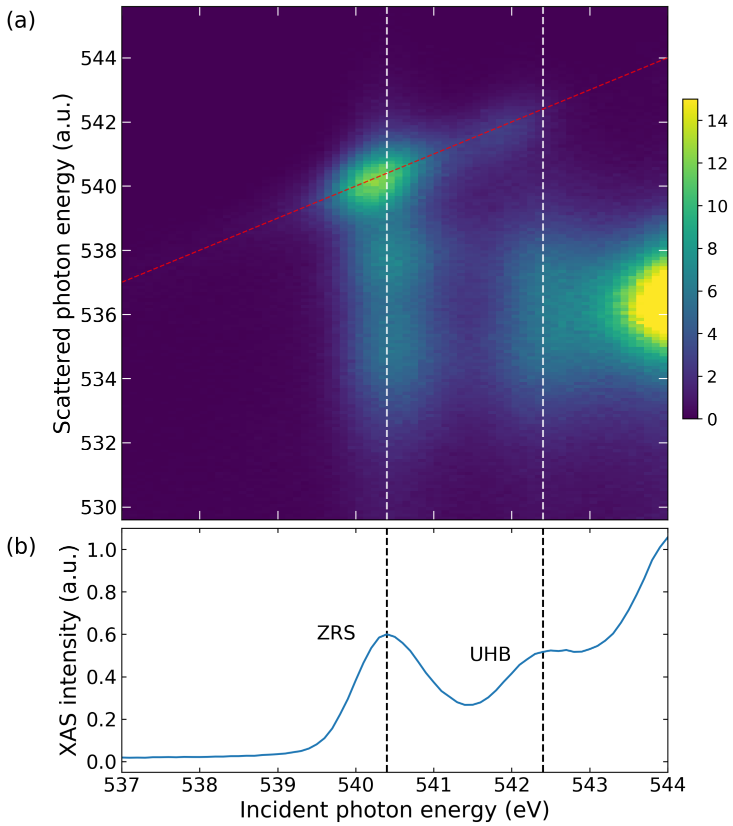

Figure 5.9: (a) Incident beam energy dependence of spectra of CDW in LBCO $x = 0.125$ at $T = 26$ K. The incident beam energy was tuned from 537 eV to 544 eV, which covers the pre-edge region of the O K edge. The red dashed line indicates the location of the elastic scattering. (b) XAS of LBCO $x = 0.125$ measured in TFY mode in the same incident beam energy range of (a). The vertical dashed lines indicate the energy of two pre-edge peaks, ZRS peak at 540.4 eV and UHB peak at 542.4 eV.

observable at the elastic energy when the beam energy was tuned at the resonant condition [Fig. 5.8(a)], the elastic component could not be clearly resolved, since other inelastic components are intermixed together. When the beam energy was detuned from the resonant condition by 1.8 eV, the spectra at on- and off-CDW locations were almost identical.

Since the experiments at the Cu L_3 edge could not successfully resolve the elastic CDW signal, we next used O K edge resonant scattering to perform experiments. In order to characterize the features of spectra at O K edge, we measured the CDW reflection in LBCO $x = 0.125$ whose signal is strong enough, making it appropriate to be a reference. Figure 5.9(a) shows the incident beam energy dependence of spectra of CDW in LBCO $x = 0.125$ at the O K edge. The elastic CDW signal (red dashed line in Fig. 5.9(a)) exhibits a strong resonance at the incident energy of 540.4 eV that corresponds to the lower-energy pre-edge peak (Zhang-Rice singlet state, ZRS) in the XAS spectrum [Fig. 5.9(b)].

Using the incident beam tuned at the resonant energy of 540.4 eV, we performed a momentum scan by

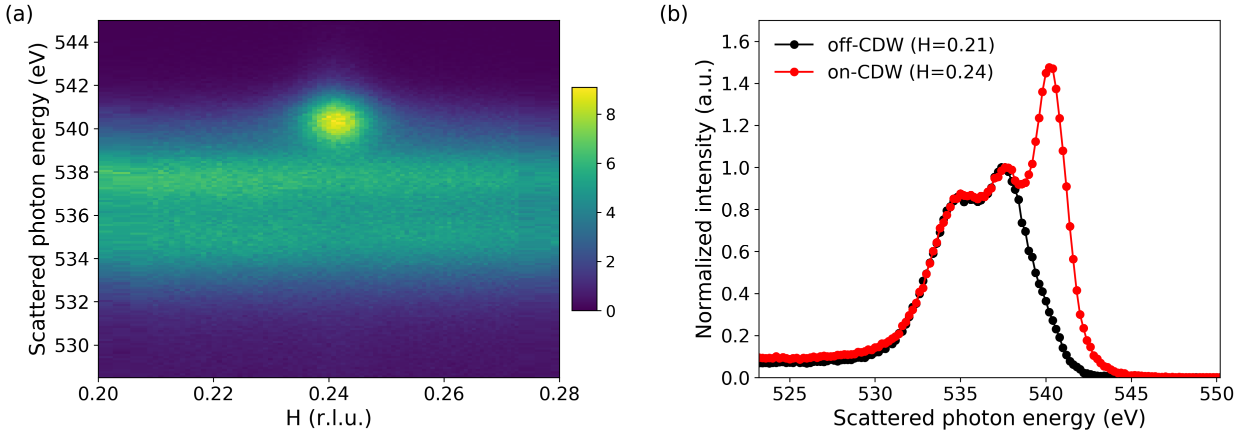

Figure 5.10: (a) Momentum dependence of spectra of CDW in LBCO $x = 0.125$ at $T = 26$ K using the incident beam energy of 540.4 eV. The elastic CDW peak is shown as a bright spot at $H \sim 0.24$, $E = 540.4$ eV. (b) Spectra at two momenta: $H = 0.24$ which is at the CDW peak, and $H = 0.21$, off from the CDW peak. The strong signal at 540.4 eV in the on-CDW spectrum is the elastic CDW component.

rotating the sample angle. As shown in Fig. 5.10(a), the elastic CDW peak appears at $H = 0.24$ at the scattered photon energy of 540.4 eV, and the inelastic features does not show any momentum dependence. Figure 5.10(b) shows the spectra at on- and off-CDW location. The on-CDW spectrum shows the elastic CDW component at 540.4 eV, and the inelastic feature exhibits two peaks at 535 eV and 537.5 eV. In the case of the spectrum at the Cu L_3 edge, the main limiting factor in resolving an elastic component was the *d*-*d* excitation peak that is located at 1.5 - 2 eV below the elastic energy. At the O K edge, as shown in Fig. 5.10(b), the strong inelastic components are located below 3 eV from the elastic energy. Considering the modest energy resolution of the TES detector, the larger separation of the inelastic fluorescence could make it easier to resolve the elastic component from the O K edge resonant scattering spectrum. However, the lack of a theoretical model of the fluorescence lineshape and the small Ewald sphere due to its low incident energy are the shortcomings of the O K edge, when compared to the Cu L_3 edge.

Having established the feasibility of the O K edge RSXS, we proceeded to look for the CDW and the subharmonic order in LBCO $x = 0.155$ by lowering the temperature below $T_\mathrm{c} = 30$ K. Figure 5.11(a) shows the intensity map of momentum - scattered energy. Unlike the case of LBCO $x = 0.125$ [Fig. 5.10(a)], the presence of CDW reflection is not clearly observable from the map. The CDW intensity is spread out over a wide range of momenta, which represents the fluctuating nature of CDW in LBCO $x = 0.155$. For a detailed analysis of the data, we compared the spectra at the CDW location ($H = 0.25$) and at the location far away from the CDW ($H = 0.07$) [5.11(b)]. When normalized to the intensity of the inelastic peak at 537 eV, the on-CDW spectrum showed a higher intensity around the elastic energy that corresponds to the elastic scattering from the CDW. For the case of the spectra at Cu L_3 edge, as seen in the previous section,

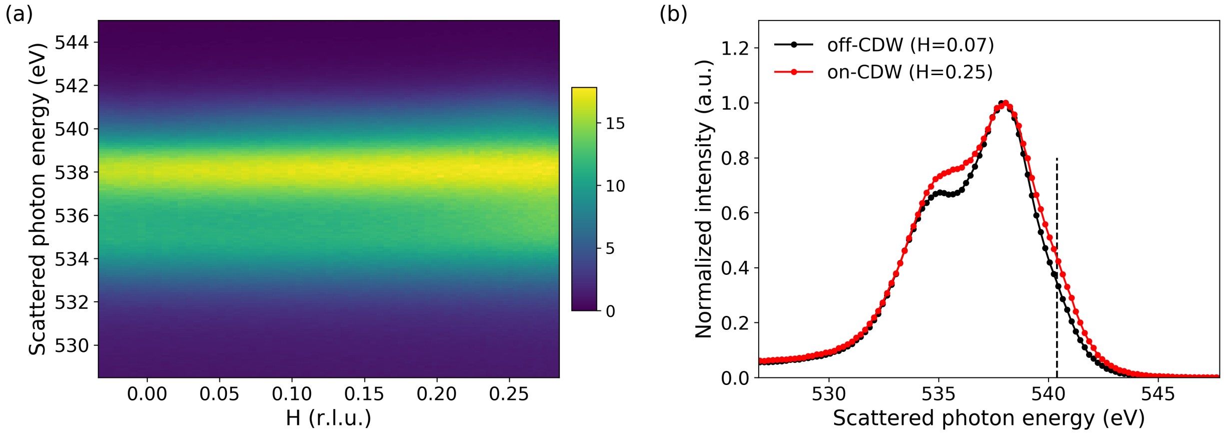

Figure 5.11: (a) Momentum dependence of spectra of CDW in LBCO $x = 0.155$ at $T = 22.5$ K using the incident beam energy of 540.4 eV. (b) Spectra at two momenta: $H = 0.25$ which is at the CDW peak, and $H = 0.07$, off from the CDW peak. Dashed line indicates the elastic energy.

the elastic component could be resolved by fitting the spectrum with a theoretical model that describes the lineshape of the inelastic components. However, unfortunately, such model is not available for the spectra at O K edge, and the elastic component could not be precisely resolved by a fitting. Instead, as an approximation, we obtained the intensity of the elastic component by integrating a spectrum over the range of ±1 eV from the elastic energy, from 539.4 eV to 541.4 eV. By performing the integration for each spectrum of the momentum scan, we obtained the elastic intensity at each momentum location. The scan range was limited up to $H = 0.284$ at which the scattering geometry was with a grazing incidence angle to the sample surface, and at higher momenta, at which the geometry is with a more grazing angle, the beam did not hit the sample properly due to a slight misalignment of the sample to the beam.

Figure 5.12 shows the temperature dependence of momentum scans of elastic intensity for a wide range of momenta that covers the CDW ($H = 0.25$) and the expected subharmonic order ($H = 0.125$) locations. The intensity of the CDW peak continuously decreases upon warming and the scans flattens out above $T = 180$ K. Previous hard x-ray diffraction studies reported that the CDW in LBCO $x = 0.155$ onsets at $T = 40$ K [14]. However, we observed that the peak persists up to $T = 150$ K, which is much higher than the reported onset temperature, and the development of the peak does not show a clear onset. This phenomenon of a continuous development of CDW starting at a high temperature is similar to what is observed in LESCO (Chapter 4), and the disorder-induced phase fluctuation may be playing an important role in LBCO as well.

Although it was anticipated, we did not observe any signature of a subharmonic order reflection at $H = 0.125$ in the scans taken at temperatures below $T_\mathrm{c} = 30$ K. This result does not prove that subharmonic order does not exist. It only means that, if such order exists, our experimental scheme was not sensitive

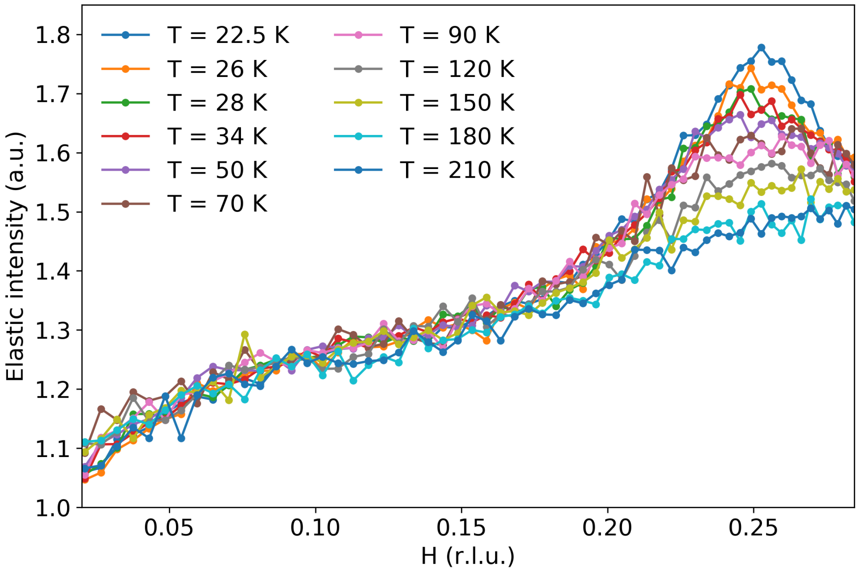

Figure 5.12: Temperature dependence of momentum scans for the range covering the CDW ($H = 0.25$) and the expected subharmonic order ($H = 0.125$) locations. The elastic intensities are obtained by integrating intensities over the energy range of 539.4 eV to 541.4 eV from each spectra.

enough to detect a signal from the order. A few ways to improve the sensitivity would include developing a theoretical model of inelastic features of O K edge spectrum for fitting the spectrum and resolving the elastic component, or performing the experiment at an instrument with a lower base temperature, since the amplitude of the order parameters of the uniform superconductivity and CDW will be larger at a lower temperature, and thus so is the order parameter of subharmonic order.

Chapter 6

Dynamics of charge density wave in $La_{2-x}Ba_xCuO_4$

This chapter has been adapted from Ref. [56] and [104].

6.1 Introduction: time-resolved x-ray scattering

In the previous chapter, we discussed a technique to detect fluctuating orders via their distribution in momentum space by integrating the scattering from the orders in quasi-elastic channel ($\Delta E \sim 0$). To determine the energy scale of the fluctuation, and thus to verify whether the order is indeed fluctuating or static, one needs a probe with an energy resolution, such as inelastic x-ray or electron scattering. The physical quantity that such techniques measure is the dynamic structure factor, $S(q, \omega)$. This quantity is related to the charge susceptibility, $\chi''(q, \omega)$, by the fluctuation-dissipation theorem, which provides a quantitative relationship between the weakly nonequilibrium dynamics of a system and its equilibrium fluctuations at finite temperature [56]. However, a limitation lies in the instrumental energy resolution. The energy scale of charge fluctuation could be of the same order as the superconducting gap, requiring instruments with sub-millielectron volt energy resolution to detect it. The inelastic x-ray and electron spectrometers with such energy resolution do not yet exist.

An alternative way to achieve sub-millielectron volt energy resolution is to study the collective excitations in the time domain. The effective energy resolution of a time-resolved experiment can be defined as $\Delta\omega = 2\pi\hbar/t_d$, where t_d is the time interval measured. Arbitrarily low energy scales can therefore be accessed by measuring for a long time interval. Furthermore, the fluctuation-dissipation theorem guarantees that the time-domain dynamics of a system may be used to shed light on its low-energy fluctuations in equilibrium.

When an ordered phase is excited out of equilibrium, its order parameter could exhibit any of several distinct types of dynamics. It might exhibit inertial dynamics, undergoing coherent oscillation around its equilibrium value at a characteristic frequency [105]. Alternatively, the order parameter might relax back to equilibrium gradually, through either dissipation or diffusive motion of excitations. Recent time-resolved optics studies of $YBa_2Cu_3O_{6+x}$ and $La_{2-x}Sr_xCuO_4$ showed coherent, millielectron volt-scale oscillations that were interpreted as an amplitude mode of the charge order [106–108], implying that the charge dynamics are inertial. However, optics experiments probe the system at zero momentum and are not selectively sensitive to CDW. Hence, momentum-resolved techniques capable of directly studying the dynamics of CDW are greatly needed.

Here, we used time-resolved resonant soft x-ray scattering (tr-RSXS) to study the dynamics of CDW in $\mathrm{La}_{2-x}\mathrm{Ba}_x\mathrm{CuO}_4$ with $x = 0.125$ (LBCO). We use 50-fs, 1.55-eV laser pulses to drive the charge order parameter out of equilibrium and probe its subsequent dynamics by scattering 60-fs x-ray pulses from a free-electron laser after a controlled time delay. In addition to an energy-integrating avalanche photodiode (APD), we used an energy-resolving soft x-ray grating spectrometer with a resolution of 0.7 eV. Using the latter makes this is a time-resolved resonant inelastic x-ray scattering (tr-RIXS) and allows the isolation of the resonant, valence band scattering from the fluorescence background.

6.2 Results

The tr-RSXS experiment was performed at the SXR beamline of the Linac Coherent Light Source (LCLS). The p-polarized x-ray beam energy was tuned to the Cu L_3 edge resonant condition with a repetition rate of 120 Hz. The p-polarized optical pump pulses of 1.55 eV, 120 Hz, and with a pulse duration of 50 fs were generated with a Ti:sapphire amplifier and propagated collinearly with the x-rays. The overall time resolution of approximately 130 fs was achieved. The pump-probe time delay was controlled by a mechanical translation stage. For energy-resolving measurements, a modular qRIXS grating spectrometer [109] that was installed on a fixed port at a scattering angle of 135° was used. A single crystal of LBCO x = 0.125 was grown using floating-zone method by Genda Gu at Brookhaven national laboratory.

6.2.1 Gapless excitations and diffusive dynamics of CDW

Figure 6.1(a) shows momentum scans through the CDW peak at a selection of time delays with a pump fluence of 0.1 mJ/cm^2. For analysis of the lineshape of the peak, each scan is fitted with a pseudo-Voigt profile,

$$I(q) = f\frac{1}{\pi g}\frac{A}{1+\left(\frac{q-Q_{\mathrm{CDW}}}{g}\right)^2} + (1-f)\frac{A}{g}\sqrt{\frac{\ln 2}{\pi}}\exp\left[-\ln 2\left(\frac{q-Q_{\mathrm{CDW}}}{g}\right)^2\right], \tag{6.1}$$

where the fit parameters are the linear mixing parameter f, amplitude A, peak position Q_{CDW}, and half-width-half-maximum (HWHM) g. The time delay dependence of the amplitude of the peak shows two main features: the melting of CDW by the pump upon its arrival (delay time = 0) due to an effective temperature

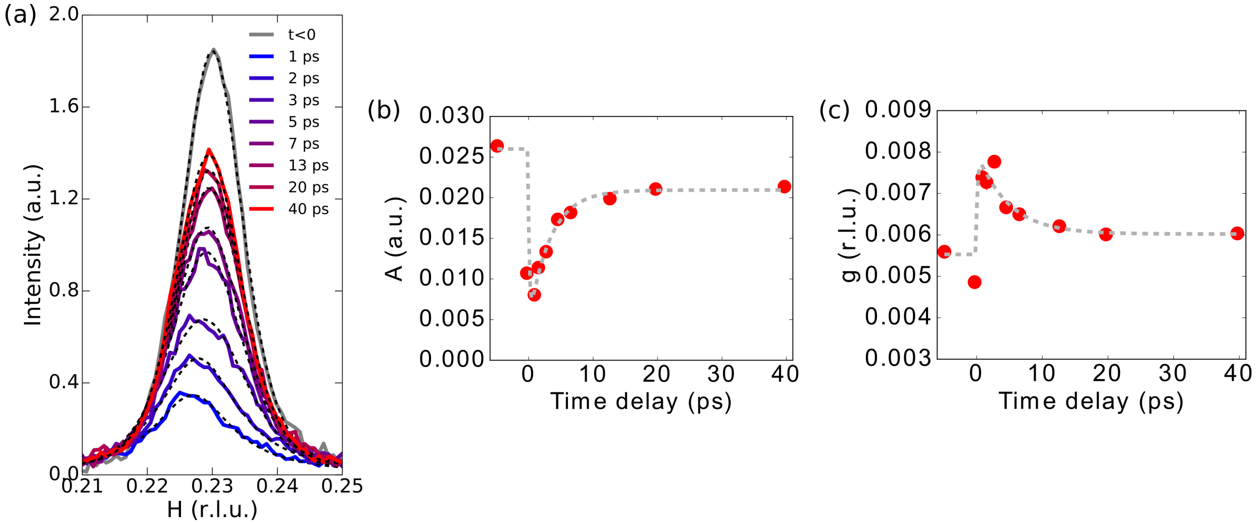

Figure 6.1: (a) H-scans of CDW for a selection of time delays. Dashed lines are fits using a pseudo-Voigt function. (b,c) Time-delay dependence of amplitude (b) and HWHM (c) of CDW from fits shown in (a). Reprinted with Permission from Ref. [56].

increase within a time scale of 100 fs, and its recovery over time that is much slower than the melting [Fig. 6.1(b)]. At the delay time of 1 ps, the peak is suppressed by 75% and broadened in momentum by 45% compared to its equilibrium value [Fig. 6.1(c)]. The broadening of the peak indicates the creation of microscopic heterogeneous structure in the CDW.

It is crucial to establish whether the peak changes observed are truly properties of the valence band ordering. Repeating the measurement using tr-RIXS with a resolution of 0.7 eV, we found that the peak suppression only takes place in the resonant, quasi-elastic scattering (Fig. 6.2). The other RIXS features, including the *dd* and charge transfer excitations and fluorescence emission, are unaffected by the pump. We conclude that the effects observed are properties of the valence band and that the time response will directly reveal the dynamics of the CDW.

After a delay time of 2 ps, the CDW intensity begins to recover. Figure 6.3 shows the energy-integrated intensity of the CDW peak for time delays 2 ps $\leq t \leq$ 10 ps, corresponding to an energy scale of 0.4 meV $\leq \omega \leq$ 2 meV. Unlike previous reports of a gapped amplitude mode [106–108], the recovery of the order parameter is purely exponential, lacking observable oscillations that would indicate inertial dynamics. This observation is unexpected because a conventional CDW is normally gapped either by the crystal lattice or by disorder, resulting in inertial dynamics [61]. We conclude that the dynamics of CDW in LBCO, previously thought to be static, are relaxational, meaning that the transverse excitations are gapless and will fluctuate at any temperature.

In the standard description of relaxational dynamics in a periodic system, a non-conserved order pa-

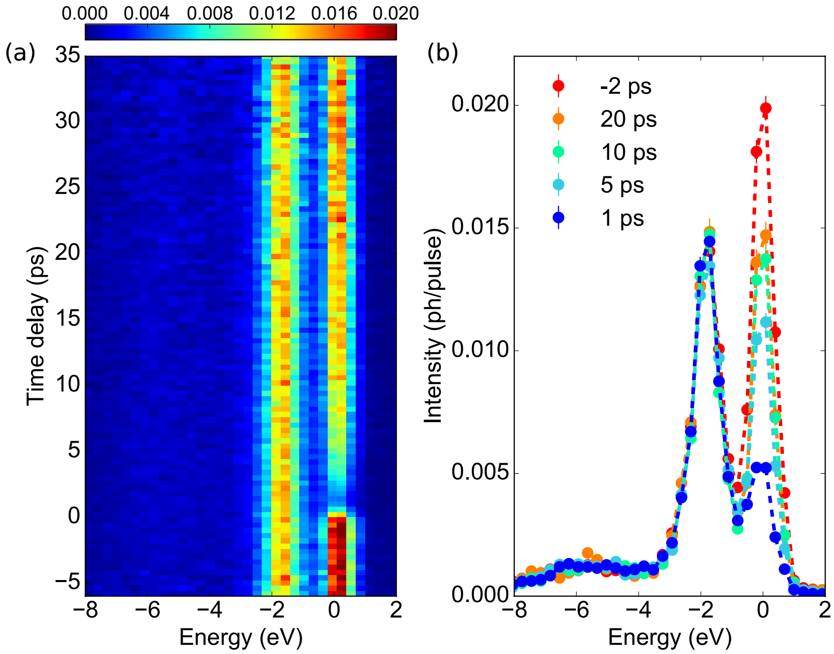

Figure 6.2: tr-RIXS measurement of CDW (a) Intensity map of tr-RIXS spectra of the CDW peak taken at a series of time delays. (b) tr-RIXS spectra at a selection of time delays. The quasi-elastic scattering from the CDW appears at zero energy and is the only spectral feature influenced by the pump. Reprinted with Permission from Ref. [56].

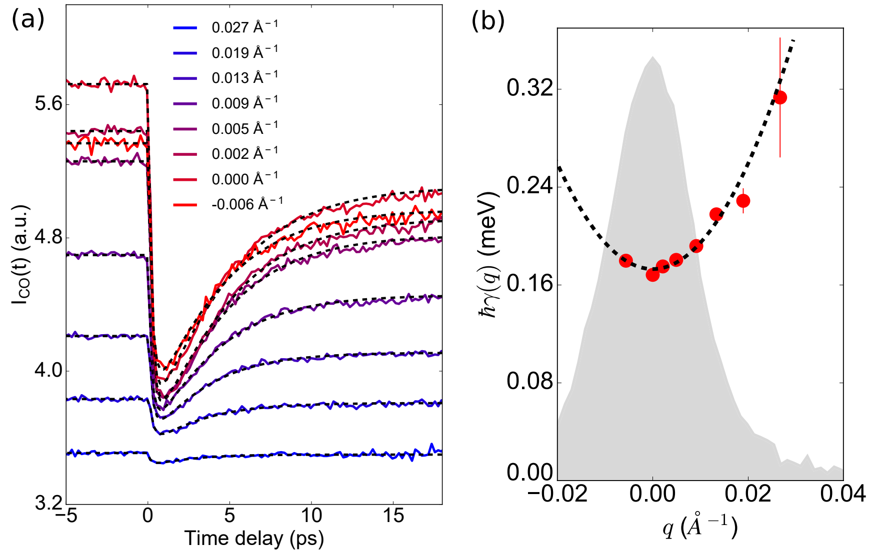

Figure 6.3: (a) Time traces of the energy-integrated CDW scattering for a selection of momenta $q = |\boldsymbol{Q} - \boldsymbol{Q}_{\mathrm{CDW}}|^2$. Dashed lines are fits using a single exponential recovery model given as Eq. (6.3). (b) Exponential decay parameter, $\gamma(q)$, as a function of relative momentum difference. Dashed line is a fit to the data using Eq. (6.2). Shaded area is the lineshape of the unperturbed CDW reflection. Reprinted with Permission from Ref. [56].

rameter driven weakly out of equilibrium will have a time dependence proportional to $\exp[-\gamma(q)t]$, where $q = |\boldsymbol{Q} - \boldsymbol{Q}_{\mathrm{CDW}}|$ is the momentum relative to the CDW peak and

$$\gamma(q) = \gamma_0 + Dq^2, \tag{6.2}$$

where γ_0 describes pure dissipation, and the momentum dependence arise from diffusion quantified by the parameter, D [56].

Figure 6.3(a) shows time traces of the CDW intensity for $t \leq 10$ ps and for a selection of momenta $\boldsymbol{Q}$ along the transverse direction around $\boldsymbol{Q}_{\mathrm{CDW}}$. Each curve is fitted well by an exponential recovery model,

$$I(t) = \left|\Delta_0 - \Theta(t - t_d)\left[1 - \exp\left(-\frac{t - t_d}{\tau_0}\right)\right]\left[A_0 + A_1 \exp\left(-\frac{t - td}{\tau}\right)\right]\right|^2 + I_{\mathrm{bkg}}, \tag{6.3}$$

where the first exponential term represents the pump-induced melting that saturates in a very short timescale τ_0 and the second exponential term represents the exponential recovery. A_1 represents the exponential amplitude and τ is the timescale of the exponential recovery. A_0 is an offset capturing the long-time relaxation of the CDW, t_d is the parameter for the zero time delay, Δ_0 is the equilibrium value of the intensity, and I_{bkg} is the fluorescence contribution to the overall intensity.

We found that the relaxation rate is highly momentum dependent, increasing rapidly with q [Fig. 6.3(b)], and is fit well by Eq. (6.2), yielding dissipation parameter $\hbar\gamma_0 = (0.1730 \pm 0.0015)$ meV and diffusion constant $\hbar D = (215 \pm 19)$ meV$\cdot\mathring{A}^2$. These two quantities imply the transverse collective excitations of the CDW in LBCO propagate by diffusion, with a characteristic diffusion length $\lambda = \sqrt{2D/\gamma_0} = (49.9 \pm 2.2)\mathring{A}$ and dissipation time $1/\gamma_0 = (3.805 \pm 0.031)$ ps.

Our results show that the CDW in LBCO is dynamic, undergoing transverse fluctuations at millielectron volt energy scales. On an energy scale of 0.4 to 2 meV, the dynamics are relaxational, meaning that the collective excitations are gapless and propagate by diffusion.

6.2.2 Photoinduced sliding of CDW

We also discovered a transient sliding CDW state induced by the optical pump. The tr-RIXS spectrum shows three features: a quasielastic peak, a *dd* excitation, and a charge transfer (CT) components. To analyze the time delay dependence of each component, the spectra are fitted with a model consisting a Gaussian function for the quasielastic component, and two Lorentzian functions for the *dd* and CT components [Fig. 6.4(a)]. The fitting result revealed that the spectrum at 1 ps after the arrival of the pump exhibits a short-lived 80-meV pump-induced redshift [Fig. 6.4(b), (c)]. Due to the limited energy resolution, we could not conclude

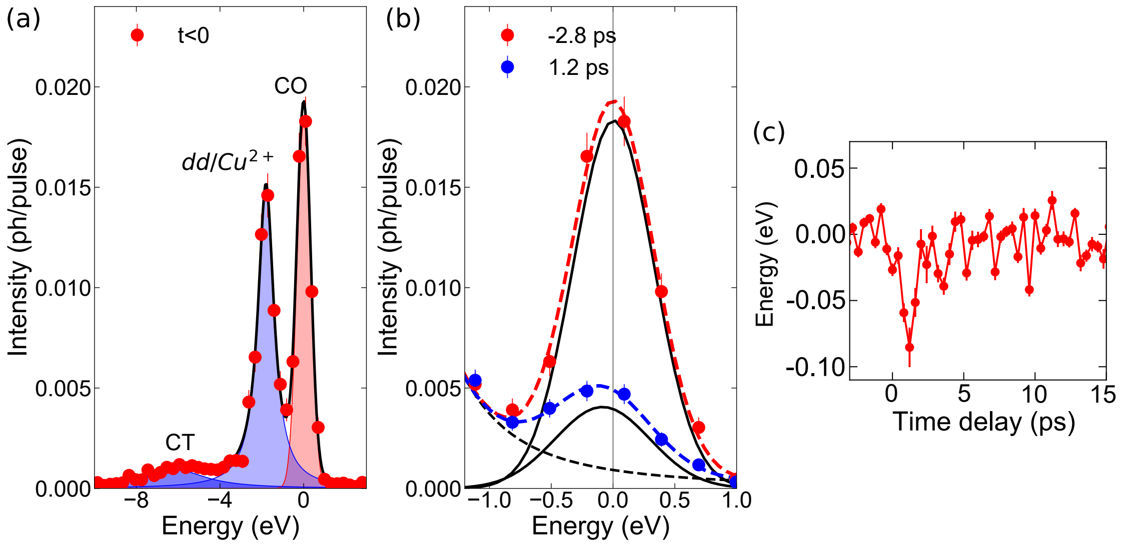

Figure 6.4: (a) tr-RIXS spectrum of CDW. Red area indicates the quasielastic scattering from the charge order (CO) modeled by a Gaussian function. Blue areas indicate *dd* and charge transfer (CT) excitations modeled by two Lorentzian functions. (b) Enlarged view of the quasielastic spectrum before (red) and after (blue) the arrival of the pump. The solid black lines are the Gaussian components of the fits, and the black dashed line is the Lorentzian fit to the *dd* excitations. (c) Time delay dependence of the center of the Gaussian component, representing the energy of the quasielastic energy. Reprinted with Permission from Ref. [104].

whether this phenomenon is due to an actual redshift of the elastic line or to the creation of low-energy ($\hbar\omega < 0.3$ eV) inelastic excitations.

In addition to the energy redshift, the CDW peak also changes in momentum [Fig. 6.5(a)]. We found a maximum pump-induced momentum shift $\Delta q \sim 0.003$ r.l.u., along the H momentum direction, but not along the perpendicular K direction. This pump-induced phenomenon could originate from any of three possible effects: (1) a change in the sample refractive index in the soft x-ray regime, which would alter the measured Bragg reflection angle [110]; (2) a change in the CDW periodicity; or (3) a collective recoil of the CDW.

A pump-induced change in the refractive index would also affect other diffraction peaks. However we observed no corresponding pump-induced shift in the $(0, 0, 1)$ Bragg reflection of the low-temperature tetragonal structure [Fig. 6.5(c), thus ruling out this first possible explanation.

On the other hand, changes in the CDW periodicity have been observed in a wide variety of systems under the effect of external electric fields or currents [111–113] and are ascribed to deformations of the density-wave modulation $\rho(x)$, defined as

$$\rho(x) = \rho_0 + \Delta\rho\cos(Q_{\mathrm{CDW}}x + \varphi) \tag{6.4}$$

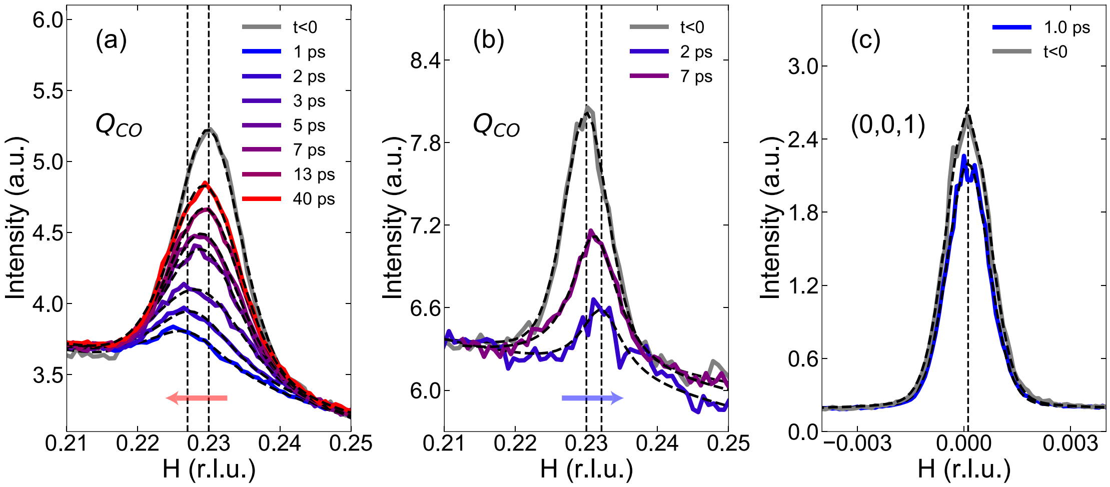

Figure 6.5: H scans of the CDW for a selection of time delays taken at (a) $\phi = 0$ and (b) $\phi = \pi$. Dashed vertical lines indicate the position of the peak at equilibrium and the maximum observed shift. (c) H scans of the $(0, 0, 1)$ structural Bragg peak before and after the pump arrival. Reprinted with Permission from Ref. [104].

where ρ_0 is the background charge density, $\Delta\rho$ is the CDW modulation, x is the spatial coordinate, and φ is the CDW phase. Deforming the CDW modulation is equivalent to introducing a spatial dependence in the phase φ. To the lowest order, a linear gradient in the phase $\varphi(x) = \varphi_0 + (\partial_x\varphi)x$ is equivalent to altering the CDW wave vector. In other words, the distorted CDW modulation is likely to have the form

$$\rho'(x) = \rho_0 + \Delta\rho \cos[Q_{\mathrm{CDW}}x + \varphi_0 + (\partial_x\varphi)x] \tag{6.5}$$

$$= \rho_0 + \Delta\rho \cos(Q'_{\mathrm{CDW}}x + \varphi_0) \tag{6.6}$$

with $Q'_{\mathrm{CDW}} = Q_{\mathrm{CDW}} + (\partial_x\varphi)$. In order to test this possibility, we rotated the sample azimuthal angle ϕ by 180° and repeated the measurement of H scans of the same CDW reflection [Fig. 6.5(b)]. This is equivalent to changing the orientation of the pump propagation axis with respect to the H direction. In our geometry $\phi = 0$ corresponds to a pump propagating from positive to negative H, while $\phi = \pi$ corresponds to a pump propagating from negative to positive H [Fig. 6.6(a), (b)]. If the shift were due to a periodicity change, such a rotation would not affect the Δq momentum shift as measured in the reference frame of the sample and it would be independent of the pump, as illustrated in Fig. 6.6(d).

Surprisingly, we instead observe a reversal in the momentum shift [Fig. 6.5(b) and 6.6(c)], meaning the peak moves a fixed direction with respect to the propagation of the pump, not to the crystal axes, excluding a CDW periodicity change. In other words, the pump exchanges momentum Δq with the CDW condensate along its propagation axis.

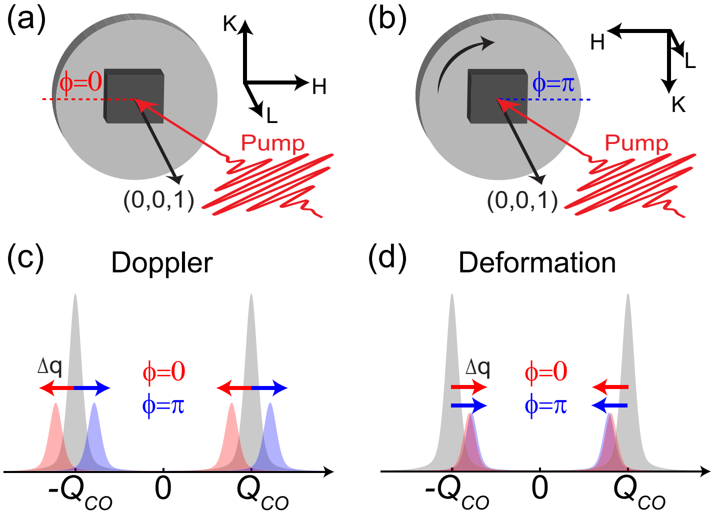

Figure 6.6: (a) Scattering geometry at $\phi = 0$, with the pump propagating from positive to negative H, and (b) at $\phi = \pi$, the pump propagating from negative to positive H. (c) Observed Doppler recoil of the CDW from the equilibrium diffraction peak (gray) to the Δq-shifted reflection at $\phi = 0$ (red) and $\phi = \pi$ (blue). (d) Diffraction peak shift due to a change of the charge-density periodicity (deformation). Reprinted with Permission from Ref. [104].

This reversal in momentum shift leads to the conclusion that the pump induces a sliding motion of the CDW condensate with a uniform momentum Δq or, equivalently, creates a nonequilibrium population of collective modes exhibiting a nonzero center-of-mass momentum. If the condensate is coherently set in motion, the elastic peak located at $(Q_{\mathrm{CDW}}, \omega = 0)$ will shift both in energy and in momentum $(Q_{\mathrm{CDW}} \pm \Delta q, \omega \mp v\Delta q)$ [114] and the direction will be dictated by the applied field. This is, in essence, a manifestation of the Doppler effect for a moving electronic system.

As this phenomenon is expected to exhibit a simultaneous shift of the elastic line by $\Delta\omega = \mp v\Delta q$ [114], where v is the phason velocity of the CDW, one could naively identify the observed 80-meV RIXS redshift in Figs. 6.4(b) and (c) with such energy change. This would imply a condensate velocity $v = \Delta\omega/\Delta q = 16$ eV×Å ($v = 2.4 \times 10^6$ m/s), far greater than the nodal Fermi velocity $v_F \sim 1.7$ eV×Å (2.6×10^5 m/s) [115], which is regarded as a limiting value for the electronic velocity of a CDW [61]. Given this rather unphysical value, we conclude that the observed energy redshift, characterizing the spectrum of the sliding CO, is due to a distinct effect coexisting with the Doppler shift. For example, it could be that the high-energy excitation spectrum of a sliding CDW is different from that of a CDW in equilibrium.

Chapter 7

Conclusions

In this thesis, in-depth studies on properties of CDW in pnictide and cuprate superconductors were performd using various x-ray scattering techniques. Using the in-lab hard x-ray instrument, new CDW phases were discovered in nickel pnictide superconductors $\mathrm{Ba(Ni_{1-x}Co_x)_2As_2}$ and $\mathrm{Ba_{1-x}Sr_xNi_2As_2}$, and the evolution of the CDW orders upon doping indicated that CDW may be the origin of the suppression of T_c and filamentary superconductivity in these systems. Furthermore, synchrotron and free-electron laser x-ray sources were used to study various aspects of CDW in cuprates. The resonant soft x-ray scattering measurements on CDW in $\mathrm{La_{1.8-x}Eu_{0.2}Sr_xCuO_4}$ revealed that the CDW orders are well-developed at much higher temperatures than previously thought, and phase fluctuations due to disorders play important role on the temperature dependence of CDW. The results on the temperature and doping evolution of the CDW wave vector provided an explanation for the opposite sign of the doping evolution observed in La-cuprates and other cuprate families, suggesting a presence of a universal mechanism of CDW in cuprates. Our results were further supported by theoretical models. Also, CDW in $\mathrm{La_{2-x}Ba_xCuO_4}$ was measured not only in momentum domain, but also in time and energy domain, revealing the previously unidentified fluctuating nature of the CDW. These results confirmed that CDW is a central feature of the phase diagram of unconventional superconductors, and will provide a better guidance to future studies to resolve the problem of high temperature superconductivity.

References

[1] J. Bardeen, L. N. Cooper, and J. R. Schrieffer. Microscopic theory of superconductivity. *Phys. Rev.*, 106:162–164, Apr 1957.

[2] D. J. Van Harlingen. Phase-sensitive tests of the symmetry of the pairing state in the high-temperature superconductors - Evidence for $d_{x^2-y^2}$ symmetry. *Rev. Mod. Phys.*, 67:515–535, Apr 1995.

[3] J. G. Bednorz and K. A. Müller. Possible high T_c superconductivity in the Ba-La-Cu-O system. *Zeitschrift für Physik B Condensed Matter*, 64(2):189–193, Jun 1986.

[4] M. K. Wu, J. R. Ashburn, C. J. Torng, P. H. Hor, R. L. Meng, L. Gao, Z. J. Huang, Y. Q. Wang, and C. W. Chu. Superconductivity at 93 K in a new mixed-phase Y-Ba-Cu-O compound system at ambient pressure. *Phys. Rev. Lett.*, 58:908–910, Mar 1987.

[5] B. Keimer, S. A. Kivelson, M. R. Norman, S. Uchida, and J. Zaanen. From quantum matter to high-temperature superconductivity in copper oxides. *Nature*, 518(7538):179–186, Feb 2015.

[6] Yoichi Kamihara, Takumi Watanabe, Masahiro Hirano, and Hideo Hosono. Iron-based layered superconductor $La[O_{1-x}F_x]FeAs$ ($x = 0.05 - 0.12$) with $T_c = 26$ K. *J. Am. Chem. Soc.*, 130:3296–3297, 2008.

[7] Johnpierre Paglione and Richard L. Greene. High-temperature superconductivity in iron-based materials. *Nat. Phys.*, 6:645–658, 2010.

[8] F. Steglich, J. Aarts, C. D. Bredl, W. Lieke, D. Meschede, W. Franz, and H. Schäfer. Superconductivity in the presence of strong pauli paramagnetism: $CeCu_2Si_2$. *Phys. Rev. Lett.*, 43:1892–1896, Dec 1979.

[9] G. R. Stewart. Heavy-fermion systems. *Rev. Mod. Phys.*, 56:755–787, Oct 1984.

[10] Jérome, D., Mazaud, A., Ribault, M., and Bechgaard, K. Superconductivity in a synthetic organic conductor $(TMTSF)_2PF_6$. *J. Physique Lett.*, 41(4):95–98, 1980.

[11] S. S. P. Parkin, E. M. Engler, R. R. Schumaker, R. Lagier, V. Y. Lee, J. C. Scott, and R. L. Greene. Superconductivity in a new family of organic conductors. *Phys. Rev. Lett.*, 50:270–273, Jan 1983.

[12] Eduardo Fradkin, Steven A. Kivelson, and John M. Tranquada. Colloquium: Theory of intertwined orders in high temperature superconductors. *Rev. Mod. Phys.*, 87:457–482, May 2015.

[13] Chris Eckberg, Daniel J. Campbell, Tristin Metz, John Collini, Halyna Hodovanets, Tyler Drye, Peter Zavalij, Morten H. Christensen, Rafael M. Fernandes, Sangjun Lee, Peter Abbamonte, Jeffrey W. Lynn, and Johnpierre Paglione. Sixfold enhancement of superconductivity in a tunable electronic nematic system. *Nature Physics*, 16(3):346–350, 2020.

[14] M. Hücker, M. v. Zimmermann, G. D. Gu, Z. J. Xu, J. S. Wen, Guangyong Xu, H. J. Kang, A. Zheludev, and J. M. Tranquada. Stripe order in superconducting $La_{2-x}Ba_xCuO_4$ ($0.095 \leq x \leq 0.155$). *Phys. Rev. B*, 83:104506, Mar 2011.

[15] J. Chang, E. Blackburn, A. T. Holmes, N. B. Christensen, J. Larsen, J. Mesot, Ruixing Liang, D. A. Bonn, W. N. Hardy, A. Watenphul, M. v. Zimmermann, E. M. Forgan, and S. M. Hayden. Direct observation of competition between superconductivity and charge density wave order in $YBa_2Cu_3O_{6.67}$. *Nature Physics*, 8(12):871–876, Dec 2012.

[16] T. P. Croft, C. Lester, M. S. Senn, A. Bombardi, and S. M. Hayden. Charge density wave fluctuations in $La_{2-x}Sr_xCuO_4$ and their competition with superconductivity. *Phys. Rev. B*, 89:224513, Jun 2014.

[17] C. Eckberg, L. Wang, H. Hodovanets, H. Kim, D. J. Campbell, P. Zavalij, P. Piccoli, and J. Paglione. Evolution of structure and superconductivity in $Ba(Ni_{1-x}Co_x)_2As_2$. *Phys. Rev. B*, 97:224505, Jun 2018.

[18] Athena S. Sefat, Michael A. McGuire, Rongying Jin, Brian C. Sales, David Mandrus, Filip Ronning, E. D. Bauer, and Yurij Mozharivskyj. Structure and anisotropic properties of $BaFe_{2-x}Ni_xAs_2$ ($x = 0$, 1, and 2) single crystals. *Phys. Rev. B*, 79:094508, Mar 2009.

[19] N. Ni, M. E. Tillman, J.-Q. Yan, A. Kracher, S. T. Hannahs, S. L. Bud'ko, and P. C. Canfield. Effects of co substitution on thermodynamic and transport properties and anisotropic H_{c2} in $Ba(Fe_{1-x}Co_x)_2as_2$ single crystals. *Phys. Rev. B*, 78:214515, Dec 2008.

[20] K. Kothapalli, F. Ronning, E. D. Bauer, A. J. Schultz, and H. Nakotte. Single-crystal neutron diffraction studies on Ni-based metal-pnictide superconductor $BaNi_2As_2$. *J. Phys.: Conf. Ser.*, 251:012010, 2010.

[21] Hideo Hosono, Keiichi Tanabe, Eiji Takayama-Muromachi, Hiroshi Kageyama, Shoji Yamanaka, Hiroaki Kumakura, Minoru Nohara, Hidenori Hiramatsu, and Satoru Fujitsu. Exploration of new superconductors and functional materials, and fabrication of superconducting tapes and wires of iron pnictides. *Science and Technology of Advanced Materials*, 16(3):033503, 2015.

[22] Riccardo Comin and Andrea Damascelli. Resonant x-ray scattering studies of charge order in cuprates. *Annual Review of Condensed Matter Physics*, 7(1):369–405, 2016.

[23] J. M. Tranquada, B. J. Sternlieb, J. D. Axe, Y. Nakamura, and S. Uchida. Evidence for stripe correlations of spins and holes in copper oxide superconductors. *Nature*, 375(6532):561–563, Jun 1995.

[24] Jörg Fink, Victor Soltwisch, Jochen Geck, Enrico Schierle, Eugen Weschke, and Bernd Büchner. Phase diagram of charge order in $La_{1.8-x}Eu_{0.2}Sr_xCuO_4$ from resonant soft x-ray diffraction. *Phys. Rev. B*, 83:092503, Mar 2011.

[25] P. Abbamonte, A. Rusydi, S. Smadici, G. D. Gu, G. A. Sawatzky, and D. L. Feng. Spatially modulated 'Mottness' in $La_{2-x}Ba_xCuO_4$. *Nature Physics*, 1(3):155–158, December 2005.

[26] G. Ghiringhelli, M. Le Tacon, M. Minola, S. Blanco-Canosa, C. Mazzoli, N. B. Brookes, G. M. De Luca, A. Frano, D. G. Hawthorn, F. He, T. Loew, M. Moretti Sala, D. C. Peets, M. Salluzzo, E. Schierle, R. Sutarto, G. A. Sawatzky, E. Weschke, B. Keimer, and L. Braicovich. Long-range incommensurate charge fluctuations in $(Y,Nd)Ba_2Cu_3O_{6+x}$. *Science*, 337(6096):821–825, 2012.

[27] Eduardo H. da Silva Neto, Pegor Aynajian, Alex Frano, Riccardo Comin, Enrico Schierle, Eugen Weschke, András Gyenis, Jinsheng Wen, John Schneeloch, Zhijun Xu, Shimpei Ono, Genda Gu, Mathieu Le Tacon, and Ali Yazdani. Ubiquitous interplay between charge ordering and high-temperature superconductivity in cuprates. *Science*, 343(6169):393–396, 2014.

[28] R. Comin, A. Frano, M. M. Yee, Y. Yoshida, H. Eisaki, E. Schierle, E. Weschke, R. Sutarto, F. He, A. Soumyanarayanan, Yang He, M. Le Tacon, I. S. Elfimov, Jennifer E. Hoffman, G. A. Sawatzky, B. Keimer, and A. Damascelli. Charge order driven by fermi-arc instability in $Bi_2Sr_{2-x}La_xCuO_{6+\delta}$. *Science*, 343(6169):390–392, 2014.

[29] K. Yamada, C. H. Lee, K. Kurahashi, J. Wada, S. Wakimoto, S. Ueki, H. Kimura, Y. Endoh, S. Hosoya, G. Shirane, R. J. Birgeneau, M. Greven, M. A. Kastner, and Y. J. Kim. Doping dependence of the spatially modulated dynamical spin correlations and the superconducting-transition temperature in $La_{2-x}Sr_xCuO_4$. *Phys. Rev. B*, 57:6165–6172, Mar 1998.

[30] J. E. Hoffman, E. W. Hudson, K. M. Lang, V. Madhavan, H. Eisaki, S. Uchida, and J. C. Davis. A four unit cell periodic pattern of quasi-particle states surrounding vortex cores in $Bi_2Sr_2CaCu_2O_{8+\delta}$. *Science*, 295(5554):466–469, 2002.

[31] H. Miao, J. Lorenzana, G. Seibold, Y. Y. Peng, A. Amorese, F. Yakhou-Harris, K. Kummer, N. B. Brookes, R. M. Konik, V. Thampy, G. D. Gu, G. Ghiringhelli, L. Braicovich, and M. P. M. Dean. High-temperature charge density wave correlations in $La_{1.875}Ba_{0.125}CuO_4$ without spin-charge locking. *Proceedings of the National Academy of Sciences*, 114(47):12430–12435, 2017.

[32] V. Thampy, X. M. Chen, Y. Cao, C. Mazzoli, A. M. Barbour, W. Hu, H. Miao, G. Fabbris, R. D. Zhong, G. D. Gu, J. M. Tranquada, I. K. Robinson, S. B. Wilkins, and M. P. M. Dean. Static charge-density-wave order in the superconducting state of $La_{2-x}Ba_xCuO_4$. *Phys. Rev. B*, 95:241111, Jun 2017.

[33] X. M. Chen, V. Thampy, C. Mazzoli, A. M. Barbour, H. Miao, G. D. Gu, Y. Cao, J. M. Tranquada, M. P. M. Dean, and S. B. Wilkins. Remarkable stability of charge density wave order in $La_{1.875}Ba_{0.125}CuO_4$. *Phys. Rev. Lett.*, 117:167001, Oct 2016.

[34] N. W. Ashcroft and N. D. Mermin. *Solid State Physics.* Brooks/Cole, Belmont, CA, 1976.

[35] Jens Als-Nielsen and Des McMorrow. *Elements of Modern X-ray Physics.* John Wiley & Sons, Ltd, United Kingdom, 2011.

[36] Sunil K Sinha. Theory of inelastic x-ray scattering from condensed matter. *Journal of Physics: Condensed Matter*, 13(34):7511–7523, 2001.

[37] J. J. Sakurai. *Advanced Quantum Mechanics.* Addison-Wesley Pub Co,, Reading, MA, 1967.

[38] Achkar, Andrew. *Charge Density Wave Order in Cuprate Superconductors Studied by Resonant Soft X-ray Scattering.* PhD thesis, University of Waterloo, 2015.

[39] M. W. Haverkort, N. Hollmann, I. P. Krug, and A. Tanaka. Symmetry analysis of magneto-optical effects: The case of x-ray diffraction and x-ray absorption at the transition metal $L_{2,3}$ edge. *Phys. Rev. B*, 82:094403, Sep 2010.

[40] M. Lohmeier and E. Vlieg. Angle calculations for a six-circle surface x-ray diffractometer. *Journal of Applied Crystallography*, 26(5):706–716, 1993.

[41] W. R. Busing and H. A. Levy. Angle calculations for 3- and 4-circle X-ray and neutron diffractometers. *Acta Crystallographica*, 22(4):457–464, Apr 1967.

[42] `https://certif.com/content/spec`.

[43] Sangjun Lee, Gilberto de la Peña, Stella X.-L. Sun, Matteo Mitrano, Yizhi Fang, Hoyoung Jang, Jun-Sik Lee, Chris Eckberg, Daniel Campbell, John Collini, Johnpierre Paglione, F. M. F. de Groot, and Peter Abbamonte. Unconventional charge density wave order in the pnictide superconductor $Ba(Ni_{1-x}Co_x)_2As_2$. *Phys. Rev. Lett.*, 122:147601, Apr 2019.

[44] Jörg Fink, Enrico Schierle, Eugen Weschke, Jochen Geck, David Hawthorn, Viktor Soltwisch, Hiroki Wadati, Hsueh-Hung Wu, Hermann A. Dürr, Nadja Wizent, Bernd Büchner, and George A. Sawatzky. Charge ordering in $La_{1.8-x}Eu_{0.2}Sr_xCuO_4$ studied by resonant soft x-ray diffraction. *Phys. Rev. B*, 79:100502, Mar 2009.

[45] F. C. Zhang and T. M. Rice. Effective Hamiltonian for the superconducting Cu oxides. *Phys. Rev. B*, 37:3759–3761, Mar 1988.

[46] D. C. Peets, D. G. Hawthorn, K. M. Shen, Young-June Kim, D. S. Ellis, H. Zhang, Seiki Komiya, Yoichi Ando, G. A. Sawatzky, Ruixing Liang, D. A. Bonn, and W. N. Hardy. X-ray absorption spectra reveal the inapplicability of the single-band Hubbard model to overdoped cuprate superconductors. *Phys. Rev. Lett.*, 103:087402, Aug 2009.

[47] N. Nücker, E. Pellegrin, P. Schweiss, J. Fink, S. L. Molodtsov, C. T. Simmons, G. Kaindl, W. Frentrup, A. Erb, and G. Müller-Vogt. Site-specific and doping-dependent electronic structure of $\mathrm{YBa_2Cu_3O}_x$ probed by O 1s and Cu 2p x-ray-absorption spectroscopy. *Phys. Rev. B*, 51:8529–8542, Apr 1995.

[48] Eduardo H. da Silva Neto, Riccardo Comin, Feizhou He, Ronny Sutarto, Yeping Jiang, Richard L. Greene, George A. Sawatzky, and Andrea Damascelli. Charge ordering in the electron-doped superconductor $\mathrm{Nd}_{2-x}\mathrm{Ce}_x\mathrm{CuO}_4$. *Science*, 347(6219):282–285, 2015.

[49] Sangjun Lee, John Collini, Stella X.-L. Sun, Matteo Mitrano, Eckberg-Chris Guo, Xuefei, Johnpierre Paglione, Eduardo Fradkin, and Peter Abbamonte. Multiple charge density wave orders in $\mathrm{Ba}_{1-x}\mathrm{Sr}_x\mathrm{Ni_2As_2}$. *in prepration*, 2020.

[50] Pan Zhang and Hui fei Zhai. Superconductivity in 122-type pnictides without iron. *Cond. Mat.*, 2:28, 2017.

[51] J. M. Tranquada. Modulated superfluid density in an iron-pnictide superconductor. *Physics*, 3:41, 2010.

[52] T. Park, H. Lee, E. D. Bauer, J. D. Thompson, and F. Ronning. Pressure dependence of $\mathrm{BaNi_2As_2}$. *J. Physics: Conf. Ser.*, 200:012155, 2010.

[53] Pengcheng Dai. Antiferromagnetic order and spin dynamics in iron-based superconductors. *Rev. Mod. Phys.*, 87:855–896, Aug 2015.

[54] John M. Tranquada. Exploring intertwined orders in cuprate superconductors. *Physica B: Condensed Matter*, 460:136 – 140, 2015.

[55] S. A. Kivelson, I. P. Bindloss, E. Fradkin, V. Oganesyan, J. M. Tranquada, A. Kapitulnik, and C. Howald. How to detect fluctuating stripes in the high-temperature superconductors. *Rev. Mod. Phys.*, 75:1201–1241, Oct 2003.

[56] Matteo Mitrano, Sangjun Lee, Ali A. Husain, Luca Delacretaz, Minhui Zhu, Gilberto de la Peña Munoz, Stella X.-L. Sun, Young Il Joe, Alexander H. Reid, Scott F. Wandel, Giacomo Coslovich, William Schlotter, Tim van Driel, John Schneeloch, G. D. Gu, Sean Hartnoll, Nigel Goldenfeld, and Peter Abbamonte. Ultrafast time-resolved x-ray scattering reveals diffusive charge order dynamics in $\mathrm{La}_{2-x}\mathrm{Ba}_x\mathrm{CuO}_4$. *Science Advances*, 5(8), 2019.

[57] S. Avci, O. Chmaissem, D. Y. Chung, S. Rosenkranz, E. A. Goremychkin, J. P. Castellan, I. S. Todorov, J. A. Schlueter, H. Claus, A. Daoud-Aladine, D. D. Khalyavin, M. G. Kanatzidis, and R. Osborn. Phase diagram of $\mathrm{Ba}_{1-x}\mathrm{K}_x\mathrm{Fe_2As_2}$. *Phys. Rev. B*, 85:184507, May 2012.

[58] M. G. Kim, D. K. Pratt, G. E. Rustan, W. Tian, J. L. Zarestky, A. Thaler, S. L. Bud'ko, P. C. Canfield, R. J. McQueeney, A. Kreyssig, and A. I. Goldman. Magnetic ordering and structural distortion in Ru-doped $\mathrm{BaFe_2As_2}$ single crystals studied by neutron and x-ray diffraction. *Phys. Rev. B*, 83:054514, Feb 2011.

[59] Jiun-Haw Chu, Hsueh-Hui Kuo, James G. Analytis, and Ian R. Fisher. Divergent nematic susceptibility in an iron arsenide superconductor. *Science*, 337(6095):710–712, 2012.

[60] Hsueh-Hui Kuo, Jiun-Haw Chu, Johanna C. Palmstrom, Steven A. Kivelson, and Ian R. Fisher. Ubiquitous signatures of nematic quantum criticality in optimally doped Fe-based superconductors. *Science*, 352(6288):958–962, 2016.

[61] George Grüner. *Density Waves in Solids.* Perseus, Cambridge, MA, 2000.

[62] K. Rossnagel. On the origin of charge-density waves in select layered transition-metal dichalcogenides. *J. Phys.:Cond. Mat.*, 23:213001, 2011.

[63] W. L. McMillan. Theory of discommensurations and the commensurate-incommensurate charge-density-wave phase transition. *Phys. Rev. B*, 14:1496, 1976.

[64] D. E. Moncton, J. D. Axe, and F. J. DiSalvo. Study of superlattice formation in 2H-$NbSe_2$ and 2H-$TaSe_2$ by neutron scattering. *Phys. Rev. Lett.*, 34:734–737, 1975.

[65] B. Sipos, A. F. Kusmartseva, A. Akrap, H. Berger, L. Forro, and E. Tutis. From Mott state to superconductivity in 1T-TaS_2. *Nat. Mater.*, 7:960–965, 2008.

[66] B. Zhou, M. Xu, Y. Zhang, G. Xu, C. He, L. X. Yang, F. Chen, B. P. Xie, X.-Y. Cui, M. Arita, K. Shimada, H. Namatame, M. Taniguchi, X. Dai, and D. L. Feng. Electronic structure of $BaNi_2As_2$. *Phys. Rev. B*, 83:035110, 2011.

[67] B. Kalisky, J. R. Kirtley, J. G. Analytis, Jiun-Haw Chu, A. Vailionis, I. R. Fisher, and K. A. Moler. Stripes of increased diamagnetic susceptibility in underdoped superconducting $Ba(Fe_{1-x}Co_x)_2As_2$ single crystals: Evidence for an enhanced superfluid density at twin boundaries. *Phys. Rev. B*, 81:184513, May 2010.

[68] H. Xiao, T. Hu, A. P. Dioguardi, N. apRoberts Warren, A. C. Shockley, J. Crocker, D. M. Nisson, Z. Viskadourakis, Xianyang Tee, I. Radulov, C. C. Almasan, N. J. Curro, and C. Panagopoulos. Evidence for filamentary superconductivity nucleated at antiphase domain walls in antiferromagnetic $CaFe_2As_2$. *Phys. Rev. B*, 85:024530, Jan 2012.

[69] Y. I. Joe, X. M. Chen, P. Ghaemi, K. D. Finkelstein, G. A. de la Peña, Y. Gan, J. C. T. Lee, S. Yuan, J. Geck, G. J. MacDougall, T. C. Chiang, S. L. Cooper, E. Fradkin, and P. Abbamonte. Emergence of charge density wave domain walls above the superconducting dome in 1T-$TiSe_2$. *Nature Physics*, 10(6):421–425, Jun 2014.

[70] Shichao Yan, Davide Iaia, Emilia Morosan, Eduardo Fradkin, Peter Abbamonte, and Vidya Madhavan. Influence of domain walls in the incommensurate charge density wave state of Cu intercalated $1T-\mathrm{TiSe}_2$. *Phys. Rev. Lett.*, 118:106405, Mar 2017.

[71] Sangjun Lee, Edwin W. Huang, Thomas Johnson, Xuefei Guo, Matteo Mitrano, Alexander V. Zakrzewski, Gilberto de la Peña, Yingying Peng, Hai Hunag, Sang-Jun Lee, Hoyoung Jang, Jun-Sik Lee, Young Il Joe, William B. Doriese, Paul Szypryt, Daniel S. Swetz, Gregory J. MacDougall, Steven A. Kivelson, Eduardo Fradkin, and Peter Abbamonte. Evolution of charge order wave vector in $La_{1.8-x}Eu_{0.2}Sr_xCuO_4$. *in prepration*, 2020.

[72] E. Blackburn, J. Chang, M. Hücker, A. T. Holmes, N. B. Christensen, Ruixing Liang, D. A. Bonn, W. N. Hardy, U. Rütt, O. Gutowski, M. v. Zimmermann, E. M. Forgan, and S. M. Hayden. X-ray diffraction observations of a charge-density-wave order in superconducting Ortho-II $YBa_2Cu_3\mathbf{O}_{6.54}$ single crystals in zero magnetic field. *Phys. Rev. Lett.*, 110:137004, Mar 2013.

[73] M. Hücker, N. B. Christensen, A. T. Holmes, E. Blackburn, E. M. Forgan, Ruixing Liang, D. A. Bonn, W. N. Hardy, O. Gutowski, M. v. Zimmermann, S. M. Hayden, and J. Chang. Competing charge, spin, and superconducting orders in underdoped $YBa_2Cu_3O_y$. *Phys. Rev. B*, 90:054514, Aug 2014.

[74] Kazuhiro Fujita, Andrew R. Schmidt, Eun-Ah Kim, Michael J. Lawler, Dung Hai Lee, J. C. Davis, Hiroshi Eisaki, and Shin-ichi Uchida. Spectroscopic imaging scanning tunneling microscopy studies of electronic structure in the superconducting and pseudogap phases of cuprate high-Tc superconductors. *Journal of the Physical Society of Japan*, 81(1):011005, 2012.

[75] Kazushige Machida. Magnetism in La_2CuO_4 based compounds. *Physica C: Superconductivity*, 158(1):192 – 196, 1989.

[76] Jan Zaanen and Olle Gunnarsson. Charged magnetic domain lines and the magnetism of high-T_c oxides. *Phys. Rev. B*, 40:7391–7394, Oct 1989.

[77] H.-H. Klauss, W. Wagener, M. Hillberg, W. Kopmann, H. Walf, F. J. Litterst, M. Hücker, and B. Büchner. From antiferromagnetic order to static magnetic stripes: The phase diagram of $(\mathrm{La}, \mathrm{Eu})_{2-x}\mathrm{Sr}_x\mathrm{CuO}_4$. *Phys. Rev. Lett.*, 85:4590–4593, Nov 2000.

[78] M. Fujita, H. Goka, K. Yamada, and M. Matsuda. Competition between charge- and spin-density-wave order and superconductivity in $\mathrm{La}_{1.875}\mathrm{Ba}_{0.125-x}\mathrm{Sr}_x\mathrm{CuO}_4$. *Phys. Rev. Lett.*, 88:167008, Apr 2002.

[79] Qisi Wang, M. Horio, K. von Arx, Y. Shen, D. John Mukkattukavil, Y. Sassa, O. Ivashko, C. E. Matt, S. Pyon, T. Takayama, H. Takagi, T. Kurosawa, N. Momono, M. Oda, T. Adachi, S. M. Haidar, Y. Koike, Y. Tseng, W. Zhang, J. Zhao, K. Kummer, M. Garcia-Fernandez, Ke-Jin Zhou, N. B. Christensen, H. M. Rønnow, T. Schmitt, and J. Chang. High-temperature charge-stripe correlations in $\mathrm{La}_{1.675}\mathrm{Eu}_{0.2}\mathrm{Sr}_{0.125}\mathrm{CuO}_4$. *Phys. Rev. Lett.*, 124:187002, May 2020.

[80] C. T. Chen, F. Sette, Y. Ma, M. S. Hybertsen, E. B. Stechel, W. M. C. Foulkes, M. Schulter, S-W. Cheong, A. S. Cooper, L. W. Rupp, B. Batlogg, Y. L. Soo, Z. H. Ming, A. Krol, and Y. H. Kao. Electronic states in $\mathrm{La}_{2-x}\mathrm{Sr}_x\mathrm{CuO}_{4+\delta}$ probed by soft-x-ray absorption. *Phys. Rev. Lett.*, 66:104–107, Jan 1991.

[81] E. Pellegrin, N. Nücker, J. Fink, S. L. Molodtsov, A. Gutiérrez, E. Navas, O. Strebel, Z. Hu, M. Domke, G. Kaindl, S. Uchida, Y. Nakamura, J. Markl, M. Klauda, G. Saemann-Ischenko, A. Krol, J. L. Peng, Z. Y. Li, and R. L. Greene. Orbital character of states at the Fermi level in $\mathrm{La}_{2-x}\mathrm{Sr}_x\mathrm{CuO}_4$ and $R_{2-x}\mathrm{Ce}_x\mathrm{CuO}_4$ (R=Nd,Sm). *Phys. Rev. B*, 47:3354–3367, Feb 1993.

[82] C.-C. Chen, M. Sentef, Y. F. Kung, C. J. Jia, R. Thomale, B. Moritz, A. P. Kampf, and T. P. Devereaux. Doping evolution of the oxygen K-edge x-ray absorption spectra of cuprate superconductors using a three-orbital Hubbard model. *Phys. Rev. B*, 87:165144, Apr 2013.

[83] W. B. Doriese, P. Abbamonte, B. K. Alpert, D. A. Bennett, E. V. Denison, Y. Fang, D. A. Fischer, C. P. Fitzgerald, J. W. Fowler, J. D. Gard, J. P. Hays-Wehle, G. C. Hilton, C. Jaye, J. L. McChesney, L. Miaja-Avila, K. M. Morgan, Y. I. Joe, G. C. O'Neil, C. D. Reintsema, F. Rodolakis, D. R. Schmidt, H. Tatsuno, J. Uhlig, L. R. Vale, J. N. Ullom, and D. S. Swetz. A practical superconducting-microcalorimeter x-ray spectrometer for beamline and laboratory science. *Review of Scientific Instruments*, 88(5):053108, 2017.

[84] Young Il Joe, Yizhi Fang, Sangjun Lee, Stella X.L. Sun, Gilberto A. de la Peña, William B. Doriese, Kelsey M. Morgan, Joseph W. Fowler, Leila R. Vale, Fanny Rodolakis, Jessica L. McChesney, Joel N. Ullom, Daniel S. Swetz, and Peter Abbamonte. Resonant soft x-ray scattering from stripe-ordered $\mathrm{La}_{2-x}\mathrm{Ba}_x\mathrm{CuO}_4$ detected by a transition-edge sensor array detector. *Phys. Rev. Applied*, 13:034026, Mar 2020.

[85] R. Kajimoto, T. Kakeshita, H. Yoshizawa, T. Tanabe, T. Katsufuji, and Y. Tokura. Hole concentration dependence of the ordering process of the stripe order in $\mathrm{La}_{2-x}\mathrm{Sr}_x\mathrm{NiO}_4$. *Phys. Rev. B*, 64:144432, Sep 2001.

[86] Laimei Nie, Gilles Tarjus, and Steven Allan Kivelson. Quenched disorder and vestigial nematicity in the pseudogap regime of the cuprates. *Proceedings of the National Academy of Sciences*, 111(22):7980–7985, 2014.

[87] M. Hücker, G.D. Gu, J.M. Tranquada, M.v. Zimmermann, H.-H. Klauss, N.J. Curro, M. Braden, and B. Büchner. Coupling of stripes to lattice distortions in cuprates and nickelates. *Physica C: Superconductivity and its Applications*, 460-462:170 – 173, 2007. Proceedings of the 8th International Conference on Materials and Mechanisms of Superconductivity and High Temperature Superconductors.

[88] Stuart E. Brown, Eduardo Fradkin, and Steven A. Kivelson. Surface pinning of fluctuating charge order: An extraordinary surface phase transition. *Phys. Rev. B*, 71:224512, Jun 2005.

[89] W. L. McMillan. Landau theory of charge-density waves in transition-metal dichalcogenides. *Phys. Rev. B*, 12:1187–1196, Aug 1975.

[90] Oron Zachar, S. A. Kivelson, and V. J. Emery. Landau theory of stripe phases in cuprates and nickelates. *Phys. Rev. B*, 57:1422–1426, Jan 1998.

[91] Laimei Nie, Akash V. Maharaj, Eduardo Fradkin, and Steven A. Kivelson. Vestigial nematicity from spin and/or charge order in the cuprates. *Phys. Rev. B*, 96:085142, Aug 2017.

[92] E. Berg, E. Fradkin, E.-A. Kim, S. A. Kivelson, V. Oganesyan, J. M. Tranquada, and S. C. Zhang. Dynamical layer decoupling in a stripe-ordered high-T_c superconductor. *Phys. Rev. Lett.*, 99:127003, Sep 2007.

[93] Erez Berg, Eduardo Fradkin, and Steven A. Kivelson. Theory of the striped superconductor. *Phys. Rev. B*, 79:064515, Feb 2009.

[94] Erez Berg, Eduardo Fradkin, Steven A. Kivelson, and John M. Tranquada. Striped superconductors: how spin, charge and superconducting orders intertwine in the cuprates. *New J. Phys.*, 11:115004, 2009.

[95] J. Uhlig, W. B. Doriese, J. W. Fowler, D. S. Swetz, C. Jaye, D. A. Fischer, C. D. Reintsema, D. A. Bennett, L. R. Vale, U. Mandal, G. C. O'Neil, L. Miaja-Avila, Y. I. Joe, A. El Nahhas, W. Fullagar, F. Parnefjord Gustafsson, V. Sundstrom, D. Kurunthu, G. C. Hilton, D. R. Schmidt, and J. N. Ullom. High-resolution x-ray emission spectroscopy with transition-edge sensors: present performance and future potential. *J. Synch. Rad.*, 22:766–775, 2015.

[96] M. R. J. Palosaari, M. Käyhko, K. M. Kinnunen, M. Laitinen, J. Julin, J. Malm, T. Sajavaara, W. B. Doriese, J. Fowler, C. Reintsema, D. Swetz, D. Schmidt, J. N. Ullom, and I. J. Maasilta. Broadband ultrahigh-resolution spectroscopy of particle-induced x rays: Extending the limits of nondestructive analysis. *Phys. Rev. Appl.*, 6:024002, 2016.

[97] Luis Miaja-Avila, Galen C. O'Neil, Young I. Joe, Bradley K. Alpert, Niels H. Damrauer, William B. Doriese, Steven M. Fatur, Joseph W. Fowler, Gene C. Hilton, Ralph Jimenez, Carl D. Reintsema, Daniel R. Schmidt, Kevin L. Silverman, Daniel S. Swetz, Hideyuki Tatsuno, and Joel N. Ullom. Ultrafast time-resolved hard x-ray emission spectroscopy on a tabletop. *Phys. Rev. X*, 6:031047, 2016.

[98] Galen C. O'Neil, Luis Miaja-Avila, Young Il Joe, Bradley K. Alpert, Mahalingam Balasubramanian, D. M. Sagar, William Doriese, Joseph W. Fowler, Wilfred K. Fullagar, Ning Chen, Gene C. Hilton, Ralph Jimenez, Bruce Ravel, Carl D. Reintsema, Dan R. Schmidt, Kevin L. Silverman, Daniel S. Swetz, Jens Uhlig, and Joel N. Ullom. Ultrafast time-resolved x-ray absorption spectroscopy of ferrioxalate photolysis with a laser plasma x-ray source and microcalorimeter array. *J. Phys. Chem. Lett.*, 8:1099–1104, 2017.

[99] K.D. Irwin and G.C. Hilton. *Transition-Edge Sensors*, pages 63–150. Springer Berlin Heidelberg, Berlin, Heidelberg, 2005.

[100] R. Gualtieri, J. P. Filippini, P. A. R. Ade, et al. SPIDER: CMB polarimetry from the edge of space. *Journal of Low Temperature Physics*, 193(5):1112–1121, Dec 2018.

[101] J.N. Ullom, W.B. Doriese, D.A. Fischer, J.W. Fowler, G.C. Hilton, C. Jaye, C.D. Reintsema, D.S. Swetz, and D.R. Schmidt. Transition-edge sensor microcalorimeters for x-ray beamline science. *Synchrotron Radiation News*, 27(4):24–27, 2014.

[102] P. Eisenberger, P. M. Platzman, and H. Winick. X-ray resonant raman scattering: Observation of characteristic radiation narrower than the lifetime width. *Phys. Rev. Lett.*, 36:623–626, Mar 1976.

[103] J. R. Taylor, An Introduction to Error Analysis (University Science Books, Sausalito, CA, 1997).

[104] Matteo Mitrano, Sangjun Lee, Ali A. Husain, Minhui Zhu, Gilberto de la Peña Munoz, Stella X.-L. Sun, Young Il Joe, Alexander H. Reid, Scott F. Wandel, Giacomo Coslovich, William Schlotter, Tim van Driel, John Schneeloch, G. D. Gu, Nigel Goldenfeld, and Peter Abbamonte. Evidence for photoinduced sliding of the charge-order condensate in $\mathrm{la}_{1.875}\mathrm{ba}_{0.125}\mathrm{cuo}_4$. *Phys. Rev. B*, 100:205125, Nov 2019.

[105] M. Trigo, M. Fuchs, J. Chen, M. P. Jiang, M. Cammarata, S. Fahy, D. M. Fritz, K. Gaffney, S. Ghimire, A. Higginbotham, S. L. Johnson, M. E. Kozina, J. Larsson, H. Lemke, A. M. Lindenberg, G. Ndabashimiye, F. Quirin, K. Sokolowski-Tinten, C. Uher, G. Wang, J. S. Wark, D. Zhu, and D. A. Reis. Fourier-transform inelastic x-ray scattering from time- and momentum-dependent phonon–phonon correlations. *Nature Physics*, 9(12):790–794, Dec 2013.

[106] Darius H. Torchinsky, Fahad Mahmood, Anthony T. Bollinger, Ivan Božović, and Nuh Gedik. Fluctuating charge-density waves in a cuprate superconductor. *Nature Materials*, 12(5):387–391, May 2013.

[107] Georgi L. Dakovski, Wei-Sheng Lee, David G. Hawthorn, Niklas Garner, Doug Bonn, Walter Hardy, Ruixing Liang, Matthias C. Hoffmann, and Joshua J. Turner. Enhanced coherent oscillations in the superconducting state of underdoped $\mathrm{YBa_2Cu_3O}_{6+x}$ induced via ultrafast terahertz excitation. *Phys. Rev. B*, 91:220506, Jun 2015.

[108] J. P. Hinton, J. D. Koralek, Y. M. Lu, A. Vishwanath, J. Orenstein, D. A. Bonn, W. N. Hardy, and Ruixing Liang. New collective mode in $\mathrm{YBa_2Cu_3O}_{6+x}$ observed by time-domain reflectometry. *Phys. Rev. B*, 88:060508, Aug 2013.

[109] Yi-De Chuang, Yu-Cheng Shao, Alejandro Cruz, Kelly Hanzel, Adam Brown, Alex Frano, Ruimin Qiao, Brian Smith, Edward Domning, Shih-Wen Huang, L. Andrew Wray, Wei-Sheng Lee, Zhi-Xun Shen, Thomas P. Devereaux, Jaw-Wern Chiou, Way-Faung Pong, Valeriy V. Yashchuk, Eric Gullikson, Ruben Reininger, Wanli Yang, Jinghua Guo, Robert Duarte, and Zahid Hussain. Modular soft x-ray spectrometer for applications in energy sciences and quantum materials. *Review of Scientific Instruments*, 88(1):013110, 2017.

[110] S Smadici, J C T Lee, G Logvenov, I Bozovic, and P Abbamonte. Form factor dispersion at La $\mathrm{M}_{5,4}$ edges and average density of resonant atoms, journal = Journal of Physics: Condensed Matter. 26(2):025303, dec 2013.

[111] D. DiCarlo, E. Sweetland, M. Sutton, J. D. Brock, and R. E. Thorne. Field-induced charge-density-wave deformations and phase slip in nbse_3. *Phys. Rev. Lett.*, 70:845–848, Feb 1993.

[112] E. Pinsolle, N. Kirova, V. L. R. Jacques, A. A. Sinchenko, and D. Le Bolloc'h. Creep, flow, and phase slippage regimes: An extensive view of the sliding charge-density wave revealed by coherent x-ray diffraction. *Phys. Rev. Lett.*, 109:256402, Dec 2012.

[113] V. L. R. Jacques, C. Laulhé, N. Moisan, S. Ravy, and D. Le Bolloc'h. Laser-induced charge-density-wave transient depinning in chromium. *Phys. Rev. Lett.*, 117:156401, Oct 2016.

[114] S. N. Coppersmith and C. M. Varma. Shift in the longitudinal sound velocity due to sliding charge-density waves. *Phys. Rev. B*, 30:3566–3568, Sep 1984.

[115] T. Valla, A. V. Fedorov, Jinho Lee, J. C. Davis, and G. D. Gu. The ground state of the pseudogap in cuprate superconductors. *Science*, 314(5807):1914–1916, 2006.